THE CLOUDY H I HALO OF THE MILKY WAY

Dissertation

zur

Erlangung des Doktorgrades (Dr. rer. nat.)

der

Mathematisch-Naturwissenschaftlichen Fakultät

der

Rheinischen Friedrich-Wilhelms-Universität Bonn

vorgelegt von

Leonidas Dedes

aus

Veroia (Griechenland)

Bonn, Juni 2008

Angefertigt mit Genehmigung der Mathematisch-Naturwissenschaftlichen Fakultät der Rheinischen Friedrich-Wilhelms-Universität Bonn

1. Referent: PD Dr. Jürgen Kerp
2. Referent: Prof. Dr. Ulrich Klein

Tag der Promotion: 02.09.2008

Erscheinungsjahr 2008

Contents

1 Introduction

Neutral hydrogen is one of the most important components of the visible matter in the universe. From the time of the theoretical predictions of the 21-cm line, by the Dutch astronomer van der Hulst (1945) up to today, observations of the neutral hydrogen emission help to expand the knowledge in the field of Radio Astronomy. Almost five decades ago, Oort et al. (1958) for the first time brought to light the large scale morphology of our Galaxy, the Milky Way, using the HI line. Today the HI line is utilized in various fields, as a tracer to study the dark matter content of the galaxies, and as a probe of the physical conditions pervading through the interstellar medium (ISM). In the future, with the arrival of the Square Kilometer Array (**SKA**), studies of neutral hydrogen will give us the opportunity to understand Galaxy evolution and enable us to probe the epoch of re-ionization giving new insights in the cosmological evolution of the Universe (Carilli & Rawlings, 2004).

In Galactic astronomy, the 21-cm line plays a vital role in studying a variety of astrophysical phenomena from AU scales, up to scales of hundreds of kpc. This is due to the widespread distribution of the neutral hydrogen in the Galaxy, and its transparency which allows a detection even in areas where optical observations are very difficult (e.g., regions obscured by dust). Especially the neutral hydrogen in the Milky Way disk has been studied in great detail. I.e, large scale HI observations probed thoroughly the vertical structure of the disk, revealing an asymmetric warp reaching in height more than 4kpc above the plane at distances of 17kpc and measuring the flaring of the HI disk (Nakanishi & Sofue, 2004; Levine et al., 2006a; Kalberla et al., 2007). More recent studies detected a distant spiral arm in the outer part of the galaxy (McClure-Griffiths et al., 2004) and found evidence for disruption in the HI disk in the form of giant bubbles and super-shells (McClure-Griffiths et al., 2006). On smaller scales, regarding the structure of the ISM in Milky Way disk, it is known for some time that the diffuse neutral hydrogen resides in two phases: the warm neutral medium phase with a temperature $T < 8000$K and a cold dense neutral phase with $T \sim 80$K associated with discrete small HI structures, detected in absorption line studies (Heiles, 1997).

Furthermore, high above the Milky Way disk, another class of astronomical objects has been detected in the 21-cm line in 1963, the high-velocity-clouds (HVC), a population of HI clouds incompatible with Galactic rotation having a deviation velocity $\upsilon > 90\mathrm{km\,s^{-1}}$(Wakker & van Woerden, 1991). An estimate regarding their distance gives a lower limit of 5kpc (z>3.5kpc) for Complex C (Wakker et al., 1999) and for Complex A a distance d=4kpc, implying a height above the plane between 2.5kpc and 7kpc (van Woerden et al., 1998).

Above the Milky Way disk, moving with high velocities, lays a population of old, low metalicity stars, Globular Clusters and remnants of the accretion from Dwarf companions of the Milky Way. This layer of stars surrounding the Milky Way disk forms what is known as the Halo. Similarly in the case of dark matter it is proposed that it forms a dark matter halo surrounding the disk and dominating the gravitational potential of the Galaxy.

The question then arises, if there exists a stellar and dark matter Halo of the Milky Way Galaxy, is it possible that there exists also a similar gaseous layer surrounding the Galactic disk? If this is true, what is the origin of such a layer? Is it the result of an interaction between the Galaxy and the intergalactic medium? Is it the result from an accretion? Is it the product of other physical processes in the Galaxy like supernova explosion?

The answer to the first question is positive. Even from the early fifties, it was Spitzer (1956) who proposed that there exists a semi-static hot gaseous layer which surrounds the Milky Way disk. The vertical extent of the Galactic corona would be approximately 8 kpc with a temperature reaching 10^6 K and a total mass of 10^8 $\mathrm{M}_{\odot}$. The existence of such a layer was proposed mainly to explain the stability of high latitude clouds but also to facilitate the equilibrium of spiral arms in the presence of strong magnetic fields. Interestingly the idea of a Galactic corona was partially inspired from the claim of Pickelner (1953) for the existence of a homogeneous substratum of relatively cool gas, with a density of 0.1 cm^{-3} supported from turbulent motion with velocity 70 $\mathrm{km\,s}^{-1}$.

The first observational confirmation of the hot galactic corona hypothesis was given by Münch & Zirin (1961). Using absorption lines of distant stars outside the Milky Way disk, evidence was found for gas clouds at heights $z \sim 1$ kpc above the Galactic disk. From these clouds they found that the acceptible temperature for the Galactic corona is the one postulated by Spitzer of 10^6 K.

Shapiro & Field (1976) proposed the mechanism of the “Galactic fountain” in order to explain the presence of coronal gas and to introduce a process to cool the gas through convection and radiation. According to the mechanism, hot gas, produced by supernovae explosions in the disk, is buoyant. It streams upwards with a velocity perpendicular to the disk smaller or equal than the speed of sound. The outcome of this motion may have the following results: a) if the cooling is inefficient, the hot gas bubble reaches great heights above the disk, forming and becoming part of the Galactic corona of the disk, in hydrostatic equilibrium b) or if the cooling mechanism is efficient, at height z_c the hot bubble cools rapidly and undergoes a phase transition forming cool dense H I clouds. These clouds are not buoyant and so beyond this point they follow a ballistic motion under the influence of gravity which will bring them again at height z_c. It was the latter result of this mechanism that prompted Bregman (1980) to associate the galactic fountain mechanism with the formation of the HVC.

A few years later there was observational evidence that beyond the hot coronal gas surrounding the disk, there possible exists neutral gas extending high above the Milky Way disk. Lockman (1984) detected the 21-cm emission from these patches of neutral gas located in the inner Galaxy at heights greater than $|z|$>1000 pc. He proposed that the neutral gas in this region is following Galactic rotation and that this gas may form a layer that can not be solely thermally supported nor can it be considered as a single component isothermal layer.

While these were the first indication for the presence of neutral hydrogen as an extra-planar gas, more robust evidence was discovered later using the all sky 21-cm Bell Labs survey (Stark et al., 1992). Lockman & Gehman (1991) averaged 21-cm line emission spectra over large angular scales at high latitudes, detecting faint broad wings surrounding the main Galactic line. The estimated velocity dispersion was 35 km s^{-1} and the wings were attributed to HI surrounding the disk and it was proposed that the neutral hydrogen is forming a thick layer around it with a scale height of 1.5 kpc. The authors estimated that turbulence plays an important role in the maintenance of this layer in equilibrium configuration. The presence of extra-planar HI was further verified from the study of absorption lines of ionized titanium by Albert et al. (1994). They utilized ionized titanium as a tracer the neutral interstellar medium and from the observations towards six halo stars with $|z| > 1$ kpc they were able to verify the presence of a significant neutral gas phase. Although they were unable to determine the scale height accurately, they speculated that it can be well over a kpc and of the same order of magnitude as the scale height of hot gas.

All the above gave evidence that the disk of our Galaxy is surrounded by hot coronal gas and patchy neutral gas, forming a gaseous equivalent of the stellar halo. The more robust evidence for the existence of a thick gaseous layer surrounding the Galactic disk and the real breakthrough came with the completion of the 21-cm emission line Leiden/Dwingeloo/Survey(LDS) (Hartmann & Burton, 1997) and the analysis of the $\frac{3}{4}$keV and $\frac{1}{4}$keV diffuse soft X-ray background in the ROSAT all sky survey. Kalberla et al. (1998) used a version of the LDS corrected for instrumental effects to search for velocity wings of the main Galactic line in the emission spectra. They found solid evidence for the presence of the HI gas with a velocity dispersion of 60 km s^{-1}. The discrepancy between the LDS velocity dispersion and the dispersion velocity estimated from the Bell-Labs survey was attributed to the insufficient corrections of the instrumental baselines of the latter. Fig. 1.1 shows a comparison between the average spectrum of the LDS and the average spectrum of the Bell-Labs survey for the same position. In the same publication a vertical scale height of 4.4 kpc was derived for the observed diffuse HI component, assuming of course that the distributions of mass and pressure perpendicular to the plane are in hydrostatic equilibrium with the Galactic potential. Regarding the hot gas surrounding the Milky Way, Pietz et al. (1998) analyzed the intensity distribution of the $\frac{3}{4}$keV and $\frac{1}{4}$keV diffuse soft X-Ray background of the ROSAT all sky survey using the 21-cm LDS. The intensity distributions can be then described as the superimposed result of the extragalactic X-ray background and an isothermal X-ray Galactic Halo. The latter was modeled based on hydrostatic equilibrium considerations, and it was found that the hot gas responsible for the X-ray halo, described earlier as coronal gas, must have a temperature of $T = 1.5 \cdot 10^6$K and a scale height of 4.4kpc.

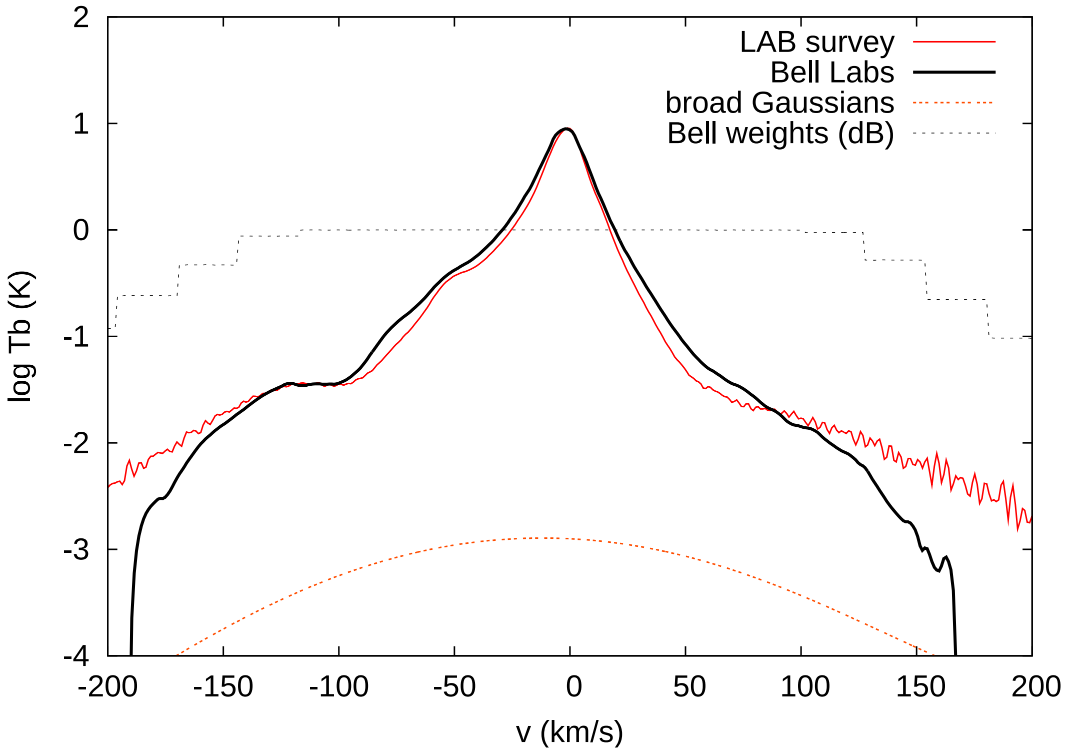

Fig. 1.1: *A comparison of the averaged spectra of the LDS and the Bell Labs survey. The black line shows the spectrum of the Bell Labs survey. The red line depicts the spectrum of the LDS. The dotted line depicts the weights applied to the Bell Labs baseline. Finally the dashed line shows the broad Gaussian component in the LDS.*

The last two results regarding the neutral medium and the hot gas in the halo gave the drive for the proposal of a gaseous Halo surrounding the Milky Way disk in hydrostatic equilibrium (Kalberla & Kerp, 1998). According to this, the thick gaseous layer has a vertical scale height of 4 kpc. This layer is highly turbulent, with turbulence most likely described by a Kolmogorov spectrum and providing the necessary support against the gravitational potential of the Galaxy. The gaseous Halo is composed by two constituents, each having 50% of its total mass, a) the hot gas which is a plasma with a temperature of of $T = 1.5 \cdot 10^6$ K and b) the neutral medium phase. Assuming pressure equilibrium between the plasma and the neutral gas yields a filling factor for the latter by around 10%. The prediction for the patchiness of the neutral gas agrees well with earlier observations by Albert et al. (1994) and Savage & Sembach (1996). Fig. 1.2 is a simple sketch showing the Galactic disk edge on surrounded by the different components of the gaseous Halo according to the Bonn model (Kalberla & Kerp, 1998) for the halo.

A vertical structure similar to the Milky Way with a thick layer of gas surrounding

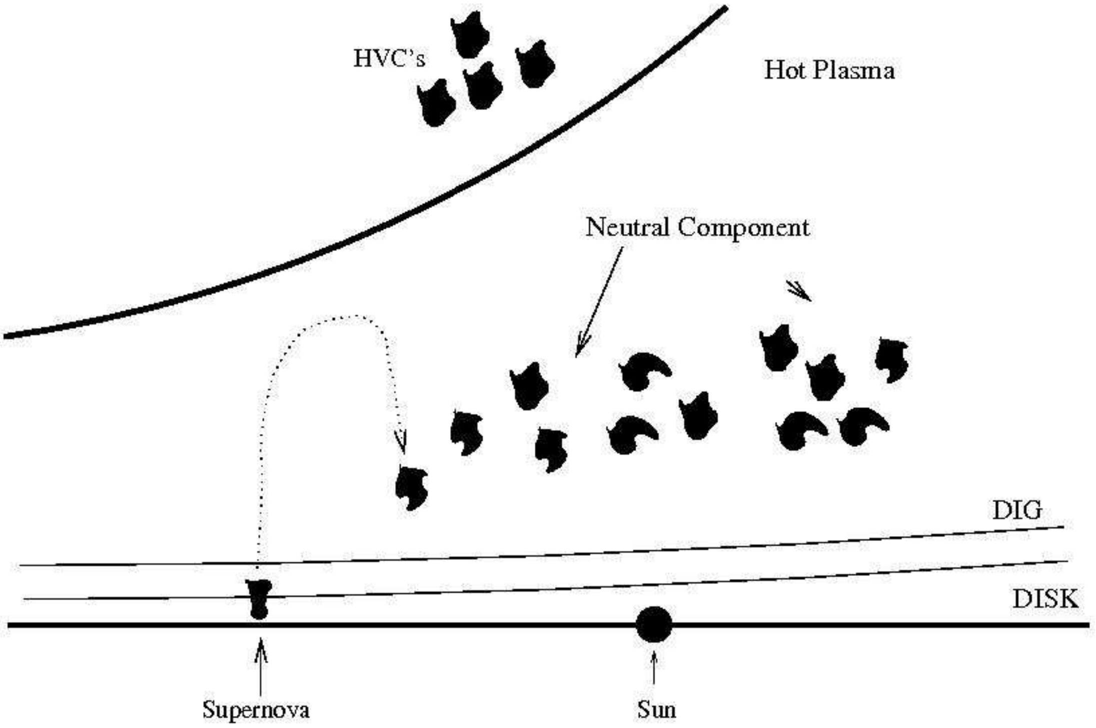

Fig. 1.2: *A sketch of the vertical structure of the Milky Way disk as proposed from the Bonn model. The different black thick lines correspond to the scale height of each layer. The disk is surrounded by the diffuse ionized component and the hot plasma with a temperature of* 10^6 *K. Embedded in it there are patches of neutral gas while high above the disk there are the HVC's.*

the disk was also revealed a few years later in an external galaxy by Fraternali et al. (2004). In the spiral galaxy NGC 2403 deep interferometry observations with the Very Large Array (VLA) detected the presence of a low density thick layer of neutral gas following Galactic rotation but rotating slower by 25-50$\mathrm{km\,s^{-1}}$, surrounding the thin "cold" disk. Chandra observations also revealed a diffuse hot gas component with a temperature $T \sim 10^6$K. Similar findings were reported in other spiral galaxies like NGC 891 and NGC 6946.

While evidence for the presence of the gaseous layer surrounding the Milky Way disk is significant, there are a number of fundamental questions that require a more detailed discussion in order to establish the presence of such a layer but also help us to answer various problems connected with the surrounding environment of our Galaxy such as the HVCs, the interaction with intergalactic gas material, galaxy formation etc. Most important of all is the creation mechanism of the gaseous halo and its origin. Does the gas have extra-galactic or Galactic origin? What supports this layer to reach great heights? Is turbulence support enough? What is the role of the magnetic field and cosmic rays? The second question has to do with the physical condition of the gas in the Halo. Is it possible for example, to have a stable two phase (cold and warm) configuration of the neutral gas or will all the gas eventually be driven to one of the

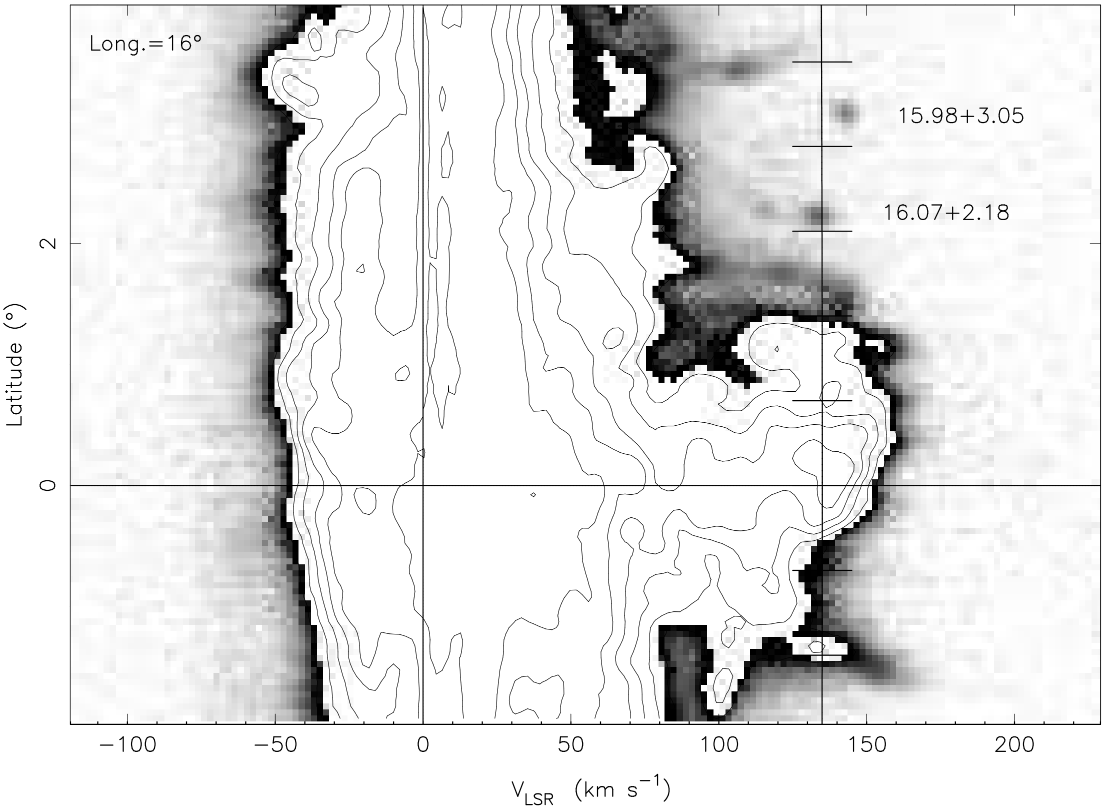

Fig. 1.3: *The 21cm emission as measured by GBT at l=16°. Grey scale shows emission below 2K and contours are a factor 2 from the peak. The vertical line at 135km s^{-1} marks the terminal velocity. Two clumps are identified in this map. (Taken by Lockman (2002))*

two phases? What are the cooling and the heating processes in the gaseous halo?

All these fundamental questions are intermingled and to shed light to one means finding answer for all others. The investigation of the spatial distribution of the halo was firstly undertaken since there was already evidence for the patchiness of the gaseous layer. Lockman (2002), using the 100-m Robert C. Byrd Green Bank Telescope(GBT), discovered the first direct evidence for the clumpy nature of the gaseous halo. He found in the inner Galaxy $\sim$ 1kpc above the Milky Way a number of discreet HI clouds at terminal velocity following Galactic rotation. In Fig. 1.3 the HI clouds can be seen.

These were barely resolved with the GBT telescope, they showed narrow line-widths and a significant number showed a two component core-envelope structure. Since they were observed at terminal velocity he could estimated their positions accurately in the lower layer of the galactic halo. A few years later a similar population of clumps towards the Galactic anti-center was discovered with the 300-m Arecibo telescope (Stanimirović et al., 2006). These clumps showed fairly similar characteristics as the ones detected with the GBT, although their location makes an accurate distance determination a very difficult task. In Fig. 1.4 a HI emission temperature brightness map is

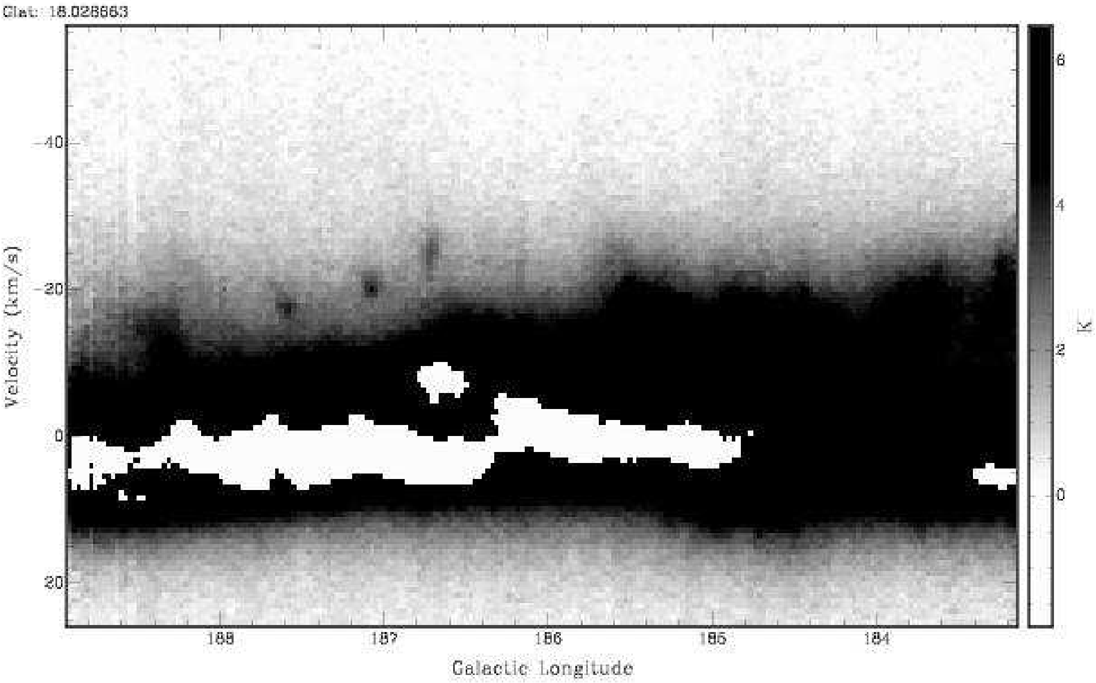

Fig. 1.4: *An 21cm line emission map observed with Arecibo at a region close to the anti-center. All pixels with T_B >12 K have been masked out. Three small clumps can be seen at* $b = 18^\circ$, $l = 186 - 188^\circ$ *at* υ_{lsr} *=-21 km* s^{-1}*(Stanimirović et al., 2006)*

shown with the detected HI clumps above the Milky Way disk.

If these HI clumps form the building blocks of the neutral component of the gaseous halo then inquiring more about them will help us infer more about the fundamental question regarding the nature of the gaseous halo. As a creation mechanism for the clumps it was proposed by Lockman (2002) that a Galactic fountain may play that role, thus opening the possibility that they are the low velocity counterparts of the HVCS. It was also suggested that these HI clumps are related to the formation of super-bubbles and are part of the caps of a super-bubble (McClure-Griffiths et al., 2006). Another possibility is, as suggested earlier, that they are the results of a large scale turbulence due to the shear bulk motions which form and maintain the gaseous halo of the Milky Way (Kalberla & Kerp, 1998).

Since the study of the patchy structure in the neutral gas of the Galactic halo is still at an infant stage, I undertook the task to study it with the help of large single dish telescopes and interferometer arrays. The aim of my study is to gather a sample of HI clumps belonging to the Galactic halo and to determine the physical properties, with the hope to gain knowledge of their physical condition of the formation and maintenance of these clumps and thus learn more about the nature of the Galactic gaseous halo.

This thesis is organized in the following way: Chap. 2 describes the aim of the thesis, the method followed to make the necessary analysis and the tools used to determine the observational parameters. In Chap. 3, I discuss my attempts to model the Galactic spiral structure using the linear density wave theory in order to improve the Bonn Milky Way Mass model. The results from observations using the 100-m Effelsberg Radio telescope are discussed in Chap. 4. In Chap. 5, I discuss the follow-up observations with two synthesis arrays, the Very Large Array (VLA) and the Westerbork Synthesis Radio Telescope (WSRT). In Chap. 6, I present data from a different Galactic quadrant, taken by Arecibo telescope where both extended and narrow emission can be traced. In the next chapter, Chap. 7, after presenting the data from various telescopes and extracting their physical parameters, I discuss the possibility of thermal equilibrium between the broad warm and the cold narrow phase of the neutral gas in the lower Galactic halo. From the Arecibo data a good opportunity arises to study the importance of turbulence in the Halo ISM, so I present the results of a statistical analysis of the density field in the Arecibo maps in Chap. 8. In Chap. 9 I discuss the nature of uncertainties affecting our physical parameter estimates and try to determine if there can be a correlation between the HI clumps and the Galactic fountain mechanism in order to provide an explanation for their origin. Finally in Chap. 10, I summarize my thesis and discuss future prospects and work in the field.

2 Method

2.1 Aim

During the last decade new observational discoveries have enriched our understanding of the environment surrounding the Galactic disk. The Galactic halo emerged as one of the important building blocks of the Milky Way. One important component is the gaseous layer surrounding the Milky Way disk (Spitzer, 1956; Kalberla & Kerp, 1998), composed partially of hot plasma ($T \sim 10^6$ K) and partially of neutral gas. Still there are a lot of unanswered questions. What is the origin of this layer? What mechanism provides the energy to support the layer reaching at such great heights (z$\sim$ 4 kpc) above the disk? Is it possible for a thermal equilibrium between its components to exists and how important is the role of turbulence? Understanding more about the gaseous halo will help us gain new insight to problems connected with it, like the nature and origin of the HVCs, the interaction with the infalling intergalactic medium (IGM) or the large scale feature of the Galactic disk like the asymmetric warp which dominates the outer parts of the disk.

Lockman (2002) discovered a population of compact H I clumps, residing in the lower parts of the halo. This was the first direct evidence of the highly clumpy nature of neutral ISM in the halo of the Milky Way at scales $|z|$<1.2 kpc. The sample is limited to the inner part of the Galaxy. It shows a mix of one and two component structures with the line width $\Delta\upsilon_{1/2}$ range spanning from a few km s^{-1} up to 20 km s^{-1}. It was proposed that a significant amount of the gaseous halo mass is in this state. To explain their origin, it is considered that the H I clumps are the late stage evolution of a Galactic fountain, where hot gas becomes a cool condensed clump, looses it buoyancy and follows a ballistic trajectory finally impinging on the Galactic disk.

Since a significant part of the gaseous Halo should be in this state, a sample of H I clumps similar to the ones detected with the Robert C. Byrd Green Bank 100m Telescope(GBT), but in different parts of the sky, could give us a better insight to their nature and their origin, thus helping us to better understand the neutral component of the Halo. In order to do this I undertook the task to detect and predominandly study the part of the Galaxy outside the Solar circle, in order to gather a sample of clumps for further study and comparison with the detections made by the GBT.

2.2 Properties of the H I clumps

Under the assumption that the H I clumps are part of the gaseous Galactic halo, they should have a number of intrinsic properties. These properties are used to discern them from HVCs, IVCs and gas without Galactic origin. Possible variation of these properties within a sample can be attributed to different creation mechanisms or different conditions in the Halo.

The hydrostatic equilibrium model for the gaseous Halo (Kalberla & Kerp, 1998) predicts that its two constituents, the neutral Halo medium and the hot plasma, must be co-rotating with the disk or alternatively rotating slower but still following the disk rotation (Bregman, 1980). So the HI clumps should also co-rotate or follow the Galactic rotation. In comparison, the HVCs by definition are incompatible with Galactic rotation (Wakker & van Woerden, 1997), having a velocity deviation v>|90| km s^{-1}.

According to Kalberla & Kerp (1998), pressure equilibrium between the hot and the neutral gas implies a filling factor of $\sim$ 10% of the HI gas with a column density of $10 \cdot 10^{18}$ cm^{-2}. Due to the clumpy nature of the neutral gas, one of the major properties of the HI clumps is the small angular size, a property already observed in the GBT sample.

Kalberla et al. (1998) found that velocity wings, which are detected when HI spectra are averaged over large scales, have an average velocity dispersion of 60 km s^{-1}. The wings are attributed to the neutral component of the halo, so the HI clumps are expected on average to show similar velocity dispersion.

Finally depending on the prevalent physical condition in the Galactic halo, a mix of cold neutral and warm neutral medium is expected to be present, something which is also detected in the Lockman (2002) sample.

To summarize, I will observe a number of fields in 21-cm, to identify coherent structures. Using their size, their velocity υ_{lsr} (velocity with the local standard of rest as reference) and line width, I will build a sample of HI clumps to study their properties.

2.3 Detection of HI clumps

As discussed earlier, the neutral component of the Halo has a filling factor of 10%, while the angular size of the clumps is a few times the $9'$ beam of the GBT telescope (Lockman, 2002). In order to detect clumps of this size with a single dish telescope of similar resolution and sensitivity, either a high resolution full sky survey or observations of regions with a high probability to detect HI emission from the Galactic halo are needed. The first option is time consuming, even when using a telescope with a multi-beam receiver, so I planned my observational strategy according to the second method.

With the help of the Leiden/Argentina/Bonn (LAB in this work) all sky survey (Kalberla et al., 2005a), I identified regions where the HI emission has higher probability to originate from the Galactic gaseous halo. This method is first described in Kalberla et al. (2005c). It uses a mass model of the Milky Way (Kalberla, 2003), discussed in section 2.5, to separate the HI emission in the LAB survey into three different regions:

1. emission originating from the Milky Way disk as defined by the model

2. emission originating from a high dispersion component (HDC) with an average velocity dispersion of 60km s^{-1} associated with the gaseous Galactic halo.

3. emission originating from HVCs.

Blanking the disk and HVCs emission, the end results is a data-cube of the LAB survey with regions presumably containing mostly HI halo emission. A colum density map is then produced, seen in Fig.2.5, which charts the distribution of the halo emission in longitude and latitude. The GBT HI halo clumps (Lockman, 2002) are detected in a region with l=29° and b=8°. In Fig. 2.5, this area is found within the region where Halo emission is expected. This is an independent verification that, using the aforementioned method, we can successfully confine the parameter-space in position and velocity.

Still even in Fig. 2.5 halo emission covers a large area of the sky. Therefore I need to identify smaller regions to probe for HI clumps. The region where the GBT HI halo clumps (Lockman, 2002) are detected, is associated with faint diffuse emission in the LAB survey. So within the parameter-space of the halo, I selected regions which showed similar characteristics.

2.4 Distance determination

Assuming an HI clump has a distance d kpc and subtends an angle A from the observer. The clump diameter D is given approximately by the simple formula for the arch length: $D = A \cdot d$. Now knowing the size of the clump, physical parameters like density and pressure can be estimated. It is easy to conclude that the knowledge of distance is fundamental to estimate any physical quantities and any failure to calculate it correctly will lead to large error in the outcome of the calculations (Chap. 9).

The most direct method to estimate a distance is from the line of sight velocity with respect to the local standard of rest υ_{lsr} . Assuming circular motions of the neutral gas around the center of the Galaxy and that angular velocity $\Omega(R)$ is a decreasing function of Galactocentric radius R, the line of sight υ_{lsr} is given by

$$V_{lsr} = R_{\odot}[\Omega(R) - \Omega_{\odot}] sinl \tag{2.1}$$

Using this equation, each measured velocity along a line of sight is attributed to distance. Generally an a priori knowledge of the velocity field is needed.

As discussed in Section 2.2, HI clumps follow Galactic rotation. Measuring their υ_{lsr} and using the equation 2.1 should be enough to estimate their distance d from the Sun. But the fact that we are also part of the Galaxy imposes either a limitation or an advantage depending on which part of the Galaxy the HI clumps are positioned with respect to the Sun. In case the HI clumps lie in the inner Galaxy, with distance

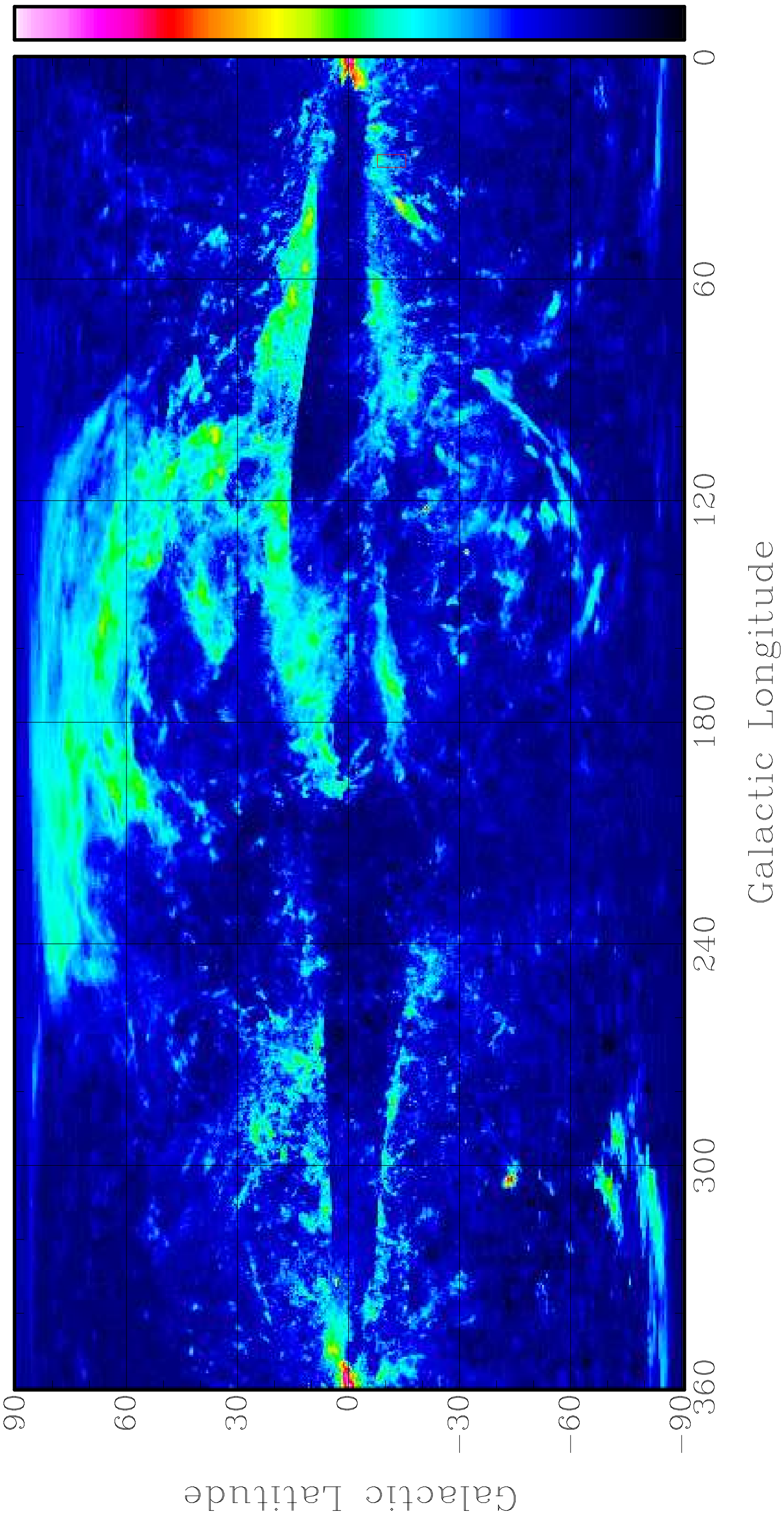

Fig. 2.5: *A column density map of the* H I *emission most probably associated with the Galactic Halo. The integration limits are defined by the Bonn model. The disk emission is masked and its emission has not been taken into account in the integration. IVCs are still visible in this map. At* $l = 29^\circ$ *and* $b \sim$*-8°, in a region marked by a red box, the first sample of* H I *clumps have been detected.*

R smaller than the distance $R_\odot$ of the Sun from the Galactic Center($R < R_\odot$), υ_{lsr} is not useful due to the distance degeneracy. In diagram 2.6, the line-of-sight velocity υ_{lsr} versus distance d is plotted for the inner Galaxy, for $0° < l < 90°$. It is obvious that two different distances have the same velocity υ_{lsr} since the line of sight intercepts an inner orbit two times. But there is a position in which the line of sight is tangential to a Galactocentric circle. This point is called tangent point and the velocity of this point the terminal velocity. The degeneracy at this point is broken and the distance can be determined unambiguously if the distance $R_\odot$ of the sun to the Galactic center is known. To measure distances at the tangential points a knowledge of the total Galactic velocity field is not required only the terminal velocity and the corresponding distance. Lockman (2002) utilizes low latitude $^{12}CO(1-0)$ studies to derive the terminal velocity and determines accurately the distance of the co-rotating H I clumps in the inner Galaxy.

In the outer part of the Galaxy, where $R > R_\odot$, as seen in 2.6, υ_{lsr} (R) is defined uniquely with distance, so no terminal velocity exists. Since my study is focused on the outer part, I use a different method to estimate the distance from υ_{lsr} . I utilize the equation 2.1 to convert the υ_{lsr} directly to distance d. The assumed Galactic velocity field is derived from a Milky Way mass model (Kalberla, 2003), described in subsection 2.5 while according to I.A.U standard $R_\odot = 8.5$ kpc. It is obvious that the Galactic model is a major source of systematic uncertainties for the measured physical parameters of the H I clumps. In Chap. 9 I give some examples of different estimates of the distance for different Galactic model.

The kinematic determination of the distance has two additional drawbacks. It can be used only if the clumps follow the Galactic rotation while also small peculiar velocities of the clumps can not be taken into account, increasing further the systematic uncertainties. More importantly, as discussed in Chap. 3 and Crane (1988), there are regions in the Galactic velocity field where $\frac{dv}{dr}$ is very small and therefore it is not feasible to get a reasonable estimate for the distance. These position where there is the so called velocity crowding are region with longitude close to the center and anti-center but also with $l \sim 75°$and $l \sim 285°$.

To avoid determining the distance kinematically one could use pressure equilibrium considerations. This method is used in Stanimirović et al. (2006) to derive distances for H I halo clumps detected near the anti-center. The properties of the H I clumplets show similarities with the CNM clouds in the Galaxy. It is known that in the Milky Way CNM and WNM clouds can co-exist in pressure equilibrium in an isobaric environment, with thermal pressure within a well defined range of P_{min} and P_{max} (more detailed study by Wolfire et al. (2003) ; Chap. 7). Wolfire et al. (2003) determined the P_{min} and P_{max} in the Galactic midplane for several Galactocentric radii. Also for H I clumps the volume density is $n \propto N_{\rm HI} \times d^{-1}$ (sub-section 2.6) where $N_{\rm HI}$ is the column density and d is the distance while the pressure is given by $P \propto nT_{kin}$ where the kinetic temperature T_{kin} can be measured by the line width $\Delta\upsilon_{1/2}$. Using the above

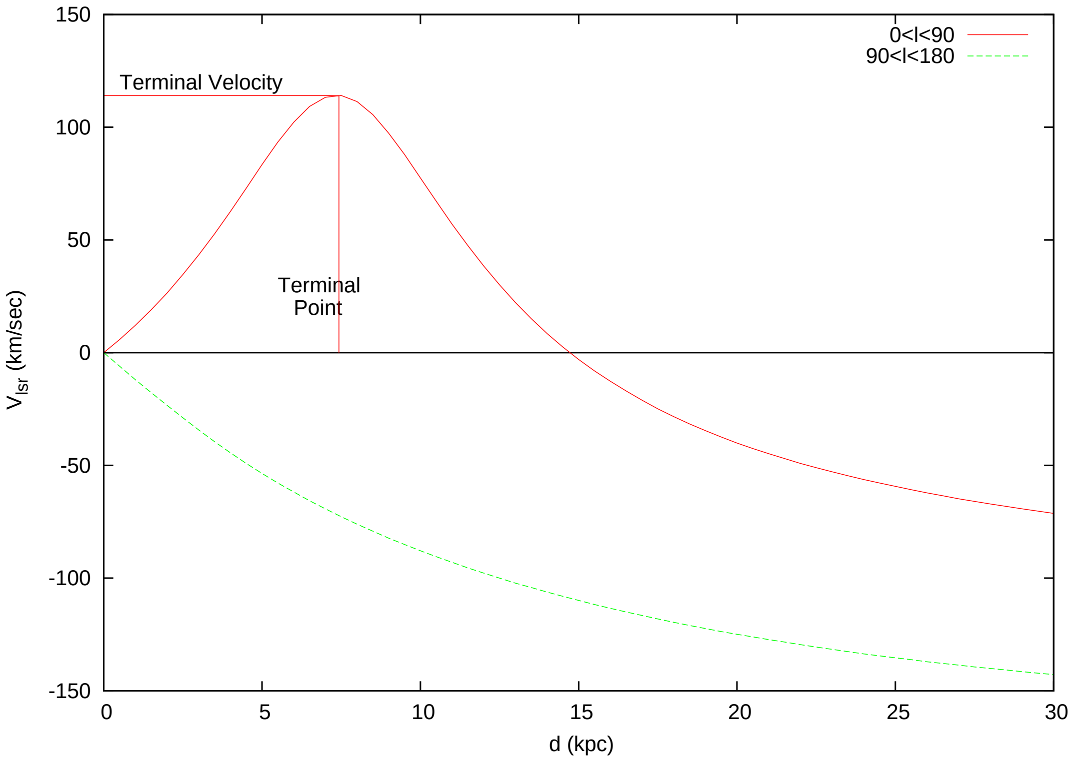

Fig. 2.6: *Inner Galaxy degeneracy: A plot of line-of-sight velocity* υ_{lsr} *versus the distance d to the observer. The red line show the change of* υ_{lsr} *with the distance in the inner part of the galaxy for longitude 0°<l<90°, while the green line show the change of the* υ_{lsr} *with the distance in the outer part of the galaxy for longitude 90°<l<180°.*

relations and the pressure range within which the two phases can co-exist (Wolfire et al., 2003), an upper and a lower limit for the distance can be derived. The major caveats are the ad-hoc assumptions that the metalicities, the dust-to-gas ratio and FUV field are known in the Halo, and similar with the disk. Wolfire et al. (1995b) shows that the range of pressures where equilibrium can exist between the two phases may change dramatically depending on the condition of the Halo ISM. Further measurements are needed to find the exact distances of the clumps. Thus this method has a limited use to the anti-center region and more generally regions where velocity crowding is important, and therefore the υ_{lsr} can not be converted directly to distances. In Chap. 9 I compare distance estimates for detected clumps using this method and compare them with the kinematical distances.

2.5 Milky Way mass model

An accurate Galactic model is necessary to disentangle disk from halo HI emission and to determine the distance. I used the Bonn Mass model described in Kalberla (2003) and Kalberla et al. (2007).

It is a model where the Galactic mass distribution is described by a number of isothermal components that are in equilibrium with the gravitational potential. The different components are: an isothermal stellar disk with a thin and thick component, a bar, a bulge and isothermal gaseous disks for molecular gas, cold neutral medium (CNM), warm neutral medium (WNM), diffuse ionized gas (DIG), a hot ionized gas and cold neutral halo. Surface densities and scale heights of all the components are adjusted according to observational constrains (Table 2.1). The distribution of visible mass can be supplemented by any dark matter distribution matching observational constrains. According to Kalberla et al. (2007) the distribution fitting the flaring of the Milky Way best has a spherical halo, a dark matter disk and a dark matter ring at 13kpc<R<18kpc. The rotation curve of the model, used also to estimate distances in the Milky Way, is shown in Fig. 2.7. What is important to note is that while the model assumes that the gaseous halo of the Milky Way follows the rotation of the Galactic disk, the halo does not co-rotate with the disk but it is lagging behind the disk. Important aspects that a Galactic model should also take into account, are the large scale features of the Galaxy like the Galactic warp and the spiral arms. This is especially important for the distance estimate since features like spiral structure may alter the velocity field of the Galaxy. In the Bonn mass model the Galactic Warp is taken into account (Kalberla et al., 2007). Regarding the spiral structure I try to model it using the linear density wave theory. This effort is thoroughly discussed in Chap. 3. All in all the Bonn mass model described a self-consistent solution which agrees with imposed observational constrain such as the observed flaring in the LAB HI survey (Kalberla et al., 2007).

2.6 Measuring the observational properties of the clumps

In order to study the HI halo and the clumps initially the 100-m Effelsberg Radio telescope is used to observe a number of fields with $9'$ resolution at 21-cm (Chap. 4). The selection of the observed regions is based on the HI column density map of the LAB survey given in Fig. 2.5. Further selection is done using a number of criteria: 1) since the aim is to study the outer Galaxy, the regions must have a longitude $90^\circ < l < 270^\circ$, 2) in the LAB survey the region must have faint HI emission (up to ∼2K), similar to the regions observed with GBT, 3) finally, since the υ_{lsr} is used for distance determination, areas where where $\frac{dv}{dr} \sim 0$ should be avoided in order to prevent large uncertainties in the distance determination.

The observed HI clumps are specified by a number of physical properties, the kinetic temperature T_{kin}, the average volume density $< n >$, the spatial diameter D, and the thermal pressure P. I will determine these properties for each clump from a set of quantities measured with a radio telescope.

Independent of the specific type of observations, whether single dish or interferometry, the final result after the application of the data reduction is a 3-dimensional array called

	ρ	h_z	Σ	σ
	cm^{-3}	pc	$(\mathrm{M}_\odot/\mathrm{pc}^{-2}$	$\mathrm{km\,s}^{-1}$
Gaseous disk:				
Molecular gas	0.66	75	3.0	3.5
Cold neutral medium	0.30	150	2.8	6.0
Warm neutral medium	0.10	400	2.5	14.8
Diffuse ionized gas	0.024	950	1.5	26.8
Neutral halo medium	0.0012	4020	0.3	60
Hot halo medium	0.0013	4020	0.3	60
Stellar disk:				
Thin disk	1.3	325	18.6	14.3
Thick disk	0.3	630	8.7	24.3
Dark Matter disk	0.69	4240	129	105

Tab. 2.1: *A table showing the different isothermal components constituting the Milky Way Mass Model. ρ is the mid-plane density at the position of the Sun, h_z is the local exponential scale height perpendicular to the Galactic plane. Σ is the local surface density and σ the isothermal velocity dispersion. The table is taken from Kalberla (2003)*

image cube. This holds information about the brightness temperature T_B or the flux density S distribution of the H I emission of the sky for each channel, that is for a specific velocity with respect to a reference velocity. Using a visualization software, for example the package KARMA (Gooch, 1996), I inspected the image cube of each observed field searching for H I clumps. Their identification was done according to the premises discussed in section 2.2. In case of a detection I can then extract the spectrum of the H I clump. In case it is unresolved, it would be the spectrum from a single position (pixel), while in case the clump is resolved the spectrum is from the central position.

Ideally, the H I atoms of the clump have a Maxwellian velocity distribution and the spectrum is best described by a Gaussian (Fig. 2.8). The following information can then be extracted from it:

1. The peak brightness temperature T_B
2. the line-of-sight velocity υ_{lsr} of the peak of the line, measured by the Doppler shift with respect to the rest frequency of H I ,
3. the line width $\Delta\upsilon_{1/2}$ which is connected with the velocity distribution of H I atoms in the clump, causing the broadening of the line due to the Doppler shift and
4. the total area enclosed by the line.

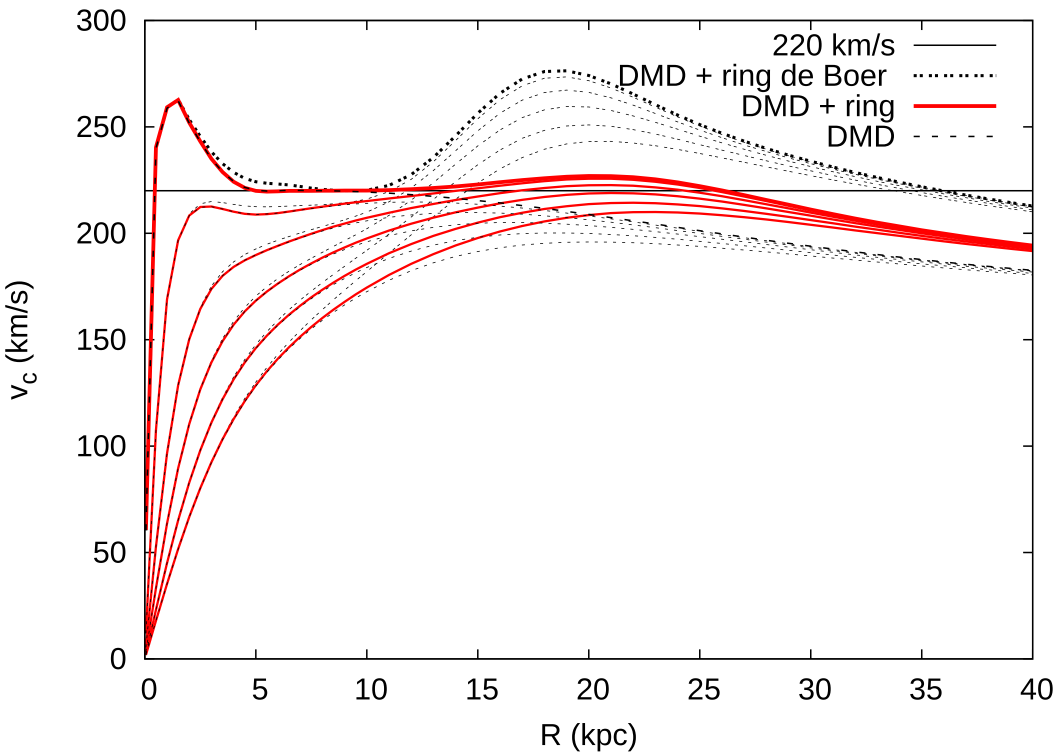

Fig. 2.7: *Rotation curves for the Milky Way mass models(Kalberla et al., 2007). The dashed black lines give the rotation curve for the initial dark matter disk, and the dotted lines the curves for the dark matter disk including a ring according to de Boer et al. (2005). The thick red lines show the rotation curve for the model used to convert* υ_{lsr} *to distance. To the rotation at* $z = 0$ *(top thick curves) the authors display in each case the circular streaming velocities at* $|z| = 1$ *to 5 kpc(from top to bottom).*

Using the line-of-sight velocity υ_{lsr} ($\mathrm{km\,s^{-1}}$), as described in subsection 2.4 and assuming that the clump follows the Galactic rotation I can estimate its distance from the sun d (kpc), their Galactocentric radius R (kpc) and the height above the disk plane z (kpc).

Using the line width $\Delta\upsilon_{1/2}(\mathrm{km\,s^{-1}})$ and making the good assumption that the HI is behaving like an ideal gas and has Maxwellian distribution I can then estimate the kinetic temperature of the gas T_{kin} from the formula $\frac{T_{kin}}{\mathrm{K}} = 22 \cdot \frac{\Delta\upsilon_{1/2}^2}{\mathrm{km/s}}$. In case turbulence is important this is the upper limit for the T_{kin} of the gas, since turbulence is the cause of the line broadening.

Assuming the neutral gas is optically thin with an optical depth $\tau << 1$, the total area A can be converted to the peak column density of the HI gas by using the following formula $N_{HI} = 1.8224 \cdot 10^{18} \cdot A\ \mathrm{cm}^{-2}$.

For an ideal spectrum like the one seen in Fig. 2.8 we can extract the above quanti-

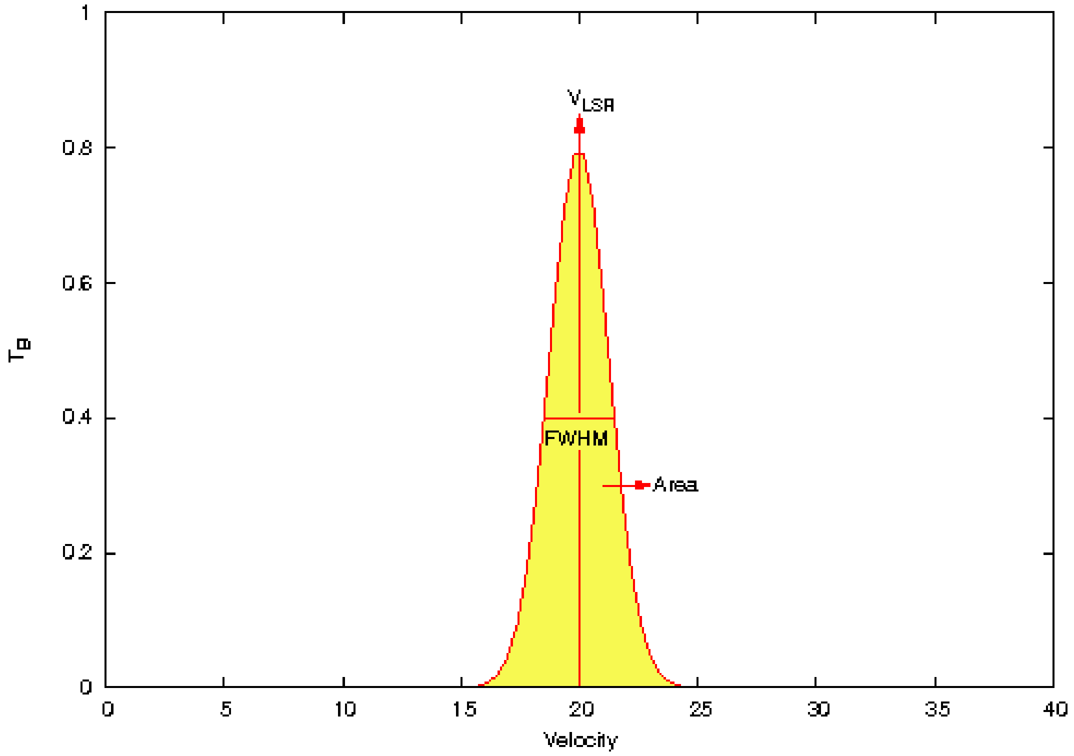

Fig. 2.8: *A ideal spectrum of an* HI *line which has a Gaussian shape.*

ties simply by fitting a Gaussian function. Unfortunately this was only true in very limited cases in the observed sample of HI clumps. A typical clump spectrum is similar to the one shown in Fig. 2.9. A two component structure is present. The narrow component which is the detected HI clump and the more extended underlying component which is the envelope. As seen in Fig. 2.9 usually, but not necessary, the broad line component is part of the extended wing of the main Galactic line. The HI clump has a very small angular extent, at adjacent positions only the broad extended component is present. A Gaussian fit, in the two component case, shows no convergence since the broad component surrounding the clumps can hardly be described by a Gaussian. In such a case the envelope/background emission must be removed manually in order to determine the properties of the clump. Due to the low intensity of the extended envelope, bad baselines in the image map increase the uncertainty in the measured quantities. Assuming the clump (narrow component) has a temperature T_c and the warm extended component has temperature T_e, the radiative transfer is: $T_m = T_e \cdot e^{-\tau} + T_c(1-e^{\tau}) \rightarrow T_m = T_{ext} + T_{nar}$ where T_m is the total measured brightness temperature, T_{ext} is the brightness temperature of the extended component T_{ext} and T_{nar} is the brightness temperature of the HI clump. Thus it is simple to derive that the total area measured is the sum of the area of the clump and the extended component. To remove the extended background at the position of the HI clump I measured

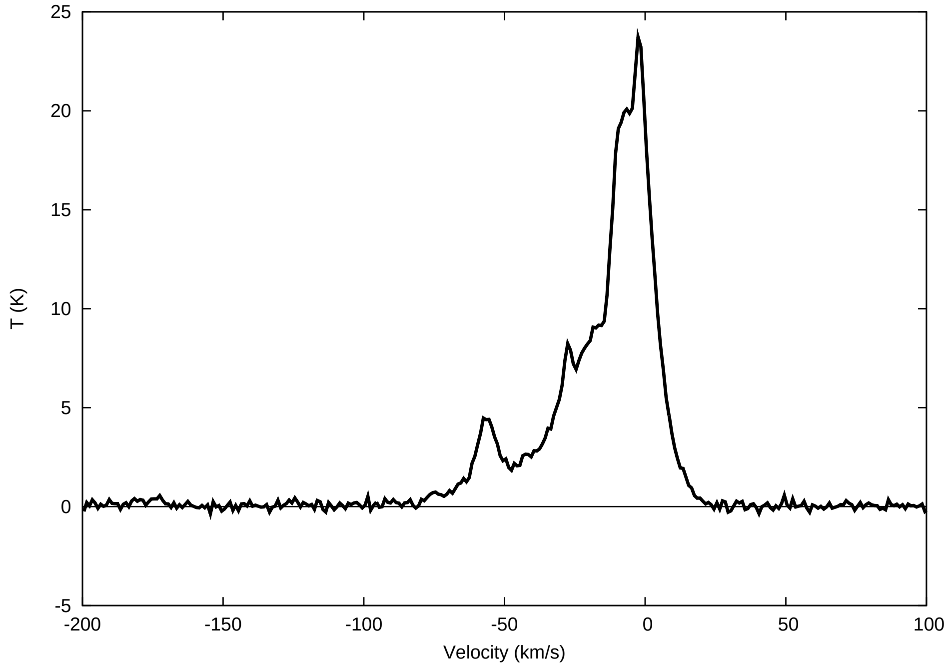

Fig. 2.9: *A typical spectrum of an* HI *clump. The clump is located at l=112.96°, b=-12.44° and* υ_{lsr} *~-50km* s^{-1} *on top of an extended Galactic wing.*

for a specific velocity range the total area, then for the same velocity range I measured the area for an adjacent position where there is no narrow HI emission. The result gave me the area A under the clump (narrow line) thus estimating the column density for that position. The υ_{lsr} of the clump is easily determined from the position of the peak. The $\Delta\upsilon_{1/2}$ is measured at the half maximum of the peak.

The HI image cube is used to measure the angular diameters of the HI clumps. For HI clumps which were unresolved or resolved in one axis the angular diameter is estimated using their angular width w and the angular length l, according to $s = (w \cdot l)^{1/2}$(in arc-minutes). In the case where the clump is resolved, I fitted a circular Gaussian and estimated the $\Delta\upsilon_{1/2}$ of the HI clumps which was defined as the angular diameter s.

If the distance from the Sun is known, the diameter of the clump is $D = d \cdot s$ where d is measured in parsec and s in radians. Assuming now that the HI clump has a circular cross section and that the density is constant in the clump, I calculated the average volume density of the clump as $< n >= \frac{N_{HI}}{D}$ (in cm^{-3} where N_{HI} is the column density and D is the diameter respectively. The error in the calculation of the volume density in this case depends on the deviation of the actual shape of the clump from the assumed cylindrical shape. In reality the error in the distance determination is more important and influences the uncertainty of the density measurement.

Finally, knowing the density and the temperature, I can estimate the Pressure P from the formula $\frac{P}{K \cdot \mathrm{cm}^{-3}} = \frac{<n>}{\mathrm{cm}^{-3}} \cdot \frac{T_{kin}}{\mathrm{K}}$ and the mass of each clump in solar masses. It is important here to note that both the pressure and the mass estimates depend on the distance as $P \sim d^{-1}$ and $M \sim d^{2}$. Uncertainties of the distance determination influences the estimates for these physical parameter.

3 The spiral structure in the Milky Way

3.1 Introduction

In an HI brightness temperature T_B distribution map of position versus velocity , like the one at Fig. 3.11a, the neutral gas can be described by the fundamental equation of 21-cm structure analysis:

$$v_c = R_{\odot}[\Omega(R) - \Omega_{\odot}]sinl \tag{3.2}$$

where v_c is the radial velocity, Ω is the angular velocity at radius R, and $\Omega_{\odot}$ the angular velocity at the position of the Sun, $R_{\odot}$. It is easily discernable in this map, that T_B does not have a smooth distribution. Large scale features like the warp, deviations from circular rotation like the spiral arms, temperature fluctuations and a non-isotropic density distribution, all alter the expected profiles. All these factors have to be taken into account in order to construct an accurate disk model with the aim to use it to distinguish HI emission originating from the Galactic Halo. Large scale features like the warp have already been incorporated in the model. Fig. 3.11b is a l-v HI brightness temperature map of the Milky Way model at $b = 0°$with the inclusion of the warp . It is obvious that Fig. 3.11b and Fig.3.11a are different. The former shows a smooth distribution of gas with velocity, while the latter, the real data, shows elongated filamentary concentrations, a lot of them the results of spiral arms structure. In accordance, the spectra of the real data are the results of the accumulating influences of the temperature and density fluctuations of the neutral hydrogen in the disk as well as kinematic irregularities of the gas deviating from the circular rotation.

Although it is quite difficult to weight the importance of the two former effects, as it is shown in chapter 7 of Crane (1988), the kinematic irregularities play a dominant role in the morphology of the spectra. This is apparent in the regions where $\frac{d\upsilon}{dr} \sim 0$, for example at l=0°, 180°, 75°, 285°. There, since υ varies slowly with radius, the profiles contain a contribution from a long path length and thus enhancing the measured T_B . Quite similarly kinematic irregularities alter the Galactic velocity field. As a result, gas from different regions of the disk with similar υ_{lsr} velocities, appear as large scale structure features which can be interpreted wrongly as true density variations. Such structures represent mostly deviations from circular rotation. The most important kinematical irregularities are induced by the spiral arms which are present on a large scale in Fig. 3.11a. So, in order to test the effect of spiral structure in the Milky Way model, I have tried to implement the spiral structure in it. I used the linear density wave theory to predict the perturbation velocities and then created synthetic data cubes to compare them with the LAB survey to test the parameters of each model and judge its success.

3.2 The model of the Galactic spiral structure

First of all I assume the Galactic spiral structure exhibits a grand design which is supported by a density wave. The second important assumption is that the line profile characteristics are caused mainly by kinematics and any structure as spiral arms should be attributed to kinematical irregularities due to the presence of a density wave. To model the Galactic spiral structure I used the linear density wave theory. It was proposed to solve the winding dilemma of grand design spirals and was outlined in a series of papers by Lin & Shu (1964, 1966); Lin et al. (1969). According to this theory, the spiral arm is considered as a quasi-stationary compression zone of interstellar matter. So, while the zone is not disrupted and follows solid body rotation, matter can stream through it. The advantage of this idea is that both Galactic differential rotation of Galactic matter and the solid body rotation of the Galactic arms can co-exist. The application of this theory to the motion of neutral hydrogen was first described by Yuan (1969).

To model the spiral arms I followed Burton (1971). For a gravitational potential of an axisymmetric disk U_a, we assume that the spiral arms create a perturbation U_s, so the total gravitational potential of the disk is $U_d = U_a + U_s$. Therefore if the gas moves in regular circular orbit with angular velocity $\Omega(R)$ at distance R from the Galactic center, it has a circular velocity $V(R)$ and a radial velocity with respect to the local standard of rest of V_c. In the presence of spiral arms, the perturbation of the gravitational potential Φ_s induces in the gas a peculiar motion. In the radial direction towards the Galactic center and the position of the gas this potion has velocity υ_r while the tangential induced velocity is υ_θ. Fig. 3.10 shows the direction of the induced motions. Taking into account the above considerations the total radial velocity with respect to the local standard of rest (l.s.r) is given by:

$$V_{lsr} = V_c + \upsilon_r cos(l+\theta) + \upsilon_\theta cos(90 - l - \theta) \quad (3.3)$$

where l is the galactic longitude and θ is the galactocentric azimuth, measured clockwise from the radius passing through the Sun.

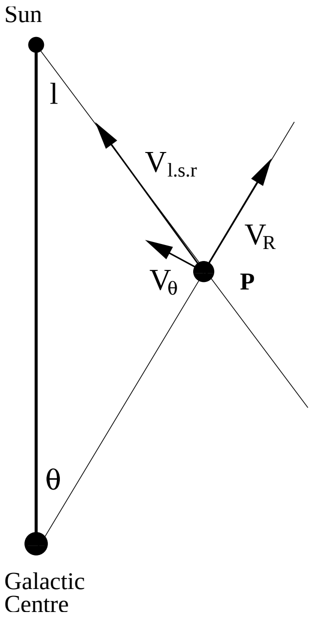

Fig. 3.10: *Coordinate system for the calculation of the velocity perturbations. θ is the azimuth measure clockwise from the radius connecting the sun with the galactic center.$V_{l.s.r}$ is the radial velocity, υ_r , υ_θ is the perturbation velocities.*

Assuming that the spiral structure of the Milky Way is described by a logarithmic function, the radial phase function is given by

$$\Phi(R) = -m \cdot \frac{1}{b} \cdot log \frac{R \cdot \tan(i_o)}{R_o \cdot \tan(i)} \tag{3.4}$$

where $\Phi(R)$ is the radial phase factor, m is the number of spirals, R_o is the radius where the spiral structure starts, and the tangent of the pitch angle is given by $tan(i) = \alpha \cdot R + \beta$.

The phase of the superimposed gravitational potential is:

$$\chi(R,\theta) = m\dot{\theta} - \Phi(R) + \chi_o \tag{3.5}$$

where χ_o is the initial phase of the spiral arms.

The radial wave number is defined as $k(R) = \frac{d\Phi(R)}{dR}$ and is related with the radial spacing of the arms $\lambda = \frac{2\pi}{k(R)}$.

Assuming that the spirals are tightly wound, i.e $|tg(1)| << 1$, according to Burton (1971) the velocity perturbations are given by the following formulae:

$$\upsilon_r = a_r cos\chi(r,\theta) \tag{3.6}$$

$$\upsilon_\theta = a_\theta sin\chi(r,\theta) \tag{3.7}$$

The amplitude of the peculiar motions is a function of the angular pattern speed Ω_p, the average angular velocity $\Omega(R)$, the surface density in the center of the spiral σ_{max}, the surface density in the inter-arm region σ_{min} and the epicyclic frequency k^2.

$$a_r = \frac{\sigma_{max} - \sigma_{min}}{\sigma_{max} + \sigma_{min}} \cdot \frac{m}{-k(R)} \cdot (\Omega(R) - \Omega_p) \tag{3.8}$$

$$a_\theta = (\frac{k^2}{4} \cdot \frac{1}{(\Omega(R)^2 - \Omega_p\Omega(R))})a_r \tag{3.9}$$

Using these formulas we can estimate the peculiar motions due to the density wave and thus the radial velocity $V(r,\theta)$.

I used the Bonn mass model described in Kalberla (2003); Kalberla et al. (2007) to get the necessary values for the unperturbed circular velocity V_c and the angular velocity $\Omega(R)$ in order to produce a synthetic data cube, including the peculiar motion from the spiral arms. The data cube is then compared with the HI LAB survey. The aim is to identify the similarities in the morphology of the spiral arms produced in the model with the real spiral structure in the LAB survey. The linear density wave theory model from its conception does not provide an accurate description of the real spiral structure.

Therefore, while it is able to reproduce the morphology, it can not replicate exactly the line profiles of the real data. As a result a direct comparison between the brightness temperature T_B distribution for the two data cubes, the model and the real data, is not feasible and does not produced any reasonable results. Therefore the comparison is done visually. A more accurate method would preferably try to fit a model data cube with the real data to extract the parameters of the spiral arms as done e.g. to extract the properties of the warp in external galaxies (Józsa et al., 2007). Such a method is beyond the scope of this work which has as main aim the study of the HI clumps in the Galactic halo. In this Chapter my target is to show to what extent the linear density wave can describe the spiral structure and how much the large scale features in the disk are a product of velocity perturbations.

3.3 Results

In order to compare the spiral structure in the LAB survey with the model, I have produced for each model a synthetic data cube. Each one covers a region in velocity of $|\upsilon_{lsr}|$<250 km s^{-1}, all longitudes and latitudes between $|b|< 15°$. The following parameters are kept fixed for all the models:

- the initial radius R_o. This marks the start of the spiral structure and the end of the Galactic bar. It is considered to be 3kpc (Vallée, 2002).
- the pattern speed Ω_p. This is the angular velocity with which the spiral arms rotate around the Galaxy. Due to our unique position, it is very difficult to measure it for the Spiral arms of our own Galaxy. Lin et al. (1969) used a guess of $\Omega_p = 13.5$km s^{-1}kpc^{-1} which produced the most reasonable results when comparing model with observations. The authors claims that even higher values could produce acceptable results. Recently Fernández et al. (2001) observationally determined the angular pattern speed at $\Omega_p = 30$km s^{-1}kpc^{-1} from kinematical studies of two samples of HIPPARCOS data, one containing 0- and B-stars and the other composed of Cepheid variables. This is used for all the models except in Burton (1971) where for consistency $\Omega_p = 13.5$km s^{-1}kpc^{-1} is used.
- the initial phase χ_o. I assumed either the simple case that at the position of the spiral arms $\chi = 0$ or the more valid one that at the central region of the spiral arms both $|\upsilon_r|$ and $|\upsilon_\theta|$ must be maximized. I utilized the plot from Vallée (2002) which shows that at starting radius of the spirals R_o the Crux arm has $\theta = 20°$. All my model were tested for both values

To reproduce the spiral structure, according to the relation of the previous section 3.2, I varied for each model the surface density contrast between the arm-inter-arm region, the number of spiral arms m and the pitch angle i. In respect to the latitude dependence the equations of the peculiar velocity do not take latitude b into account. What varies as a function of latitude is the angular velocity in the case of the lagging halo. The surface density contrast is independent of the latitude b. As shown later for $|b|>4^\circ$, the perturbations induced by spirals do not affect the brightness temperature distribution of the l-v maps created with the models. In such a case only the Galactic warp plays a dominant role, deviating from symmetry.

The first series of models to present were produced to test the difference between the kinematical and the density approach in the analysis of spiral structure. Levine et al. (2006b) observationally determined the spiral structure parameters from the LAB survey. First they transformed the brightness temperature T_B emission from a heliocentric data set into a HI density grid with Galactocentric radius. For this conversion a standard rotation curve was taken into account together with epicyclic corrections, but not velocity perturbations due to spiral arms. Their second step was to apply an un-sharp masking technique which enhances the contrast between low and high surface density features, emphasizing thus the spiral structure. Finally the authors fitted the observed spiral features of the density waves using a logarithmic spiral similar to equation 3.4, thus determining the number of spirals and the apparent pitch angles. A sum of their parameters is found in Table 1 of Levine et al. (2006b). They have found 4 arms with pitch angles of 24°, 24°, 25°, 21°at the Solar circle. It is obvious from the above analysis that they considered spiral structure as density perturbations, not velocity perturbations, apparent in the density cubes. To test their estimate I used the pitch angle values for a series of a synthetic model. Since in my models all the spiral arms have the same pitch values I used the average of 23.5° of Levine et al. (2006b). Assuming that the spiral structure has indeed the morphology found in Levine et al. (2006b) then the synthetic $l-v$ diagrams should reproduce some of the structure seen in the real $l-v$ from the LAB survey. For the angular pattern I used the $\Omega_p = 30\text{km}\,\text{s}^{-1}\text{kpc}^{-1}$ for reason explained earlier while the surface density contrast was set to 4, a value extracted from the LAB survey by Kalberla et al. (2007). The angular pattern speed and the surface density do not affect significantly the positions of the spiral arms in the synthetic cubes. This model was also modified to include either 2 or 4 arms for different values of the initial spiral structure phase χ_o.

In Fig. 3.12, 3.13 and 3.14 I present the comparison between the best synthetic cubes based on Levine et al. (2006b) and the real LAB data. A direct comparison between these show that there exists no similarity between the real data cube and the synthetic cubes with parameters based on Levine et al. (2006b). Using different values for the initial phase χ_o still cannot reproduce the spiral structure with these pitch angles. This pitch angles fail to reproduce even partially the plot seen in the real data of the LAB survey. This outcome is probably due to the T_B conversion to density used by Levine et al. (2006b). Besides considering the spiral features as density perturbation only when converting the original heliocentric dataset $T_B(\upsilon_{lsr}, l, b)$ of the LAB survey to a Galactocentric one $n_{HI}(R, \theta, z)$, no correction for the spiral arm peculiar velocity was applied. This implies that different parts of the Galactic HI with similar υ_{lsr} due to velocity perturbations will appear as density enhancements mimicking spiral structures. These do not necessary trace neither the position and morphology of the density wave nor the actual position of the real surface density enhancements induced by the spiral arms. So a fit to a density data cube can provide only the apparent values for the spiral arms and cannot be taken as an accurate description of the position and morphology of the spiral arms.

The next model is based on a set of parameters used by Burton (1971) for a similar analysis. In this paper it is assumed that the spirals have a pitch angle of 8° at R=5kpc which slowly decreases to 5° at R=10kpc. Because $R_{\odot}$=10kpc, I rescaled the above values to match the I.A.U estimate of $R_{\odot}$=8.5kpc. Table. 3.2 gives the α and β parameter determine the corresponding pitch angle. For the surface density contrast between the arm-inter-arm region Burton (1971) varied the value from 1 at the Galactic Center to 4.33 at R=10kpc. Since in my model the density contrast is kept constant throughout the spiral arms I adopted the average value of 2.65 for this model. As a result it is expected that for radii where the Burton (1971) model has lower density contrast, I estimated peculiar velocities to be higher while in the radii where the Burton (1971) model has higher density contrast, I estimated lower peculiar velocities. As a result, the contrast between the arm-inter region will be sharper than in the Burton (1971) original model but also the positions will have small modifications.

The *l*-*v* diagram of this model in comparison with the real data is seen in Fig. 3.15. This comparison shows that the spiral structure is poorly reconstructed with this set of parameters. The main similarity is the position of the bump, marked by a black circle in Fig. 3.15b, at the terminal velocities with *l*=30° and *l*=50°. The large arch which lies at the fourth quadrant with a starting position of *l*=-60° up to *l*=0° is missing in the synthetic model. And there is only a nearly faint reconstruction of the arch at the first and second quadrant, and of the outer arm starting at *l*=-180°.

I also compared the real LAB data with the synthetic data of model 4 for *b*=3°, as seen in Fig. 3.16. The application of the density wave theory does not improve the Bonn mass model much in comparison with the real data in this case. The similarities between the real emission and the synthetic data seen at the second quadrant between *l*=60°- 180° is mostly due to the inclusion of the warp in the Bonn model. The peaks of brightness temperature T_B located at the same position, at *l*=75°, *l*=180°, are due to velocity crowding expected in these areas (Chap.2). In conclusion model 4 has some success in the inner part of the Galaxy but fails generally to reproduce the large scale features in the real data.

After the trials based on the Burton (1971) and Levine et al. (2006b) models, I have produced a number of synthetic data cubes trying to match the $l-v$ maps of the real LAB data. Numerous sets of parameters were tested. As a guideline for the chosen values I used a meta-study of the Galactic spiral structure by Vallée (2002) which summarizes the most recent results on the spiral parameters. From all this datasets I will present the 3 that most successfully reproduced the spiral structure of the Milky Way.

The first model has a number of spiral arms $m = 4$ and a surface density contrast of 3. For the pitch angle I considered at the solar circle that $i \sim 12.5^\circ$ which is the estimated average in Vallée (2002). I used Burton (1971) to describe the change of the pitch angle as a function of distance. Fig. 3.17,3.18 show the comparison of the $l - v$ maps of this model and the LAB data for b=0° and b=3°, respectively. In Fig. 3.17 the black ellipses mark the regions where there is very good match between the synthetic data and the real data. As can be seen this model is quite successful. It reproduces the grand arch at the first and second quadrant. It also matches nicely the regions for terminal velocity and parts of the inner Galaxy. It even reproduces a filamentary structure at at l=180°-240° which seems to be connected with the outer arm (McClure-Griffiths et al., 2004). On the other hand it fails to reproduce the small arch at the fourth quadrant (l=290°-330°) at b=0 and also the terminal velocity regions for υ_{lsr} <0 $\mathrm{km\,s^{-1}}$ and large filamentary structure from (l,υ_{lsr} =19°,-16.49 $\mathrm{km\,s^{-1}}$) to (l,υ_{lsr} =70°,-74 $\mathrm{km\,s^{-1}}$) which seems to be not only a result of spiral structure but additionally it is probably connected with the arch at the fourth quadrant. For the higher latitudes, Fig. 3.18 shows that the model is not successful. While it produces structures, marked inside black ellipses, which morphologically are similar to features in the real data, the extent and the position of these features in the synthetic data is different from the real data.

The second model that produced successful results has a number of spiral arms m=4, a surface density contrast of 4, and a pitch angle $i = 11.7^\circ$ at the solar circle. Fig. 3.19, 3.20 show the $l - v$ brightness temperature maps for b=0° and b=3° in comparison with the real data. In Fig. 3.19 the black ellipses mark again structures which are similar to the real data. This model reproduces at the same location the great arch seen in quadrants 1 & 2 , the outer arms and also a structure located at negative velocities in quadrants 1 & 2 . While it also produces a structure similar to the small arch at the fourth quadrant, the location is different and positioned closer to the plane. At l=-106° , it produces a spiral feature not seen in the real data. At latitude b=3°, shown in Fig. 3.20, there are some morphological similarities but the positions are different from the real data. All in all this model also fails to produce feature similar to the real data for $b \neq 0^\circ$.

The last successful model has also four spiral arms and a surface density contrast of 4. The pitch angle is $i = 12.5^\circ$and the initial phase of the spiral arms is $\chi = 320^\circ$ to take into account that the Crux arm starts at $\theta = 20^\circ$ (Vallée, 2002). Fig. 3.21, 3.22 show the $l - v$ diagrams as a comparison with the real LAB data for b=0° and b=3°, respectively. In Fig. 3.21 for $b = 0^\circ$ it is seen that this model reproduces the small arch structure at the fourth quadrant as well as the bump at the terminal velocity in the inner Galaxy for $l < |60|^\circ$. It fails to reproduce the large arch structure for l>70° and the outer arms at $l \sim -170^\circ$. While it reproduces similar structures morphologically,

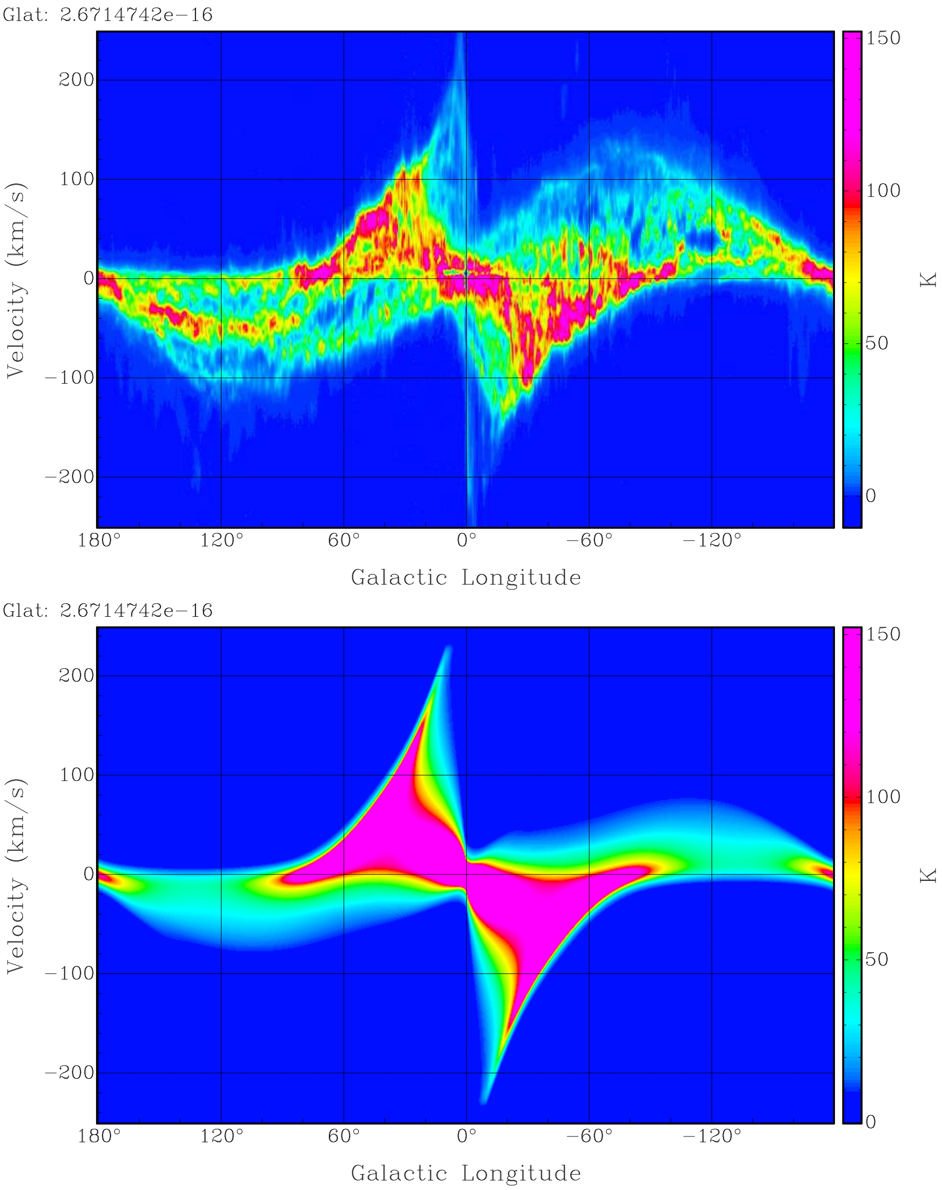

Fig. 3.11: *a) Top: An* HI *emission map of longitude versus* υ_{lsr} *along the Galactic equator (b=0°) from the LAB survey. (b) Middle: An* HI *emission map of longitude versus* υ_{lsr} *of the Milky Way model (Kalberla, 2003) which includes the warp, without spiral arm at b=0°.*

these are created at different velocity positions. For b=3° from Fig. 3.22 , it is again obvious that while we have some structures similar to the real data, marked with black ellipses, the model fails to produce a more accurate picture.

Table 3.2 summarizes all the parameters for the models discussed here, with the last three sets being the ones creating synthetic data cubes closer to the real data.

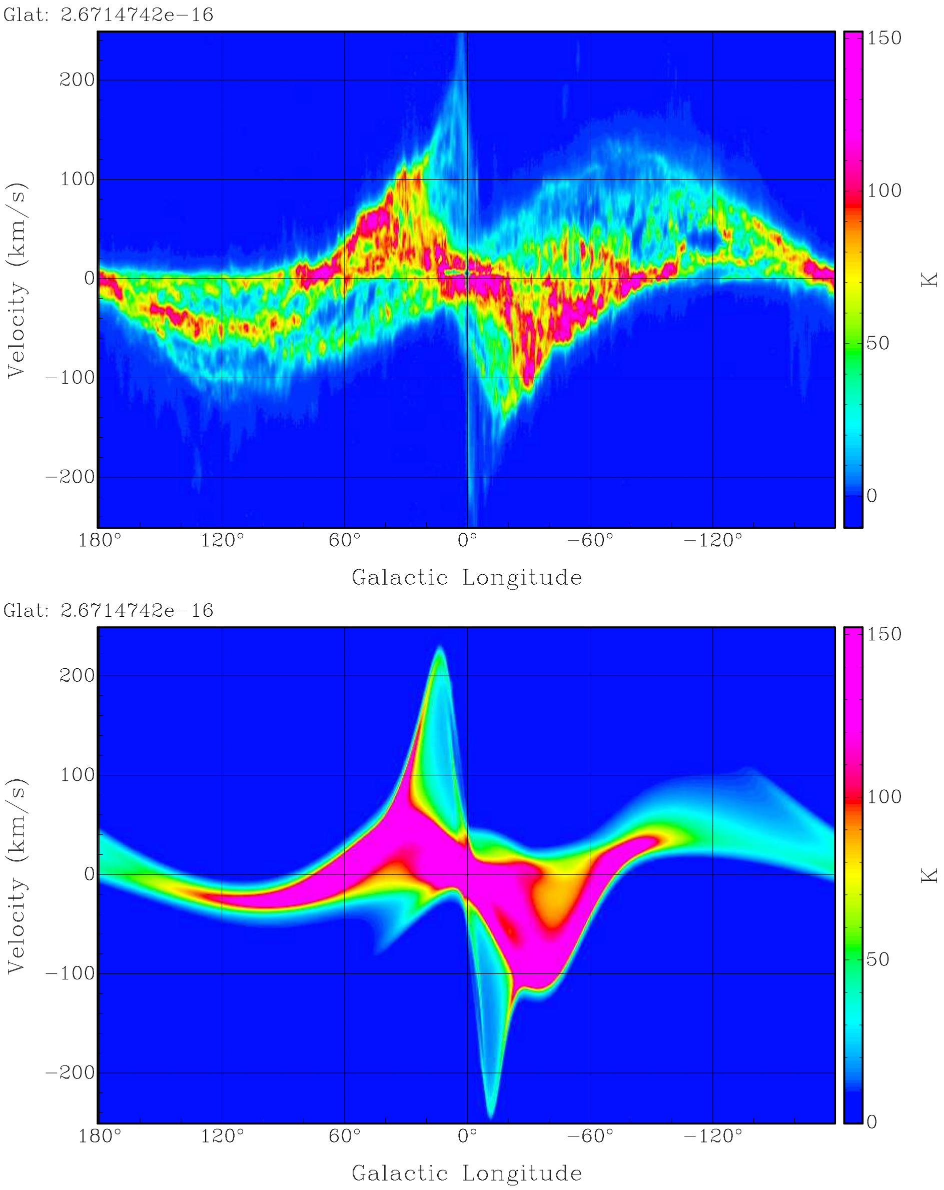

Fig. 3.12: *A comparison of longitude versus* v_{lsr} *(l-v) emission* HI *maps between the real LAB data and the model based on Levine et al. (2006b)(a) Top: An* HI *emission map of along the Galactic equator (b=0°) from the LAB survey. (b) Bottom: An synthetic emission map from the model Model 1 with m=2, Contrast=4,* $\Omega_p = 30$ *km/sec/kpc,* R_o*=3.0kpc,* $\chi_o = 0°$, $\alpha = 0$, $\beta = 0.435$

3.4 Dependence on b

In Fig.3.23 two $l - v$ maps are presented for b=-3°, one of the LAB real data and the other of the non-spiral arms model. A comparison between the two shows that the non-spiral model has a very smooth distribution of the HI emission, with an asymme-

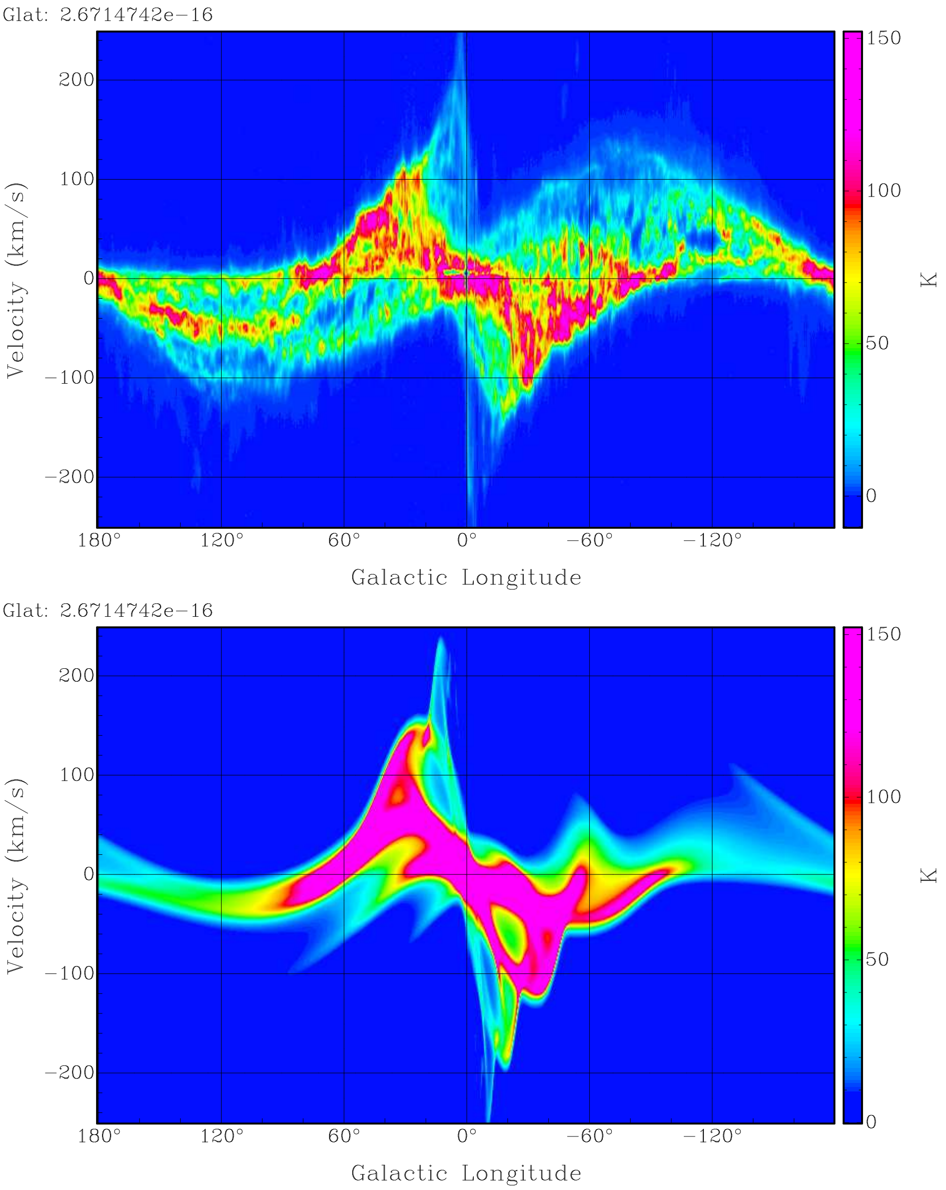

Fig. 3.13: *A comparison of longitude versus* v_{lsr} *(l-v) emission* HI *maps between the real LAB data and model based on Levine et al. (2006b) (a) Top: An* HI *emission map along the Galactic equator (b=0°) from the LAB survey. (b) Bottom: An synthetic emission map from the model Model 2 with m=4, Contrast=4,* $\Omega_p = 30$ *km/sec/kpc,* R_o*=3.0kpc,* $\chi_o = 0^\circ$, $\alpha = 0$, $\beta = 0.435$.

try present between positive and negative longitudes due to the warp. This is quite different from the patchy and filamentary structure shown in the real data. This structure is reproduced, not always accurately, under the assumption that it is the result of spiral arms. In the previous section the models presented were not successful for $b \neq 0$.

In Fig. 3.24 model 8 is shown, which differs from model 7 in the surface density

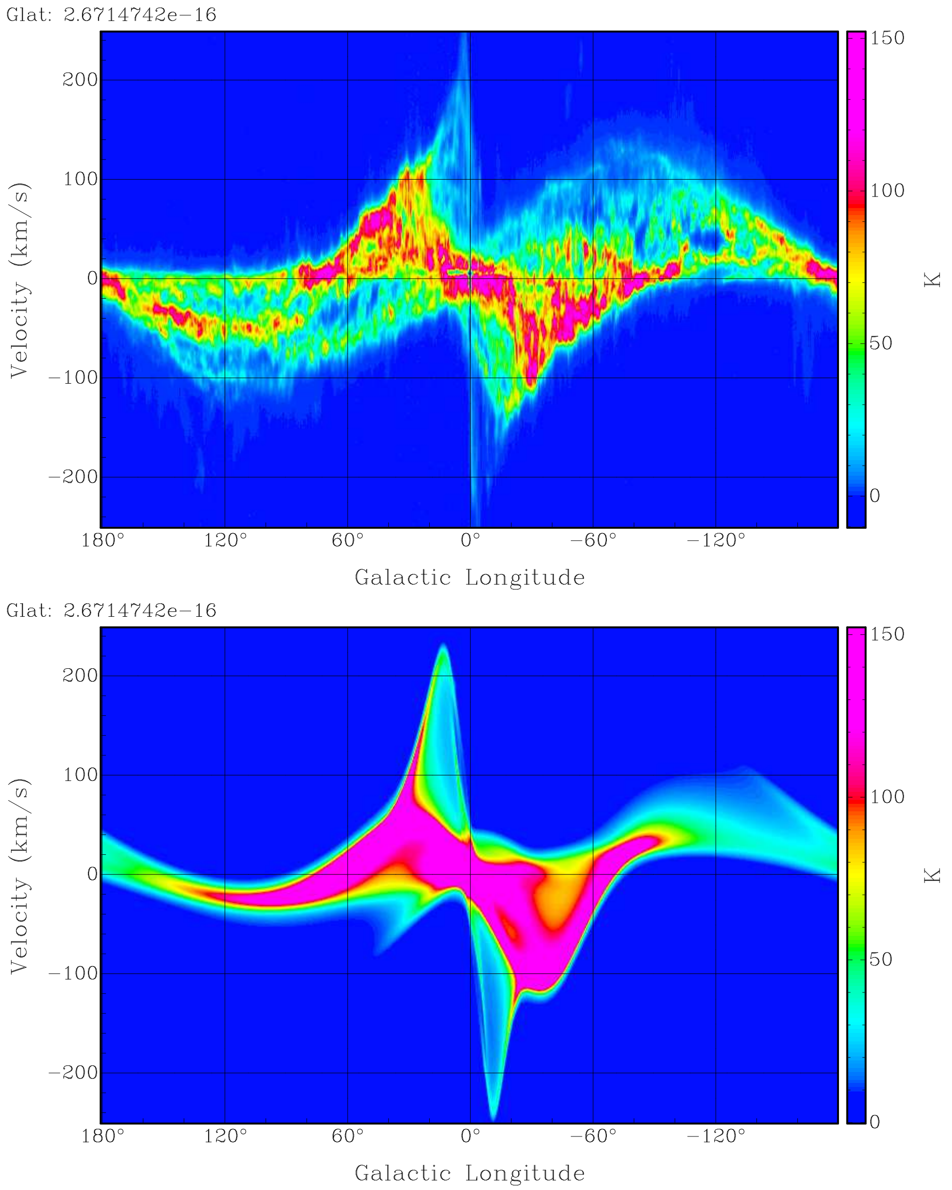

Fig. 3.14: *A comparison of longitude versus* υ_{lsr} *(l-v) emission* HI *maps between the real LAB data and the model based on Levine et al. (2006b). (a) Top: An* HI *emission map of along the Galactic equator (b=0°) from the LAB survey. (b) Bottom: An synthetic emission map from the model Model 3 with m=2, Contrast=4,* $\Omega_p = 30$ *km/sec/kpc,* R_o*=3.0kpc,* $\chi_o = 6°$*,* $\alpha = 0$*,* $\beta = 0.435$.

contrast with C=3 and the initial phase with $\chi_o = 69°$. In Fig. 3.24b I overlaid the real data with the model represented as contours. One can easily ascertain the presence of similar structures, attributing them to spiral structure. In the real data the filamentary structure seems to be clearly present up $|b|$<8°. Our models have only limited success and show similar structure up to $|b|$<4.5 .

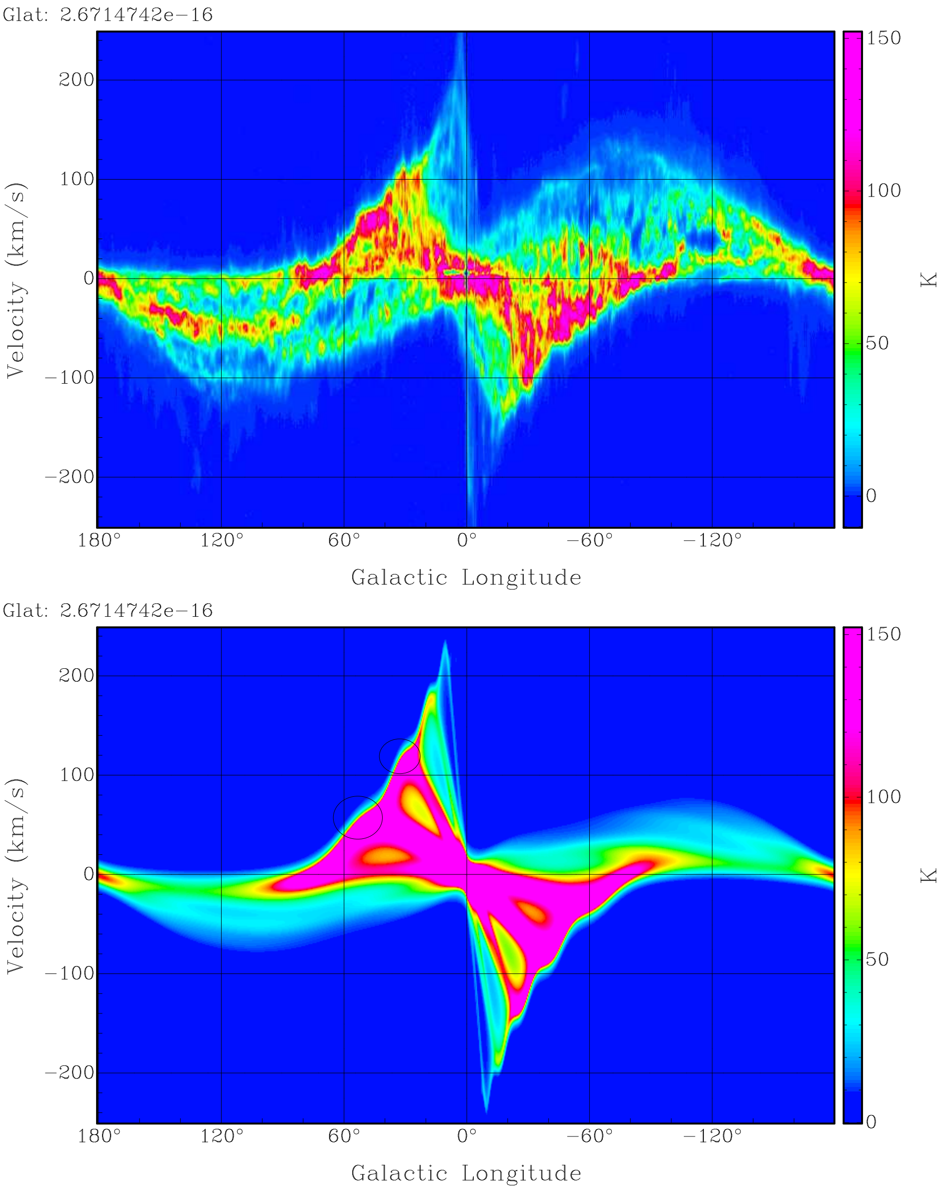

Fig. 3.15: *A comparison of longitude versus* v_{lsr} *(l-v) emission* HI *maps between the LAB data and synthetic data. The black ellipses in the synthetic maps shows region of good agreement between the synthetic and the real data. (a) Top: An* HI *emission map of along the Galactic equator (b=0°) from the LAB survey. (b) Bottom: An synthetic emission map from Model 4 with m=2, contrast=2.65,* $\Omega_p = 13.5$ *km/sec/kpc,* R_o*=3.0kpc,* $\chi_o = 0°$, $\alpha = -1.2482$, $\beta = 0.193$ *.*

3.5 Discussion

In this chapter I have presented my efforts to model the Galactic spiral structure using the linear density wave theory. The purpose of this work is not to produce an accurate

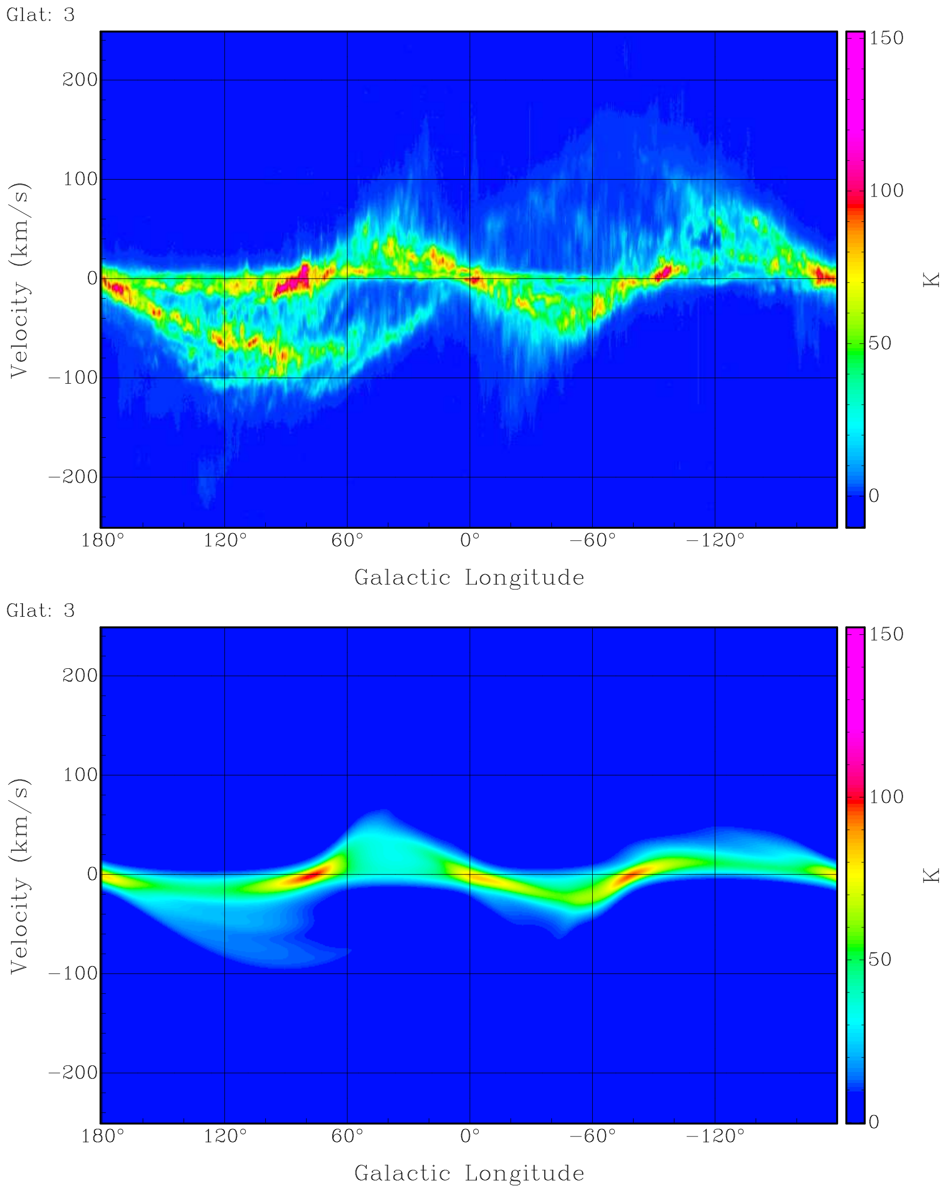

Fig. 3.16: *A comparison of longitude versus* υ_{lsr} *(l-v) emission* HI *maps between LAB data and synthetic data for b=3°. (a) Top: An* HI *emission map for b=3° from the LAB survey. (b) Bottom: An synthetic emission map from Model 4 for b=3° with m=2, contrast=2.65,* $\Omega_p = 13.5$ *km/sec/kpc,* R_o*=3.0kpc,* $\chi_o = 0^\circ$, $\alpha = -1.2482$, $\beta = 0.193$.

and complete model of the real Milky Way spiral arms. My aim is to test the possibility of incorporating the spiral arms structure using the density wave theory in a Milky Way model and to estimate the effect of the velocity perturbations due to the spiral arms in the overall apparent HI brightness distribution in the all sky surveys.

For this reason I have assumed that kinematics are the only dominant factor shaping the line profiles. Then I produced synthetic data cubes to verify this assumption. What is

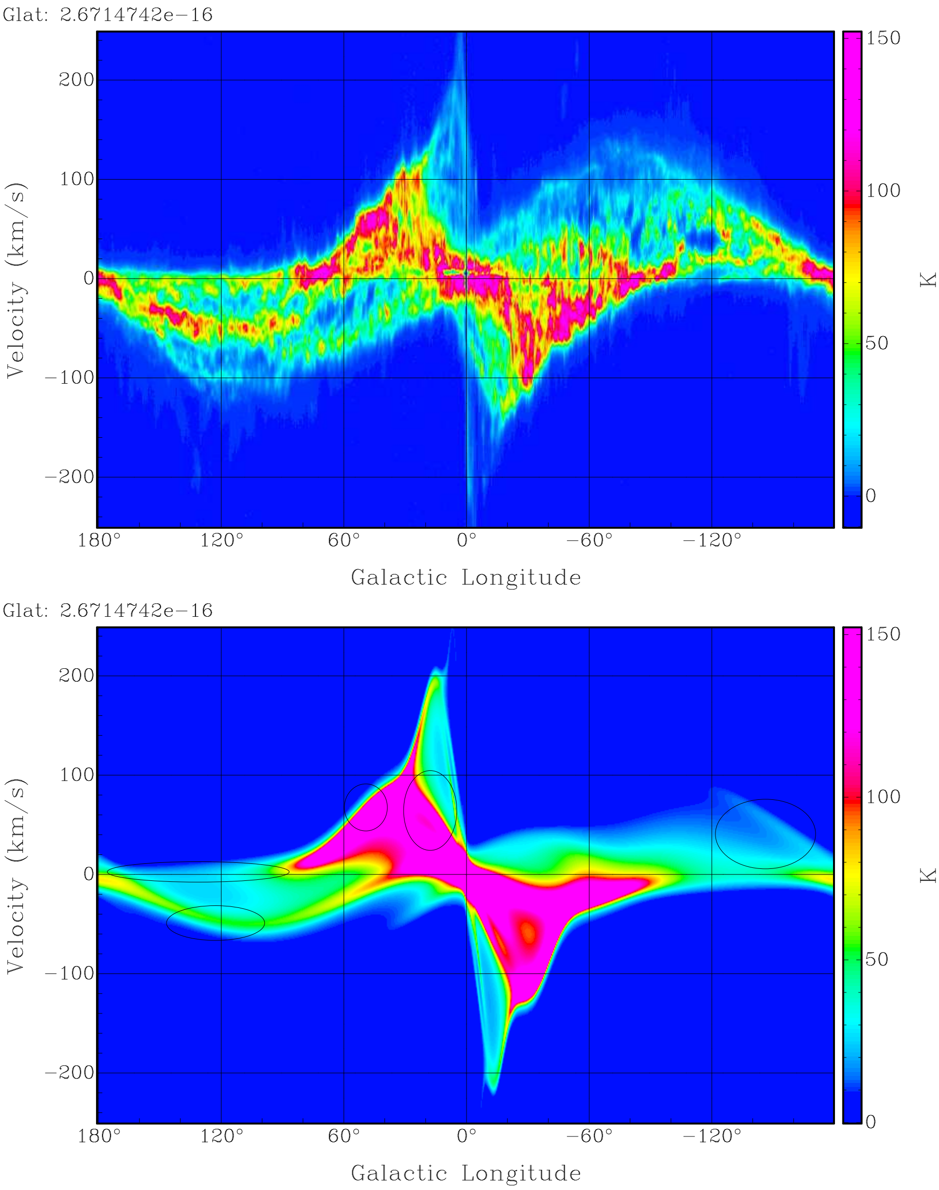

Fig. 3.17: *A comparison of longitude versus* υ_{lsr} *(l-v) emission* H I *maps between LAB data and synthetic data for b=0°.The black ellipses in the synthetic maps shows region of good agreement between the synthetic and the real data. (a) Top: An* H I *emission map for b=0° from the LAB survey. (b) Bottom: An synthetic emission map from Model 5 for b=0° with m=2, Contrast=3,* $\Omega_p = 30$ *km/sec/kpc,* R_o*=3.0kpc,* χ_o*=0°,* $\alpha = -1.070 10^{-2}$*,* β*=0.312.*

apparent is that even in the cases such as the models 2 and 3 where there is no accurate match between observations and synthetic data, it is easy to ascertain that kinematic peculiarities, induced by the linear density wave, create features in the model of the Milky Way which show great similarities with the spiral arms feature seen in the real data. For the more successful models, like 5, 6, 7, this approach can reproduce partially

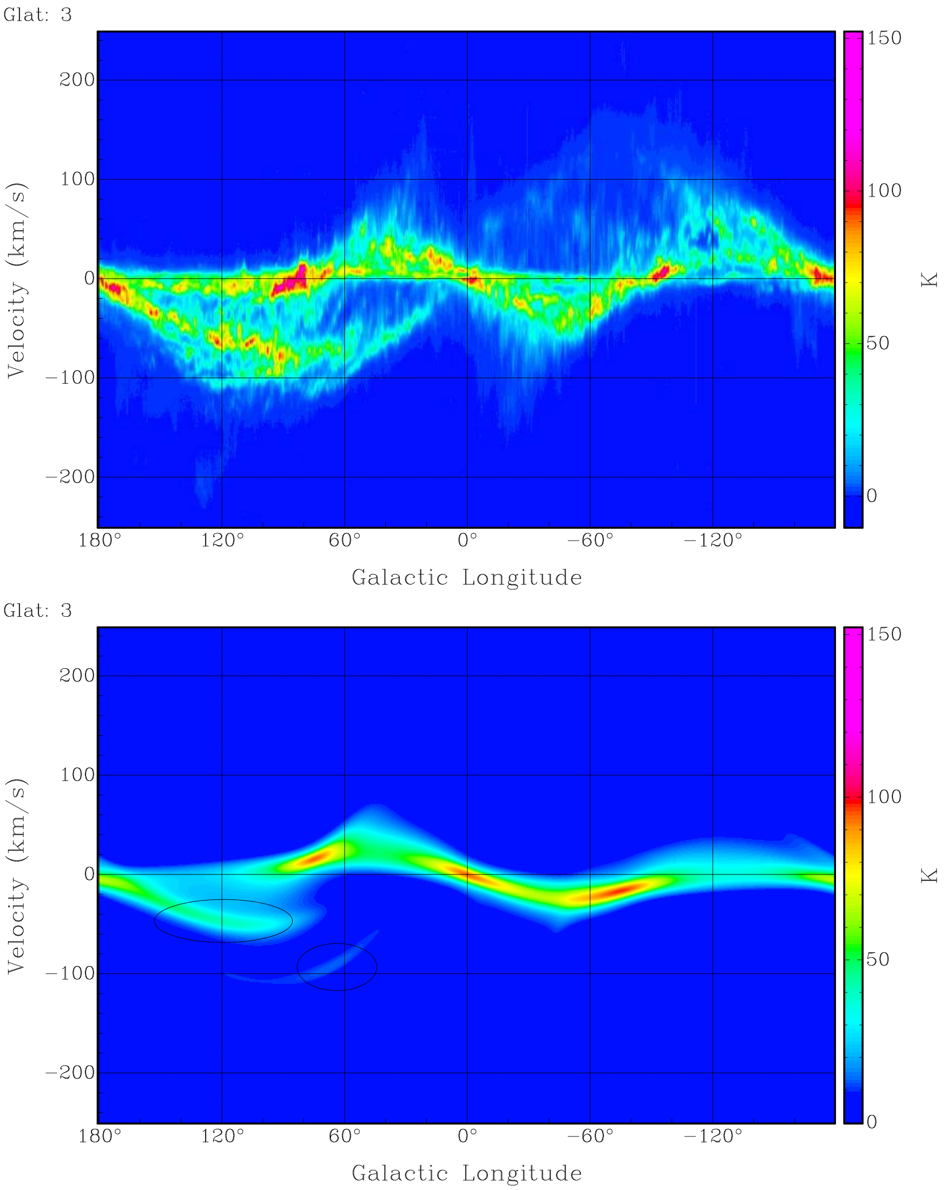

Fig. 3.18: *A comparison of longitude versus* υ_{lsr} *(l-v) emission* HI *maps between LAB data and synthetic data for b=3°. The black ellipses in the synthetic maps shows region of good agreement between the synthetic and the real data. (a) Top: An* HI *emission map for b=3° from the LAB survey. (b) Bottom: An synthetic emission map from Model 5 for b=3° with m=2, Contrast=3,* $\Omega_p = 30$ *km/sec/kpc,* R_o*=3.0kpc,* $\chi_o = 0°$, $\alpha = -1.07010^{-2}$, $\beta = 0.312$.

even the exact location of the spiral structure.

Therefore it is obvious that one should be really careful when interpreting the HI brightness distribution. The kinematic peculiarities are too important to be neglected and as seen in the models they can create velocity structures that may be erroneously interpreted as true density structures. The partial success of the modeling also shows

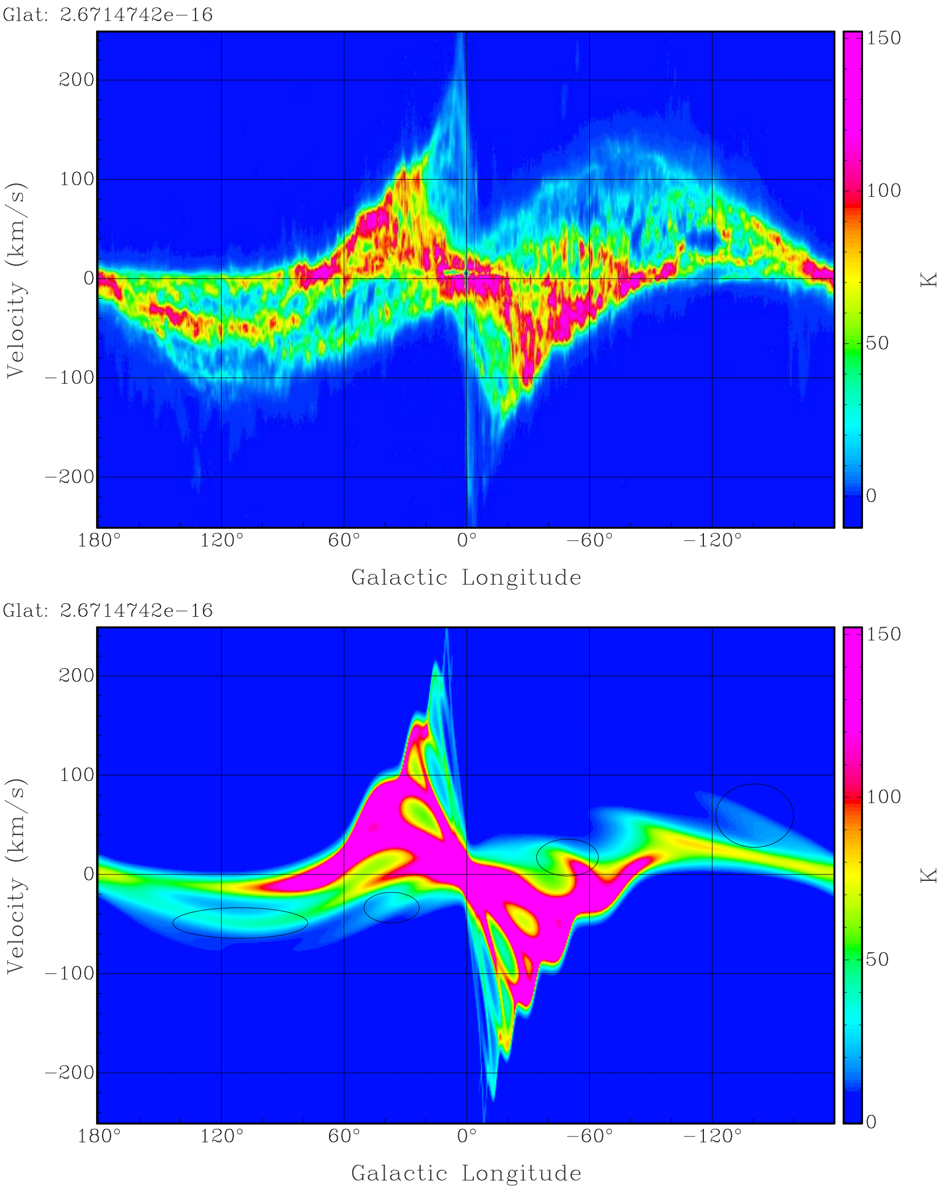

Fig. 3.19: *A comparison of longitude versus* υ_{lsr} *(l-v) emission* HI *maps between LAB data and synthetic data for b=0°. The black ellipses in the synthetic maps shows region of good agreement between the synthetic and the real data. (a) Top: An* HI *emission map for b=0° from the LAB survey. (b) Bottom: An synthetic emission map from Model 6 for b=0° with m=4, Contrast=4,* $\Omega_p = 30$ *km/sec/kpc,* R_o*=3.0kpc,* $\chi_o = 0°$, $\alpha = -1.07010^{-2}$, $\beta = 0.312$

that at least at a first approximation, the linear density wave theory can be used to introduce spiral structure in Galactic models. Not all the features are reproduced accurately but this is probably due to the simplicity of the models used here. More complicated models with separate pitch angles for each spiral, surface density contrast depending on radius and multiple spirals should yield better results. However

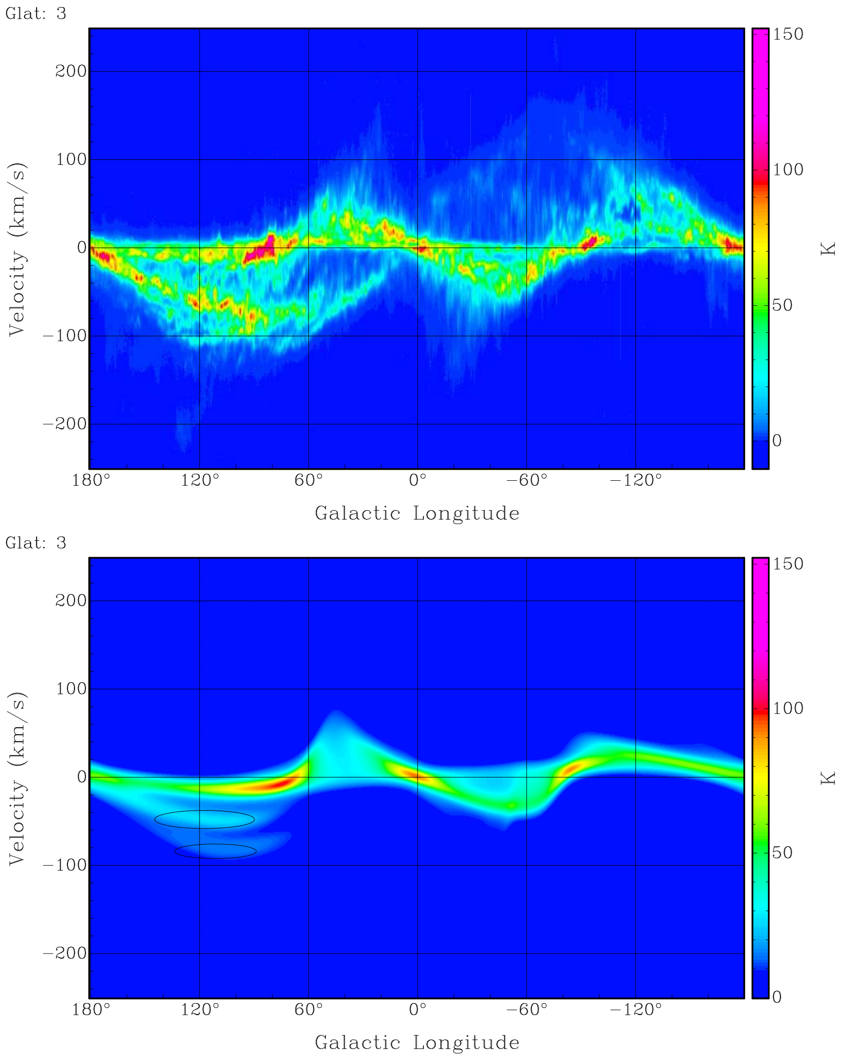

Fig. 3.20: *A comparison of longitude versus* υ_{lsr} *(l-v) emission* HI *maps between LAB data and synthetic data for b=3°. The black ellipses in the synthetic maps shows region of good agreement between the synthetic and the real data. (a) Top: An* HI *emission map for b=3° from the LAB survey. (b) Bottom: An synthetic emission map from Model 6 for b=3° with m=4, Contrast=4,* $\Omega_p = 30$ *km/sec/kpc,* R_o*=3.0kpc,* $\chi_o = 0°$, $\alpha = -1.24828^{-2}$, $\beta = 0.312$

this is beyond the scope of this work. The assumption of the angular pattern speed of $\Omega_p = 30\mathrm{km\,s^{-1}kpc^{-1}}$ measured observationally (Fernández et al., 2001) seems to yield reasonable results.

Regarding the effect of the spiral structure on vertical distribution, our models do not include an explicit dependence on latitude in the form of a third peculiar velocity perpendicular to the plane. Since the spiral arms are considered to be a perturbation from the axisymmetry of the galactic Gravitational field such a velocity affect the model significantly. Nevertheless even without this inclusion it is visible from our models

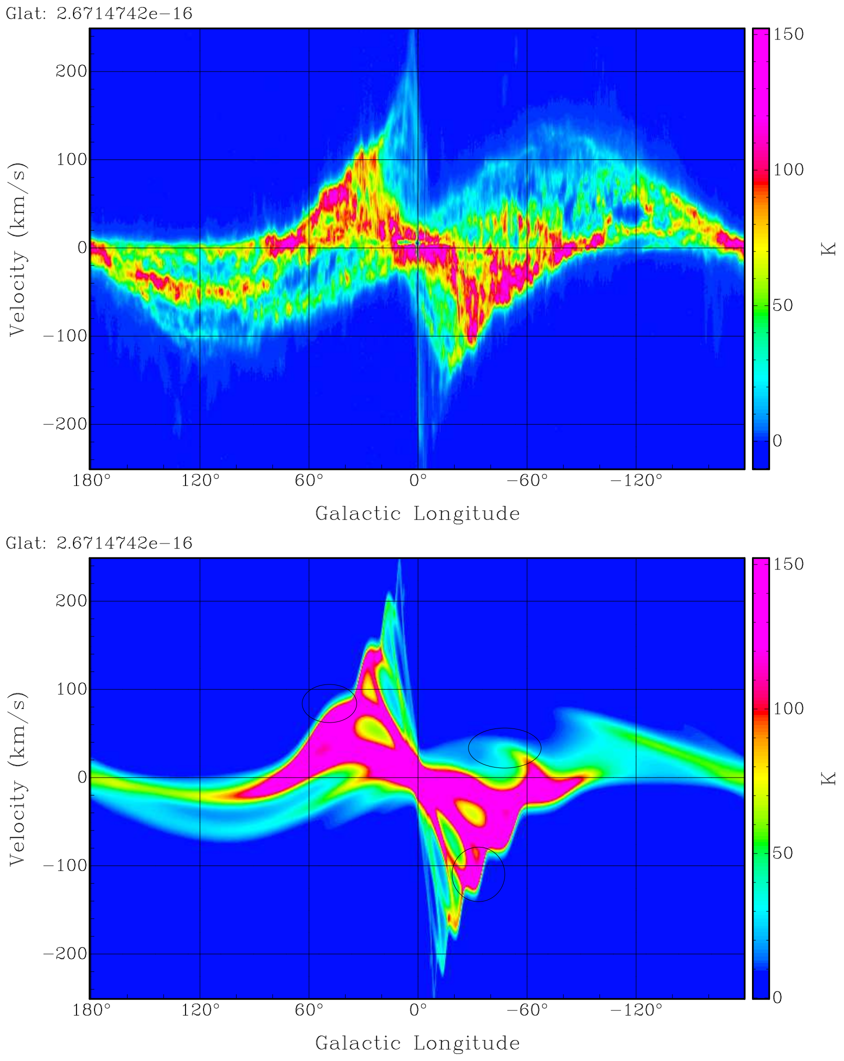

Fig. 3.21: *A comparison of longitude versus* υ_{lsr} *(l-v) emission* HI *maps between LAB data and synthetic data for b=0°. The black ellipses in the synthetic maps shows region of good agreement between the synthetic and the real data. (a) Top: An* HI *emission map for b=0° from the LAB survey. (b) Bottom: An synthetic emission map from Model 7 for b=0° with m=4, Contrast=4,* $\Omega_p = 30$ *km/sec/kpc,* R_o*=3.0kpc,* $\chi_o = 40°$, $\alpha = -1.0701^{-2}$, $\beta = 0.312$

that the spiral structure affects the kinematics and distribution of the HI not only in the Galactic plane but also at low latitudes. Although the models are not adequate for latitudes higher than b=0°, it was clearly shown that the velocity perturbations affects the spectra to latitude up to b=4.5° in the synthetic cubes. In the real data the affected latitudes seem to be up to b=8°. Taking into account the distribution of the HI gas associated with the halo as depicted in Fig. 2.5, spiral arms should have a stronger effect in the inner parts of the Galaxy where gas is associated with the halo even from b=2°. For the outer part outside the solar circle, the HI gas associated with the halo

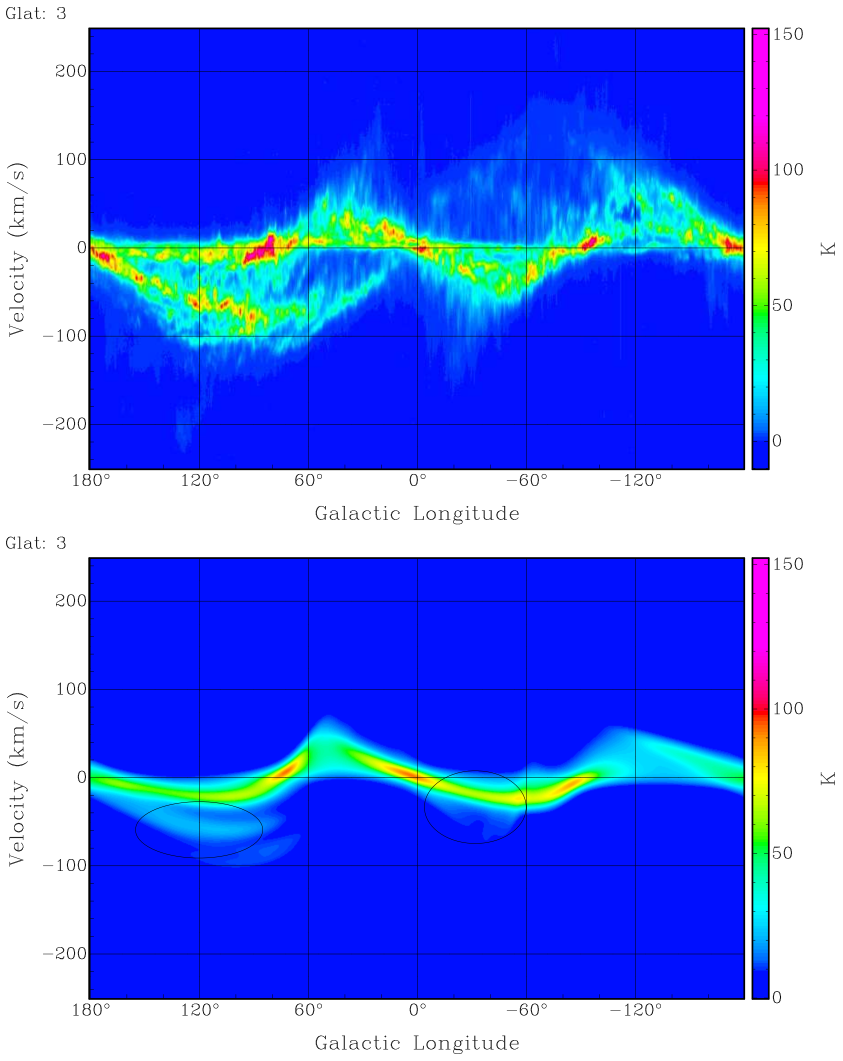

Fig. 3.22: *A comparison of longitude versus* υ_{lsr} *(l-v) emission* HI *maps between LAB data and synthetic data for b=3°.The black ellipses in the synthetic maps shows region of good agreement between the synthetic and the real data. (a) Top: An* HI *emission map for b=0° from the LAB survey. (b) Bottom: An synthetic emission map from Model 7 forb=3°with m=4, Contrast=4,* $\Omega_p = 30$ *km/sec/kpc,* R_o*=3.0kpc,* $\chi_o = 40°$, $\alpha = -1.0701^{-2}$, $\beta = 0.312$

start above b=8°, so it is expected that the spiral perturbation should have a effect on it in a limited vertical range.

Another effect, which was not taken into account but might improve the model, was shock fronts. At a gas temperature of T=100K, for the cold HI temperature, the velocity of sound is $\sim 1-2\mathrm{km\,s^{-1}}$. A simple calculation shows that the peculiar velocities induced by the spiral gravitational potential can be even 10 times greater than this. So the creation of shock fronts can affect the apparent position of spiral arm features.

Finally, it seems that the value $i = 12°$ proposed for the pitch angle of the spiral

	Ω_p $\mathrm{km\,s^{-1}}kpc^{-1}$	C -	m -	α 10^{-2}	β -	χ_o $\circ$	
Model 1	30	4	2	0	0.435	0	Levine et al. (2006b)
Model 2	30	4	4	0	0.435	0	Levine et al. (2006b)
Model 3	30	4	2	0	0.435	6	Levine et al. (2006b)
Model 4	13.5	2.65	2	-1.248	0.193	0	Burton (1971)
Model 5	30	3	2	-1.071	0.313	0	
Model 6	30	4	4	-1.248	0.313	0	
Model 7	30	4	4	-1.071	0.313	320	
Model 8	30	3	4	-1.071	0.313	69	

Tab. 3.2: *A table with the parameters used in the spiral arms models. R_o is the radius where the spiral start in kpc. Ω_p is the angular pattern speed of the spiral in $\mathrm{km\,s}^{-1}kpc^{-1}$. C is the surface density contrast between the arm inter-arm region, m is the number of spiral arms. α and β are the coefficients which define the pitch angle i. χ_o is the initial phase of the galactic spiral arms.*

arms is the most reasonable one. Smaller or larger values do not yield any reasonable results and at least in the case of the linear density wave theory, they can not be used to describe them.

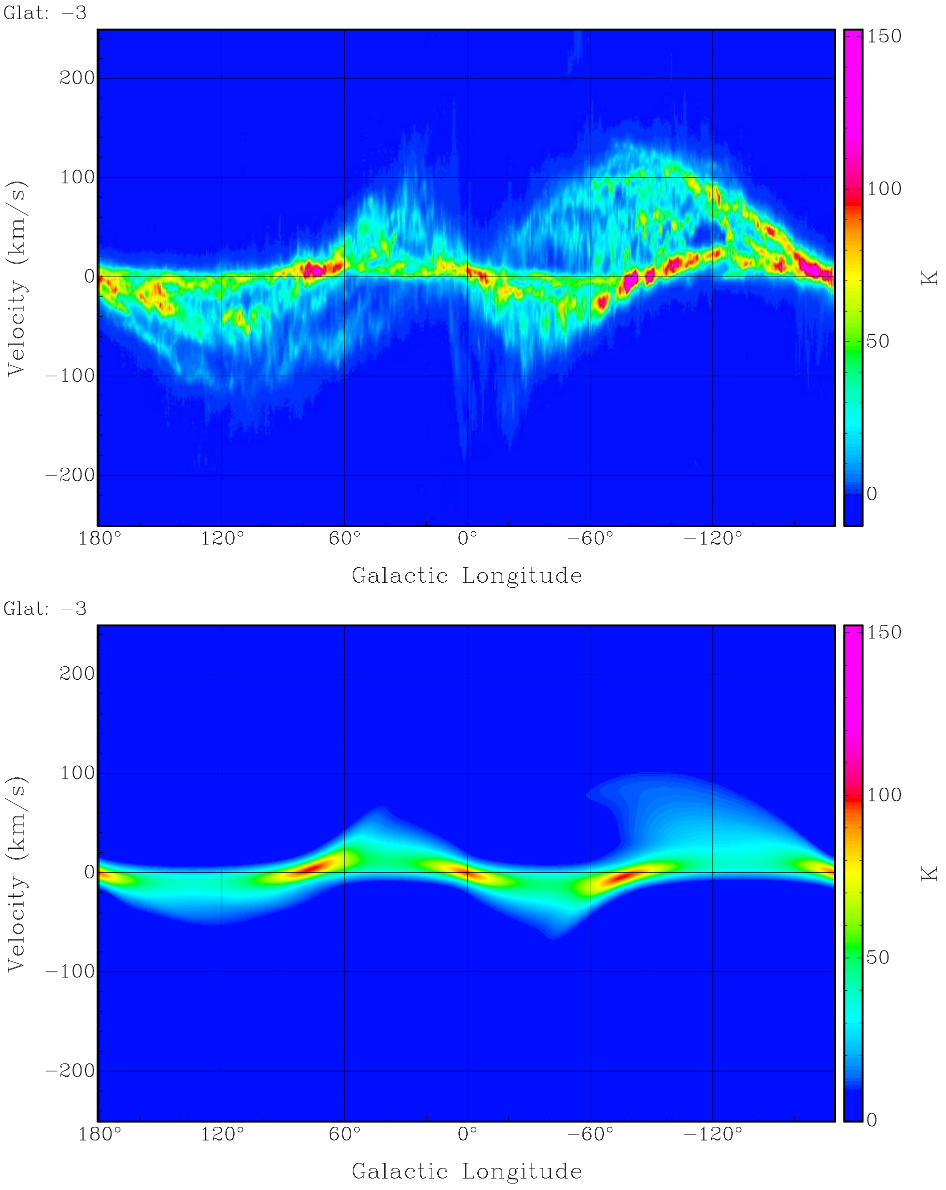

Fig. 3.23: *a) Top: An longitude versus υ_{lsr} brightness temperature* H I *map of the LAB survey at b=-3° (b) Bottom: A longitude versus velocity brightness temperature map of* H I *emission from a Galactic model without spiral arms at b=-3°*

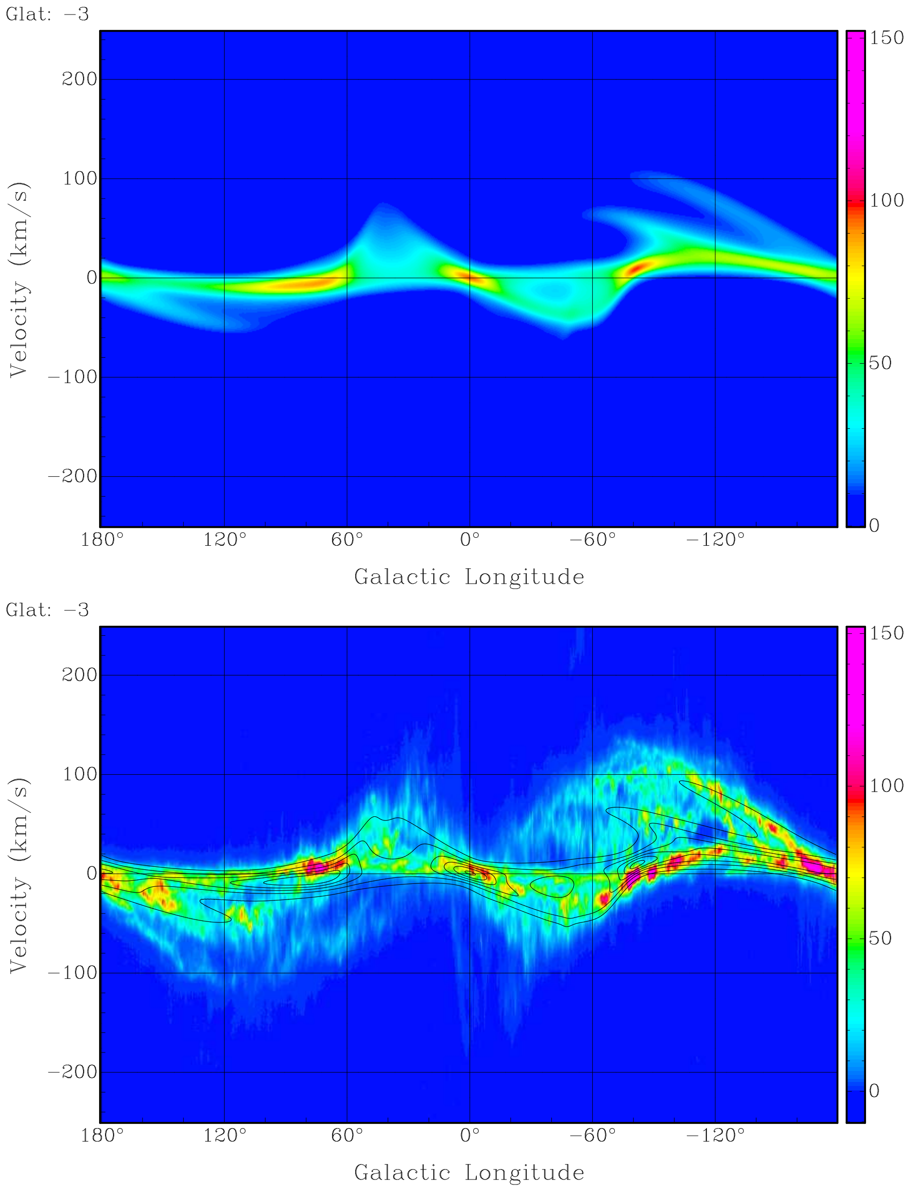

Fig. 3.24: *(a) Top:Model 8 - m=4, Contrast=3,* $\Omega_p = 30$ *km/sec/kpc,* R_o*=3.0kpc,* $\chi_o = -40°$*,* $\alpha = -1.0701^{-2}$*,* $\beta = 0.312$*,* $b = -3°$*(b) Bottom: A comparison between the Lab data and Model 8 for b=-3°. Model 8 is overlaid as contours The - m=4, Contrast=3,* $\Omega_p = 30$ *km/sec/kpc,* R_o*=3.0kpc,* $\chi_o = -40°$*,* $\alpha = -1.0701^{-2}$*,* $\beta = 0.312$*,b=-3°*

4 A search for the structure of the gaseous HI halo using the Effelsberg 100-m telescope

4.1 Introduction

According to the Bonn model (Kalberla & Kerp, 1998), the gaseous Galactic halo has a number of physical properties. To study these properties but also to overcome practical difficulties a simple search strategy was used, utilizing the new all sky HI survey LAB (Kalberla et al., 2005a) as a finding chart. The aim was to identify regions with clumps that can be used to probe the halo. Although the 36′ resolution of the LAB survey is not enough to resolve such clumps, the data are useful to select a number of regions to be observed with higher resolution. The only two telescopes, besides the Green Bank 100-m telescope (GBT) which are able to provide us with the necessary sensitivity and angular resolution are the Arecibo 300m telescope and the 100-m Effelsberg telescope. Due to the limited coverage the Arecibo telescope could not be used to map the initial sample of regions. I started the observations using the Effelsberg 100-m telescope. In the following chapter I will start by giving a brief description of morphological characteristics of the HI clumps as detected by GBT from Lockman (2002). Then I will discuss in more detail two detection made with the Effelsberg radio-telescope which can serve as primary examples of the characteristics of the HI clumps. Then a less detailed description of all my detections will be given and a summary of their physical properties as studied with the Effelsberg radio telescope. Finally I will compare my sample of clumps with the sample from Lockman (2002) from the GBT telescope.

4.2 Technical details and selection criteria

As already discussed, high resolution is needed to detect and start resolving the neutral component of the Galactic Halo. At 21-cm, the beam resolution of the 100-m Effelsberg radio telescope is 9.4′, similar to the beam resolution of the GBT, and enough for a detection of a clump. While the Arecibo telescope has better sensitivity and beam resolution, it can only observe in a limited declination range, objects within a belt of -1°< dec <+39°. This led me to use it as a secondary option.

Using the LAB HI survey, a list of regions were selected, given in Table 11.25. Since the extended faint emission has a brightness temperature T_B of the order of 0.3 K, the parameter of the observations were chosen accordingly to trace the extended emission with the 100-m telescope and to have a good S/N ratio. The parameters used in the observations are given in Table. 4.3.

After the observing run with the Effelsberg 100-m radio telescope I tried to identify the number of clumps in each of the observed fields. The halo clumps as described

Beam Size	$9'$	Sampling	$9'$
No. of Channels	2048	Int.time	60sec
Bandwidth	10Mhz	T_{sys}	27K
Vel. Separation	1.03km s^{-1}	σ_n	0.1K
No. of Polarization	2	Calibrator	S7
Reference	In-Band freq. Switch.	Bas. Correction	1st order
Field size	3°x 3°	Stray Rad. correction	Kalberla et al. (1980)

Tab. 4.3: *The table describes the resources used during the observational campaign with the Effelsberg 100-m radio telescope. The Backend used is the AK-90 auto-correlator. The* σ_n *given is the theoretical estimate for the above parameters.*

by Lockman (2002) have properties quite similar to the cold neutral medium (CNM) phase clumps described in Heiles & Troland (2003a). They are diffuse and show irregular shapes, thus the automated algorithms for the identification of clouds did not work in the observed fields, since these routines are coded for compact molecular clouds with well defined boundaries. The identification of clumps was done manually using a number of criteria associated with the expected properties of the clumps (Chap. 2.2) and the observations of the first H I halo clumps detected in the inner Galaxy by Lockman (2002). The applied selection criteria are the following:

1. **Line-of-sight velocity** υ_{lsr} . Since I am interested in H I halo gas following Galactic rotation I used the Bonn Milky Way mass model (Kalberla et al., 2007) to search for clumps in a υ_{lsr} region connected with a gaseous halo. Lockman (2002), for comparison, observed close to terminal velocity in the inner Galaxy. More detailed analysis is given in Chap.2

2. **Brightness temperature** T_B **; Angular size** s. From Fig. 4.25, depicting H I spectra of representative H I halo clumps observed with GBT, one can make the following assertions. Firstly the clumps are either isolated or embedded in the wing of the main Galactic line. Secondly they are very faint with T_L reaching up to $\sim$ 4K. Regarding their angular size, Lockman (2002) found that 25% are unresolved with GBT and appear as 1-to-2 pixel dots in low resolution surveys like the LDS (Bur, 1998). As seen in Fig. 4.26 some of the clumps have an angular size as low as $15'$ while others are more elongated and can reach up to more than $25'$ in one axis. So as a selection criteria I search for structures unresolved in the LAB survey, i.e. structures with radius less than $36'$. Since the H I halo gas is expected to be faint, the T_B must be less than 5-6K. Clumps can be either isolated or embedded in a surrounding warm medium.

3. **Line-width** $\Delta\upsilon_{1/2}$. As seen in Fig. 4.25 the typical GBT clouds have a $\Delta\upsilon_{1/2} <$ 20 km s^{-1} , implying a kinetic temperature of $T_{kin} \sim$ 8200 K. So as a final criteria I selected objects with a line-width less than 20 km s^{-1}.

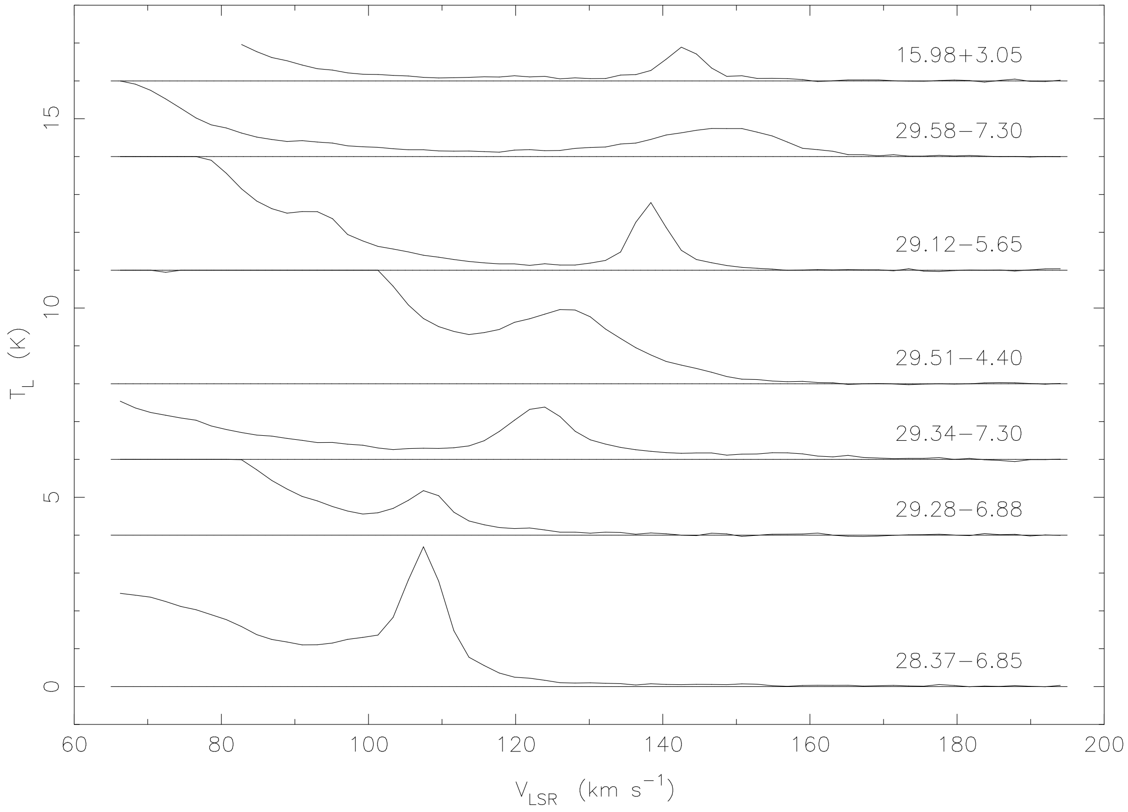

Fig. 4.25: HI *spectra toward the center of representative* HI *halo clouds observed with the GBT telescope (Lockman, 2002).*

4.3 The clump 116.20+23.55

I will describe in detail and give a thorough analysis of one of the most representative HI halo clumps detected with the Effelsberg 100-m Radio telescope. This clump was also a target of high resolution follow-up observations using the Westebork synthesis radio telescope (W.S.R.T) .

Using the criteria described in the previous section I have identified a clump at Galactic longitude l=116.20°, galactic latitude b=23.55°and υ_{lsr} =-68km s^{-1} . Fig. 4.27 is the HI spectrum towards the center of the clump and Fig. 4.28 shows two position-velocity maps around the HI clump. Using these three plots, I will describe first its morphology which is typical also for the other HI clumps. First of all, as can be seen clearly in the spectrum of the clump (Fig.4.27) and the longitude-velocity diagram (Fig. 4.28a), the very narrow line emission representing the HI halo clump is surrounded by a very extended (>1°), very broad emission ($\Delta\upsilon_{1/2}$~20 km s^{-1}). In the latitude-velocity diagram (Fig. 4.28b.), the clump is slightly more elongated along latitude and it is related in velocity with the clump 116.66+22.80, also surrounded by the same extended emission. This morphology configuration describes best most of the

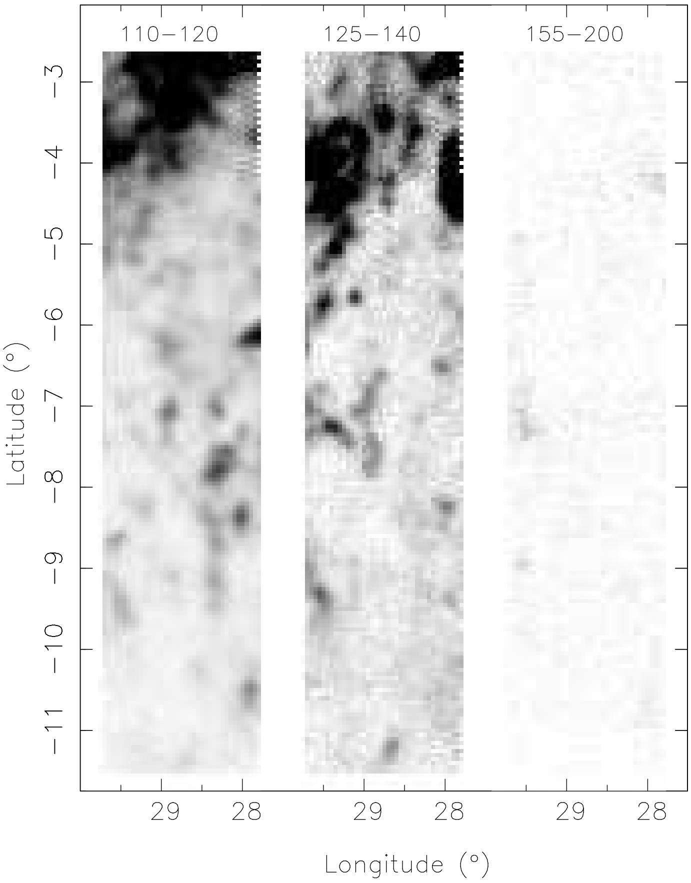

Fig. 4.26: *GBT* HI *observation depicting the clumpy* HI *halo. The* HI *emission is integrated in each of the panel over the velocity range given above it. It is interesting to note the absence of clumps at the extreme velocities. Taken by Lockman (2002).*

clumps of my sample. There exists a broad, very extended faint emission representing the warm envelope. In it there are embedded one or more narrow compact HI clumps, that can be slightly elongated along one axis. This structure configuration is more similar to the two-component sheet-like clumpy structure of the CNM described in Heiles & Troland (2003b) than the raisin-pudding model described in the same paper.

Regarding the physical properties of the HI clump itself, I follow the method outlined in Chap. 2.6. The line of sight velocity is υ_{lsr} =-68km s^{-1}. As discussed earlier, since the gas is following the Galactic rotation, I can estimate its distance using the υ_{lsr} and the velocity field of the Milky Way. The Bonn mass model (Kalberla et al., 2007), described in Chap. 2, gives a distance for the clump of 7kpc, accordingly it is located at Galactocentric radius R=12.7 kpc and at a height above the plane z=2.8 kpc. To estimate the uncertainty in the distance determination I utilized three Milky Way models. All the three are assuming that the gaseous Milky Way halo is co-rotating with the Galactic disk, in contrast with the Bonn Mass model which assumes a lagging halo

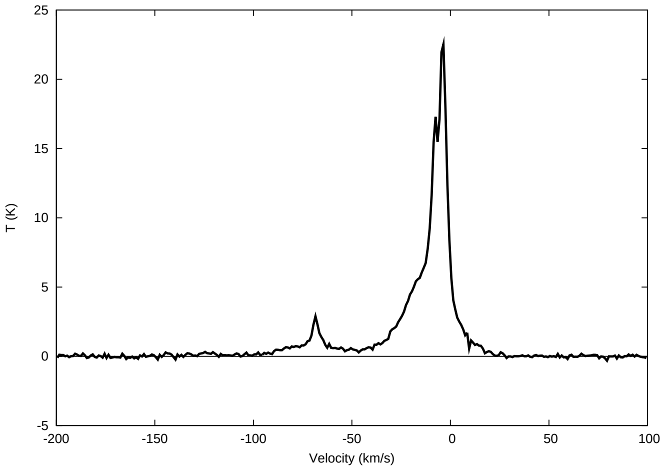

Fig. 4.27: HI *spectrum towards the center of the clump 116.20+23.55 taken with the 100-m Effelsberg Radio-telescope. The peak of* T_B *at velocity* υ_{lsr} *=-68km* s^{-1}*comes from the cloud.*

(Kalberla et al., 2007). This assumption for the kinematical state of the gaseous Galactic halo imposes an uncertainty between the non co-rotating model and the co-rotating models since the translation of the velocity υ_{lsr} to distance will be intrinsically different. The first model, which is a modified Bonn mass model to include co-rotation, gives 17% higher value for the distance estimate of the clump. This result can account for the intrinsic difference in the distance estimate between a lagging halo model and a co-rotating model. The second model uses a Brand & Blitz (1993) rotation curve giving 24% higher value than the Bonn standard model. Finally the third model from Gómez (2006) results in a 7% smaller distance. The Brand & Blitz (1993) rotation curve is the most widely used rotation curve for the Milky Way therefore I will utilize as a measure of uncertainty for the Bonn-model distance determination.

The total brightness temperature T_B at the central position of the clump is 2.89±0.06K. The diameter D of the HI clump is defined as the square root of the diameter along the latitude and longitude. For 116.20+23.55 the diameter can be taken from the position-velocity plot and it is s=25′±9′. The uncertainty in the diameter is due to the 9′ sampling in the observing strategy. Using a Gaussian decomposition I extracted the different parameters for the HI clump and the surrounding warm envelope. For the narrow component the peak temperature is T_C=1.8±0.1K and the column density is N_C=11±2$\cdot$ 10^{18} cm^{-2} while for the broad envelope the peak temperature is T_W=0.71±0.1 K and the column density is N_W=25±4$\cdot$ 10^{18} cm^{-2}. The ratio of T_C over T_W is more than 2.5 while the ratio of the column densities N_C and N_W over the total column density is 0.3 and 0.7 respectively. This implies that while the broad envelope is indeed very faint it seems that a significant fraction of the neutral gas mass is associated with it. From the Gaussian decomposition the line width of the clump is estimated to be $\Delta\upsilon_{1/2}$=3.0±1 km s^{-1}, implying a kinetic temperature of T_{kin}=200±70K while for the broad envelope the kinetic temperature is as high as T_{kin}=7200±400K. Since both

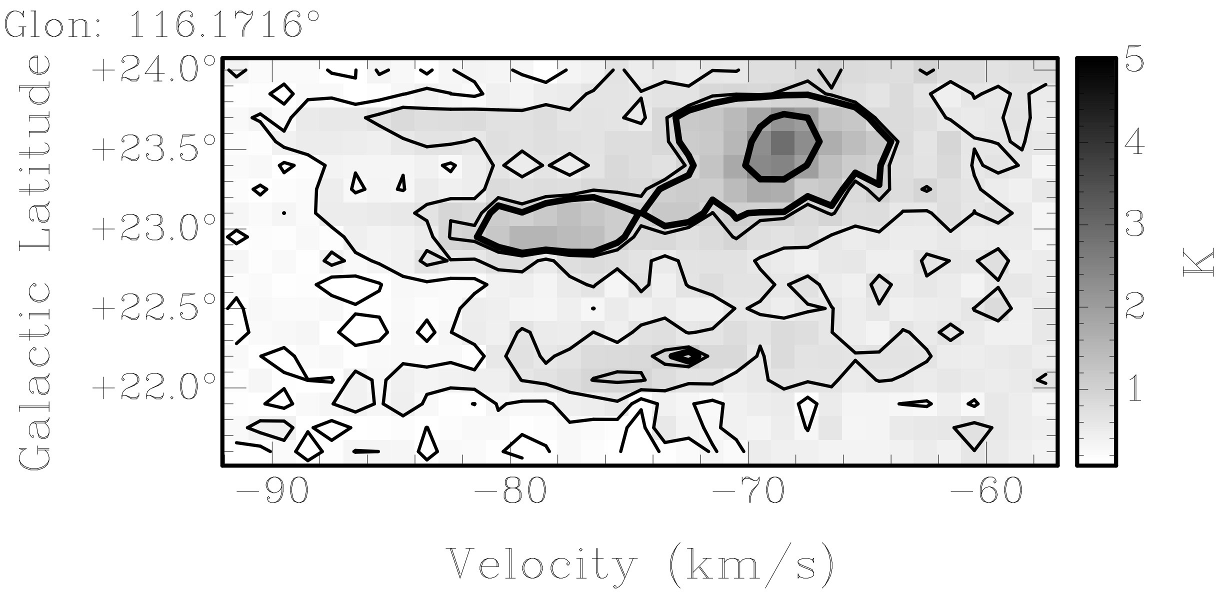

Fig. 4.28: *A latitude-velocity* HI *brightness temperature map of the clumps 116.20+23.55 taken by the Effelsberg 100-m telescope. The σ_n is 0.1K. The color-bar displays the transfer function. The contour are at the level of 0.1K 0.3K 0.6K 0.9K 1K 2K.*

of these estimated temperatures do no take into account the effect of turbulence, the thermal temperature should be significantly lower than this value.

Since I have an estimate of the distance and the diameter of the HI clump I can also calculate the spatial dimensions of the clump, its volume density and thus its pressure and its mass. For a distance of 7kpc, the spatial diameter of the clump is D=51±17pc. The volume density of the clump is then estimated to be $< n >$=0.07±0.03 cm^{-3}. Thus the visible HI mass associated with the narrow component, the clump, is estimated to be M=120±80 M$_\odot$and the pressure of the clump equals P=14±8 $K \cdot$ cm^{-3}. According to Rohlfs & Wilson (2004) the virial relation is:

$$M = 250 \cdot \Delta\upsilon^2 \cdot R$$

where M is the mass in M$_\odot$, $\Delta\upsilon^2$ is the $\Delta\upsilon_{1/2}$ in km s^{-1} and R is the radius in pc. So for the clump 116.20+23.55, $M_{vir} = 57400$M$_\odot$ which is orders of magnitude larger. This means that the clumps is not self-gravitating but must be confined by an external medium. This confining element can take the form of the surrounding extended warm envelope. Assuming that the clump is surrounded by an envelope of gas of the same size, then the volume density of the envelope is $< n >$=0.16±0.07cm^{-3} implying a pressure P=1151±507$K \cdot$ cm^{-3}. It is obvious that the clump is under-pressured in comparison with the external warm envelope.

A comparison between the T_B measured in the Effelsberg spectrum and the T_B from the LAB survey at the same position is a measure of the presence of small scale substructure in the clump. At the center the brightness temperature T_B in the LAB survey

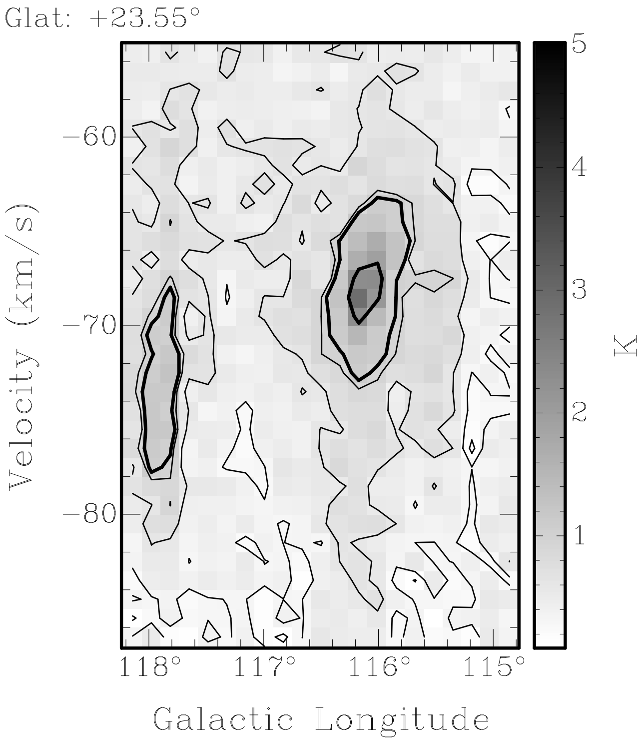

Fig. 4.29: *A longitude-velocity* HI *brightness temperature map of the clumps 116.20+23.55 taken by the Effelsberg 100-m telescope. The* σ_n *is 0.1K. The color-bar displays the transfer function. The contour are at the level of 0.1K 0.3K 0.6K 0.9K 1K 2K.*

is 0.9K. The ratio between the clump peak temperature T_C, the peak temperature of the warm component T_W and the brightness temperature T_B in Effelsberg over the T_B in the LAB survey is 2.02±0.11, 0.78±0.11 and 3.25±0.11 respectively. Since the ratio of the warm component temperature T_W over the LAB T_B is 0.78±0.11, it seems that the warm extended enveloped is resolved with the Effelsberg telescope. If the clump is considered an isolated point source then the ratio of the brightness temperature in Effelsberg T_B over the T_B in LAB should be close to 16. This is far from the ratio of 3.25 found here. Still this does not exclude the presence of small scale sub-structure as explained in Chap. 12. If the HI clump is constituted of HI cores bathed in an extended medium with lower source temperature then such low ratios are to be expected. In such a case the cores would be denser, thus having a higher pressure which could counterbalance the pressure from the surrounding medium. To resolve this issue, follow-up high resolution observations were done using the W.S.R.T array.

4.4 The clump 115.00+24.00

In this section I will give a description of the properties of the second typical HI halo clump. Initially it was detected using the Effelsberg 100-m telescope and later follow-

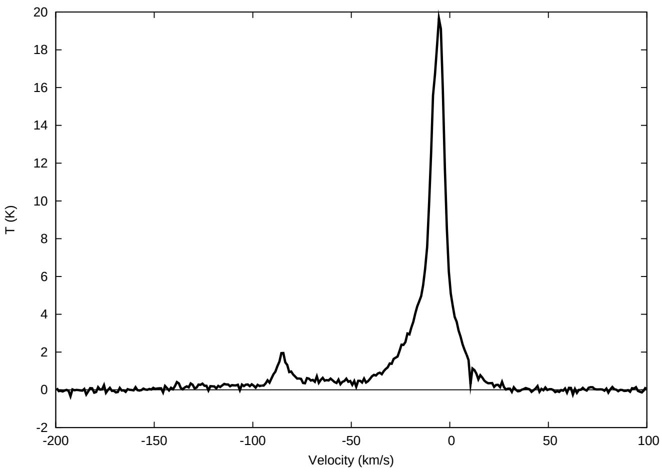

Fig. 4.30: HI *spectrum towards the center of the clump 115.00+24.00 taken with the 100-m Effelsberg Radio-telescope. The peak of* T_B *at velocity* υ_{lsr} *=-84.5km* s^{-1} *comes from the cloud.*

up observation were done using the Very Large Array (VLA) synthesis telescope.

The clump 115.00+24.00 was detected at l=115.00° and b=24.00° at υ_{lsr} =-84.5 km s^{-1} with peak brightness temperature T_B =1.94±0.04 K. Fig. 4.30 shows the spectrum towards the center of the HI clump. Fig. 4.31, 4.32 are brightness temperature maps observed with the Effelsberg 100-m telescope. A comparison between these two figures and Fig. 4.29, 4.28 show that clumps 115.00+24.00 and 116.20+23.55 have a similar morphology. While the clump 115.00+24.00 is fainter, it is still constituted by a narrow cold compact component with a non isotropic shape slightly elongated towards the latitude axis. The broad envelope of 115.00+24.00 is similar, it is warm more extended than the clump itself and it seems to be part of a very broad and extended warm component which forms a common envelope around a lot of clumps. This morphological evaluation agrees very well with the Clumpy Sheet model for the C.N.M by Heiles & Troland (2003b). A more elaborate discussion of the two models and their connection with the HI will follow in Chapt. 9.

The physical properties were estimated from the observational method described in Chapt.2 and in the previous section. With a line-of-sight velocity υ_{lsr} =-84.5 km s^{-1}, the HI clump following Galactic rotation, lies even further out at a distance d=9±2 kpc with a Galactocentric radius R=14.5 kpc and at a height z of 4 kpc. The uncertainty in the distance in comparison with the Brand & Blitz (1993) is 26.3%. The mean angular diameter is $s=22'\pm4.5'$, implying a spatial diameter of the HI clump of D=60±20pc. The Gaussian decomposition shows that the peak temperature of the clump is T_C=0.73±0.1 K while the peak temperature for the warm envelope is T_W=0.8±0.1 K. The estimated column density for the clump is N_C=15±3 10^{18} cm^{-2} while for the warm extended envelope it reaches N_W=20±4 10^{18} cm^{-2}. This implies a ratio of column density between the HI clump and the total column density of 0.42, showing

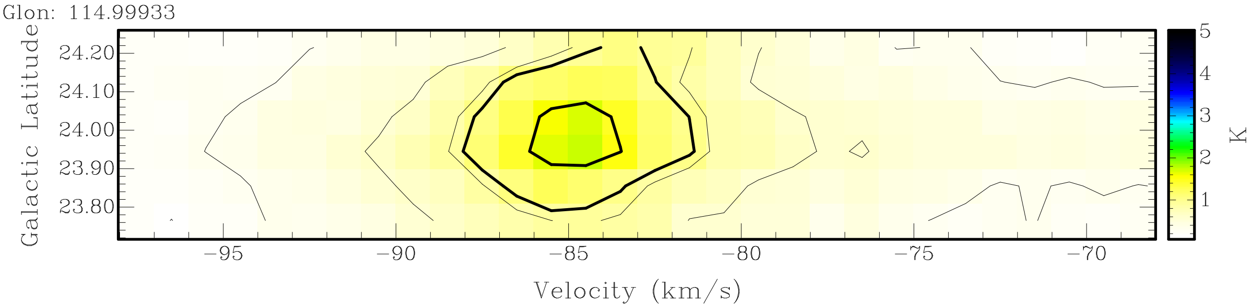

Fig. 4.31: *A latitude velocity* HI *brightness temperature maps of the clumps 115.00+24.00 taken by the Effelsberg 100-m telescope. The σ_n is 0.1K. The color-bar displays the transfer function. This map is the result of follow up observation with the same telescope done with full sampling. Each pixel represents 4.5′.*

that an important percentage of the mass is in the warm extended envelope. Regarding the kinetic temperature of the clump T_{kin}, a $\Delta\upsilon_{1/2}$=3.3±1km s^{-1} implies a temperature of T_{kin}=240±70 K while for the surrounding envelope the kinetic temperature for $\Delta\upsilon_{1/2}$=15±1 km s^{-1} is T_{kin}=4950±330 K. For an average volume density of the HI clump of $< n >$=0.08±0.03 cm^{-3}, I estimated a pressure of P=19±7 $K \cdot$ cm^{-3} and a visible HI mass of M=220±140 M$_{\odot}$. For the extended envelope the pressure is P=535±211$K \cdot$ cm^{-3}, showing that also this HI clump is significantly under-pressured.

A comparison between the Effelsberg spectrum and the LAB spectrum towards the 115.00+24.00 clump shows that the ratio of brightness temperatures is 3.27 yet again lower than the ratio of 16 expected for point sources. As before, the presence of an extended envelope and the necessity of higher pressure P for the clump to be stable points towards the presence of sub-structure in the clump. To study this I have made follow-up observation of the clump with the VLA telescope which are going to be presented in Chap.5

4.5 Effelsberg sample of HI halo clumps.

The examples in the two previous sections give a characteristic description of the physical properties and the morphology of the HI halo clumps. I will discuss here the general properties of the HI clumps detected with the Effelsberg 100-m telescope and I will compare them with the observation of the clumps by Lockman (2002) who used the GBT 100-m telescope.

In total I have observed 22 fields, in a velocity range from υ_{lsr} =-200 km s^{-1} up to υ_{lsr} =150 km s^{-1}. The total area covered is 204 deg^2. From these fields we have detected HI objects which can be identified as halo clumps in 8 fields, covering a total area of 86 deg^2, which constitutes 42% of the total area covered by the telescope. In

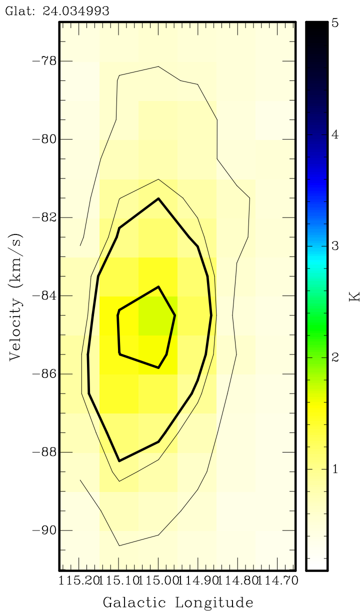

Fig. 4.32: *A longitude-velocity* HI *brightness temperature map of the clumps 115.00+24.00 taken by the Effelsberg 100-m telescope. The σ_n is 0.1K. The color-bar displays the transfer function. This map is the result of follow up observation with the same telescope done with full sampling. Each pixel represent 4.5′.The contour are at the level of 0.1K 0.3K 0.6K 0.9K 1K 1.5K.*

the two fields in the inner galaxy I detected very extended faint diffuse structures with line width of $\Delta\upsilon_{1/2}$>20km s^{-1}. For the fields with longitude *l* greater than 130° there was no detection of HI clumps, only very extended and bright emission with T_B ∼12K associated with high velocity clouds.

Using the selection criteria described earlier, I have identified 26 HI objects as HI halo clumps in the observed fields. If we define as coverage of clumps per field *w* the ratio between the number of clumps found in the field over the area of the field in degrees, I find that the average coverage of clumps is *w*=0.30 deg^{-2}. The lower coverage *w* observed in a area is 0.11 deg^{-2} while the highest is 0.66 deg^{-2}. No specific association is found between the position of the observed field and the number of HI clumps detected.

In Fig. 4.33, a selection of the most typical spectra of the HI halo clumps is shown. The rest of the spectra are found in Appendix 11. The observable parameters of all the Effelsberg sample HI clumps are given in Table. 4.4. The error in the measurement is of the order of 2%. The physical properties are given in Table. 4.5. For all the properties, except the kinetic temperature T_{kin}which is independent of the distance, the accuracy is determined by the uncertainty in the distance determination which is maximum of the order of 30% (9).

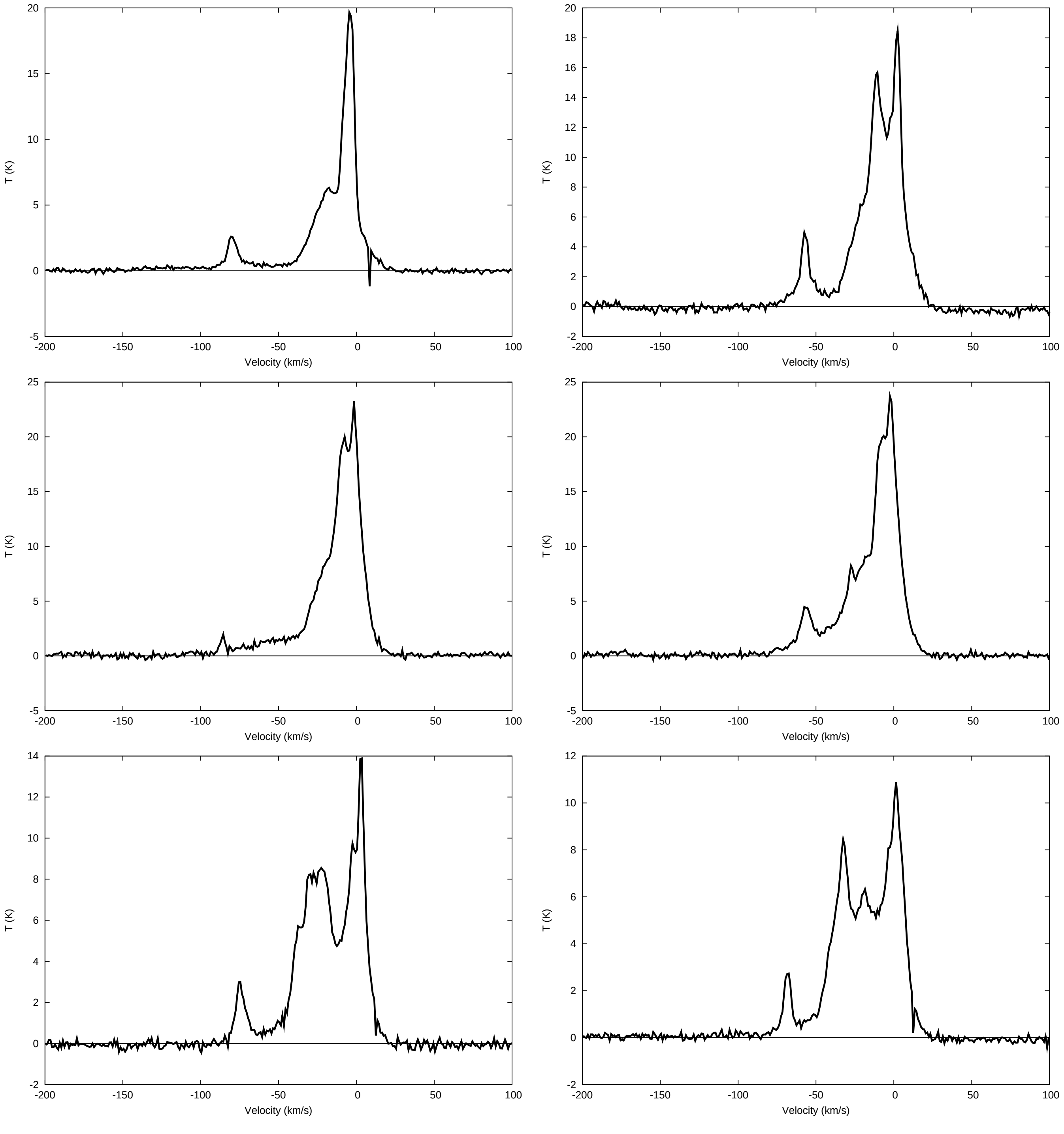

Fig. 4.33: *Spectra of* HI *clumps detected using the Effelsberg telescope. a) Top Left:116.66+22.95 b) Top Right: 113.26-14.07 c) Middle Left:113.57-12.44 d) Middle Right:112.96-12.44 e) Bottom Left:130.98-19.22 f) Bottom Right: 130.65-19.51*

	υ_{lsr} km s^{-1}	T_C K	$\Delta\upsilon_{1/2}$ km s^{-1}	s arcmin	N_{HI} 10^{18} cm^{-2}
113.33+27.00	-40	1.0	7.0	13	16(2)
113.16+25.49	-32	1.1	~ 4	9	6(1)
116.20+23.55	-68	1.8	3.0	25	11(2)
116.66+22.80	-81	2.5	5.1	27	25(3)
116.50+21.45	-42	3.2	5.4	13	36(4)
115.00+24.00	-84	0.7	3.3	22	15(3)
115.35+22.35	-66	1.7	10.0	18	35(3)
117.32+24.00	-71	2.0	8.1	27	36(3)
118.01+24.59	-71	1.3	5.0	18	20(3)
117.97+24.00	-72	1.8	21.1	18	74(4)
117.51+25.19	-74	2.1	11.6	18	60(4)
114.50-15.85	-38	1.2	~ 4	18	10(2)
113.57-12.44	-85	2.0	~ 4	13	16(2)
112.96-12.44	-55	2.6	6.7	18	41(3)
112.96-13.03	-40	2.7	4.4	9	28(3)
113.26-14.07	-57	3.5	4.9		39(4)
113.57-13.48	-50	3.9	7.0		68(5)
114.32+21.74	-75	0.7		9	7(-)
128.84-18.48	-58	4.8	4.8		54(6)
130.98-19.22	-72	3.6	5.4		49(5)
130.65-19.51	-68	2.7	6.0		35(3)
112.10+27.79	-39	0.7	5.3	9	6(1)
113.84+28.70	-69	0.5	$\sim$6.0	18	9(2)
112.45+29.90	-65	0.6	$\sim$2.0	9	4(1)
114.71+29.60	-89	1.8	3.6		19(3)

Tab. 4.4: *Observational parameters of observed* HI *halo clumps.* υ_{lsr} *is the line-of-sight velocity.* T_C *is the peak temperature of the clump.* $\Delta\upsilon_{1/2}$ *is the line width.* s *is the angular size and* N_{HI} *is the observated* HI *column density of the clump*

First of all, as estimated from their υ_{lsr} all the clumps are located at a Galactocentric radius R>8.5 kpc. As seen in their spectra but also from Table. 4.5 of their physical properties, about 84% of the clumps show narrow line widths with $\Delta\upsilon_{1/2}$<10 km s^{-1} while the remaining clumps have larger line width with $\Delta\upsilon_{1/2}$ up to 21 km s^{-1}. This implies that in most of the clumps the kinetic temperature is less than 2200K, so the gas must be associated with the cold neutral medium. Generally the warmer clumps are more massive with a total visible HI mass of up to 700 $M_\odot$. All the clumps seem to be rather diffuse with average volume densities $< n >$ not exceeding 1 cm^{-3}. A striking detail in all the spectra of the HI clumps is that they are

	d	R	z	D	T_{kin}	$< n >$	P	M_{Hi}
	kpc	kpc	kpc	pc	K	cm^{-3}	$K \cdot cm^{-3}$	$M_{\odot}$
113.33+27.00	4.0(1.0)	10.5	1.8	16(7)	1080(150)	0.33(0.15)	360(170)	25(22)
113.16+25.49	3.0(1.0)	10.0	1.4	8(5)	350(90)	0.23(0.14)	80(50)	3(4)
116.20+23.55	7.0(2.0)	12.5	2.8	51(17)	200(70)	0.07(0.03)	14(8)	120(80)
116.66+22.80	9.0(2.0)	14.5	3.5	70(19)	570(110)	0.12(0.04)	68(26)	770(440)
116.50+21.45	4.0(1.0)	10.5	1.5	14(6)	650(120)	0.70(0.30)	455(210)	45(39)
115.00+24.00	9.5(2.0)	14.5	3.9	60(20)	240(70)	0.08(0.03)	19(7)	220(140)
115.35+22.35	6.5(1.5)	12.0	2.5	34(12)	2200(220)	0.33(0.12)	730(275)	260(180)
117.32+24.00	7.5(2.0)	13.0	3.0	58(18)	1440(170)	0.20(0.06)	290(90)	770(490)
118.01+24.59	7.5(2.0)	13.0	3.1	40(15)	550(110)	0.16(0.07)	87(40)	200(150)
117.97+24.00	7.5(2.0)	13.0	3.0	40(15)	9800(460)	0.60(0.22)	5800(2140)	750(550)
117.51+25.19	7.5(2.0)	13.0	3.0	40(15)	2960(260)	0.48(0.18)	1449(550)	600(440)
114.5-15.85	3.5(1.0)	10.5	-1.0	18(7)	350(90)	0.18(0.08)	62(31)	20(16)
113.57-12.44	9.0(2.0)	14.5	-1.9	35(14)	350(90)	0.14(0.06)	50(25)	120(100)
112.96-12.44	5.5(1.0)	12.0	-1.2	28(9)	987(150)	0.49(0.16)	470(170)	205(130)
112.96-13.03	3.5(1.0)	10.5	-0.9	9(5)	425(100)	1.02(0.32)	435(170)	14(16)
113.26-14.07	5.5(1.0)	12.0	-1.3		510(100)			
113.57-13.48	5.0(1.0)	11.5	-1.3		1080(150)			
114.32+21.74	8.0(2.0)	13.5	3.0	21(12)				
128.84-18.48	6.0(1.0)	14.0	-1.9		510(100)			
130.98-19.22	8.5(2.0)	15.0	-2.8		640(120)			
130.65-19.51	7.5(2.0)	14.0	-2.5		780(130)			
112.10+27.29	4.0(1.0)	10.5	1.8	10(6)	620(120)	0.20(0.12)	126(80)	4(5)
113.84+28.70	7.5(2.0)	12.5	3.6	39(14)	790(130)	0.08(0.03)	61(25)	90(70)
112.45+29.90	7.5(2.0)	12.5	3.7	20(11)	80(40)	0.07(0.04)	6(5)	11(13)
114.71+29.60	11.0(3.0)	15.0	5.4		285(80)			

Tab. 4.5: *Physical parameters of the observed* HI *halo clumps.* d *is the distance from the Sun.* R *is the galactocentric distance.* z *is the height above the plane.* D *is the spatial diameter.* T_{kin} *is the kinetic temperature.* $< n >$ *is the volume* HI *density.* P *is the pressure of the* HI *gas.* M_{Hi} *is visible* HI *mass of the clump.*

not truly isolated. In Fig. 4.33 the narrow line associated with the clumps is “embeded” in a more broad line which is connected with the main Galactic line. This broad emission is associated with a very extended, very diffuse envelope which seems to surround the clumps. Such an extended component could potentially play the role of a surrounding envelope which would confine and stabilize the HI clumps. Since stray radiation correction removes all spurious emission from the wings of the Galactic line, the presence of such an extended wing in the spectra is real, even for Lockman (2002) GBT observations.

Assuming the clumps were isolated, the internal motion in the clumps should be balanced by self-gravity. Using the virial relation from Rohlfs & Wilson (2004) which connects the virial mass with the radius R in pc of an object and the line width $\Delta\upsilon_{1/2}$ in $\mathrm{km\,s^{-1}}$:

$$M = 250 \cdot \Delta\upsilon^2 \cdot R$$

I estimated a range of virial masses for my clumps from $10^4\ \mathrm{M_\odot}$ up to $67 \cdot 10^4\ \mathrm{M_\odot}$, at least one order of magnitude higher than the estimated visible mass. Therefore the clumps cannot be gravitationally bound and in absence of any factor to balance the internal motion they would disperse in a time $t_{disp} = D/\Delta\upsilon_{1/2}$ which for the HI clumps is on average 6Myrs. But the detected HI clumps are not isolated, so self-gravity is not necessary and support in this case can be provided by the surrounding envelope. In this case there must exist pressure equilibrium between the colder HI clumps and the warmer envelope for them to be confined. In addition, as I will explain later in chapter 7, there is a specific range of pressure and volume density where the two phases can co-exist in thermal equilibrium. Comparing the estimated pressure for the HI clumps (Table. 4.5) with the pressures expected for the extended warm envelope according to Table. 3 from Wolfire et al. (2003) and the Bonn model (Kalberla et al., 2007) for the estimated Galactocentric distances R, I find that almost all the clumps, except 117.97+24, 117.51+25.19 an 115.35+22.35 where $\Delta\upsilon_{1/2}$>10 $\mathrm{km\,s^{-1}}$, are overpressured by the surrounding envelope (Chap. 9). This conclusion is supported also by observational evidence, in the study of the two clumps 116.20+23.55 and 115+24.00. As mentioned in the previous two sections, the pressure of the surrounding medium is 71 ± 41 times larger for the former and around 67 times for the latter. Since pressure is given as a product of the volume density by the temperature according to $P/k = <n> \cdot T_{kin}$, the above result can have one of two following consequences. The first possibility is that the detected HI clumps exhibit sufficient small scale-substructure which cannot be resolved by the $9'$ beam of the Effelsberg telescope. This would mean that the constituents of the clump would have small diameters, thus they would be denser and then in equilibrium with the envelope. The second possibility is that while the HI clump detected with the Effelsberg and the GBT beam is a compact and resolved object, it exists in a dynamical state where the force from the external medium will compress it until it will be dense enough to counterbalance the external pressure. Since the detected clumps are not spherical objects but elongated along one axis, this scenario would finally also lead to the fracturing of the clump to smaller denser objects which would also be unresolved with the $9'$ Effelsberg beam.

A first glance to estimate the presence of sub-structure in the clumps was done by comparing the measured brightness temperatures from the Effelsberg telescope T_E with the measured brightness temperature form the LAB HI survey, T_{LAB}, at the same position. For an unresolved, isolated point source, the ratio K of the T_E over the T_{LAB} should be 16. In Table. 4.6, I give the ratio K of the brightness temperatures and the ratio Q of the column densities for each of the detected clumps. According to the Table. 4.6

the ratio K for my clumps ranges between 2.0 up to 10.8 with the mean at 3.32 and an average of 3.92. This implies that the distribution of the ratio is slightly skewed positively towards the lower values. Even taking into account the error of 3%, the ratios are significantly deviating from the expect ratio of 16 for an unresolved point source. While this could imply that the clumps are resolved, one has to be careful to interpret this ratio. The observed clump, in case that it has sub-structure, will be a collection of cold cores in pressure equilibrium with an extended warm medium. Thus the single dish beam observes a mix of cold and warm HI . If the filling factor of the cold gas is sufficiently low then the resulting ratio will be rather small (Chap. 12). Thus the low brightness temperature ratios K found imply a low filling factor of the small scale structure.

Regarding the column density ratio between the Effelsberg telescope over the LAB survey, the values range from 1.13 up to 4.1 with a mean value of 2.28 and an average of 2.22. In comparison with Wakker et al. (2001), who did a similar calculation between the LDS and the Effelsberg telescope, our ratio is higher than the mean ratio of the estimate for low-velocity gas in that paper. My sample also has a wider range of ratios, both in comparison with the HVC/IVC results from that paper.

In relation with the clumps 117.97+24, 117.51+25.19 and 115.35+22.35 with $\Delta\upsilon_{1/2}>$ 10 $\mathrm{km\,s^{-1}}$ the pressures which are 5833 $\mathrm{K \cdot cm^{-3}}$, 1436 $\mathrm{K \cdot cm^{-3}}$ and 730 $\mathrm{K \cdot cm^{-3}}$ respectively, are within the range of values expected by the warm medium at such distances (Kalberla et al., 2007; Wolfire et al., 2003). So it is possible to have pressure equilibrium between the clumps and the surrounding envelopes. No assumption of small scale structure is necessary here to assume stability. In addition, by comparing their volume densities which are 0.597, 0.485, 0.334$\mathrm{cm^{-3}}$, respectively, so the allowed density for the warm medium from Table 3 Wolfire et al. (2003) it is evident that these three clumps are associated with the warm medium.

As already mentioned, Lockman (2002) has detected clumps in the inner Galaxy using the GBT for observations close to terminal velocity. The Effelsberg and the GBT telescopes have similar angular resolutions, so it is reasonable to compare the two samples. In Table 4.7, I compare the median values of the two samples in the first two rows and the range which includes 90% of all the values in the second row. From the Table, it is easy to ascertain a good agreement between the properties of the two samples. The difference in the absolute height $|z|$ between my sample, where the Galactocentric distance is R>8.5 kpc, from the inner Galaxy GBT data for R<8.5kpcc can be attributed to the flaring of the Galactic disk (Kalberla et al., 2007). My mass estimates are slightly higher, also the range is wider but this comes from the fact that the range of diameters probed in my sample is also wider since I detected larger HI clumps. All in all, the similarities in T_L, N_{Hi} , diameter, density and mass show that the two samples constitute the same population of clumps, located at different regions of the Galaxy. The only big difference is in the line width $\Delta\upsilon_{1/2}$. My sample shows more narrow lines than the GBT sample, thus implying smaller kinetic temperatures T_{Kin}. This can be an

	T_E K	T_{LAB} K	$\frac{T_E}{T_{LAB}}$	N_{Eff} $10^{18}\mathrm{cm}^{-2}$	N_{LAB} $10^{18}\mathrm{cm}^{-2}$	$\frac{N_{Eff}}{N_{LAB}}$
113.33+27.00	1.68	0.305	5.5	36	12	2.92
113.16+25.46	2.20	0.860	2.55	32	23	1.39
116.20+23.55	2.89	0.89	3.25	36	22	1.63
116.66+22.80	2.95	0.49	6.02	47	12	3.89
115.35+22.35	1.7	0.60	2.83	35	20	1.72
117.32+24.00	2.0	1.75	2.04	36	32	1.14
115.00+24.00	1.93	0.59	3.27	34	16	2.20
117.97+24.00	1.99	0.98	2.03	74	30	2.43
118.01+24.59	2.22	1.11	2.00	43	32	1.35
117.51+25.19	2.18	0.64	3.40	60	43	1.40
114.50-15.85	3.06	1.04	2.94	45	40	1.13
113.57-12.44	1.97	0.42	4.69	16	5	3.25
112.96-12.44	4.4	1.5	2.93	90	36	2.49
112.96-13.03	4.56	1.76	2.5	65	37	1.77
113.26-14.07	4.97	1.27	3.91	70	29	2.36
113.57-13.48	5.28	1.66	3.18	102	41	2.44
114.32+21.74	1.32	0.33	4.125	21	10	2.12
130.98-19.22	3.63	0.7	5.18	49	18	2.7
130.65-19.51	2.7	0.25	10.8	35	9	4.1
128.84-18.48	5.97	1.01	5.94	107	36	3.01
112.10+27.79	1.59	0.43	3.69	19	10	1.78
113.84+28.7	0.97	0.23	4.12	20	7	2.67
112.45+29.90	1.09	0.20	5.42	9	4	2.09
114.71+29.60	2.62	0.87	3.01	40	27	1.50

Tab. 4.6: *The Effelsberg brightness temperature T_E is the peak values at the given position. The LAB brightness temperature T_{LAB} is the extrapolated value from a nearby position. The column density is calculated over the same range of velocities.*

intrinsic property of the HI clumps outside of the solar circle which may differ from the clumps in the inner Galaxy. For now, assuming that it is more difficult for cold gas to survive at higher z distances, one would expect our sample not to show these narrow lines, and thus this difference could be attributed to selection criteria affecting the two clump samples. But as will be discussed further in Chap. 7 it is possible to have cold HI beyond R>10kpc and thus it is quite reasonable to detect cold HI clumps also in the outskirts of the Galaxy.

	T_L K	FWHM km s^{-1}	N_{Hi} 10^{18} cm^{-2}	|z| kpc	Diameter pc	<n> cm^{-3}	M_{Hi} M$_\odot$
Median							
GBT	1	12.2	20	940	24	0.25	50
This work	1.74	5.2	17.80	2.65	31	0.2	105
90% range							
GBT	0.4 - 2.70	5.4-26.3	7-63	640 - 1210	<19 - 35	0.1-0.9	12-290
This work	0.62-2.66	3-11.6	5.87-59.88	0.96-3.7	9- 58	0.073-0.7	4-766

Tab. 4.7: *I compare the properties of the* HI *clumps for R>8.5kpc, as calculated from the Effelsberg Telescope with the properties of* HI *clumps in the inner Galaxy from GBT detection. The first two row give the median while the second two rows the 90% of the range. The values for the GBT are taken from Lockman (2002).*

5 Synthesis Observations of HI clumps

5.1 Introduction

In Chap. 4, I presented my sample of HI halo clumps detected with the Effelsberg 100-m telescope. The clumps which are composed mostly from colder gas are surrounded by a warmer more extended envelope. The $9'$ beam of the Effelsberg telescope is enough to trace the extended emission but it is not sufficient to detect small scale substructure in the clumps. This small scale morphology is implied by pressure equilibrium considerations and is not excluded by the comparison between the Effelsberg and the LAB spectra. Higher resolution images of the clumps using a synthesis telescope can provide the answers regarding the presence of sub-structure. A general limitation when using interferometers is that they cannot detect structures on angular scales larger than the fringe spacing formed by the shortest baseline. Therefore, in this follow up observations it is impossible to measure the extended emission which surrounds the clumps. The follow-up observations were made for two clumps. Using the ASTRON Westerbork Synthesis Radio Telescope (WSRT), I observed the position of the clump 116.20+23.55. Using the NRAO Very Large Array telescope, I observed clump 115.00+24.00. In this chapter I will discuss the observations done with the two interferometers and present my results.

5.2 W.S.R.T observations

5.2.1 Technical Details

I made follow-up observations with the WSRT of the clump 116.20+23.55 which was one of the first and most typical detections of a HI clump. The WSRT[1] array is composed of fourteen 25-m dishes with an east-west orientation, ten dishes have a fixed mounting while there are also two pairs of movable dishes on rails. The array has a variety of configurations and its baselines extend from 36 m up to 2.7 km. To choose the proper configuration of the array for the observation of the HI clump 116.20+23.55, I took into account its diameter, the $\Delta\upsilon_{1/2}$ of its spectrum and the brightness temperature it exhibits. The exact configuration of the array is seen in Table. 5.8.

I reduced the interferometry data using the software package MIRIAD (Sault et al., 1995) which is able to handle the WSRT data.

---

[1] More information about the Array is found on:http://www.astron.nl/p/WSRT2.htm

Configuration	Maxi-short	Velocity Separation	0.5km s^{-1}
Field of view	$36'$	Time on source	12 h
Synthesized beam	$13''$	Calibration time	2 h
Bandwidth	2.5 MHz	Calibrators	3C286 & 3C48
Channels	1024	T_{sys}	27K
Channel Separ.	2.5 kHz	σ_n	2.25mJy/beam

Tab. 5.8: *The table describes the configuration used to observe at the position 116.20+23.55 with the WSRT. More information about the configurations is found in WSRT quick guide*[3]. *The* σ_n *given is the theoretical estimate for the above parameters.*

5.2.2 Results

The image cube of the follow-up WSRT observation was smoothed with an $60''$ Gaussian beam. The HI halo clump 116.20+23.55 (α=20$^{\rm h}$47$^{\rm m}$22$''$, δ=82$^{\rm d}$56$^{\rm m}$36$''$) as detected with the Effelsberg telescope has a central υ_{lsr} =-68km s^{-1}. At the same position and velocity I searched in the WSRT image cube for HI emission. Fig. 5.34 is an α-δ map of the HI emission as observed with the WSRT telescope at $\upsilon_{lsr} \sim= -68$ km s^{-1}. In this region a number of compact HI objects are detected. The $\upsilon_{lsr} \sim= -68$ km s^{-1} translates to a distance of 7 kpc according to the Bonn model (Kalberla et al., 2007) with an uncertainty of 24%. The deconvolution process was not optimal in the map, so a part of the HI objects present in the map can be attribute to the influence of side-lobes. In the following study only 11 of these objects with S/N more than 5σ_n and an angular radius s$\geq$ $60'$ were considered as real structures and constituents of the HI clump 116.20+23.55. Their observational parameters are given in Table. 5.9.

To estimate their physical properties, given in Table 5.10, I used a similar procedure as for the Effelsberg observations. The cores show very narrow line-widths with an average of $\Delta\upsilon_{1/2}$=3.3$\pm$0.5 km s^{-1}(T_{kin}=240$\pm$40 K). This implies association with the HI clump which in the Effelsberg observations has a $\Delta\upsilon_{1/2}$=3.0$\pm$1 km s^{-1}. The average core angular size is $73''\pm14''$, corresponding to an average spatial size of just 2.5$\pm$0.8 pc (Kalberla et al. (2007) for distance calculation). The angular size of the cores agrees with the hypothesis of Chapt. 4, which associates the stability due to pressure equilibrium with small scale structure of the clumps in the form of cores with arcminute sizes. The average volume density of the cores is found to be $< n >$=2.4$\pm$0.8 cm^{-3}, 30 times larger than the volume density in HI clump 116.20+23.55. The average pressure for the cores is found to be $P = 613 \pm 230$ K$\cdot$cm^{-3} which is approximately 40 times larger than the pressure found for the clump 116.20+23.55 as observed with the 100-m Effelsberg telescope. In comparison the pressure of the envelope from Effelsberg observations is P=1151$\pm$507 K$\cdot$cm^{-3} . So within the errors it is possible to have pressure equilibrium between the cores and the extended envelope. In this case the envelope provides the necessary confinement to stabilize the HI cores. Regarding

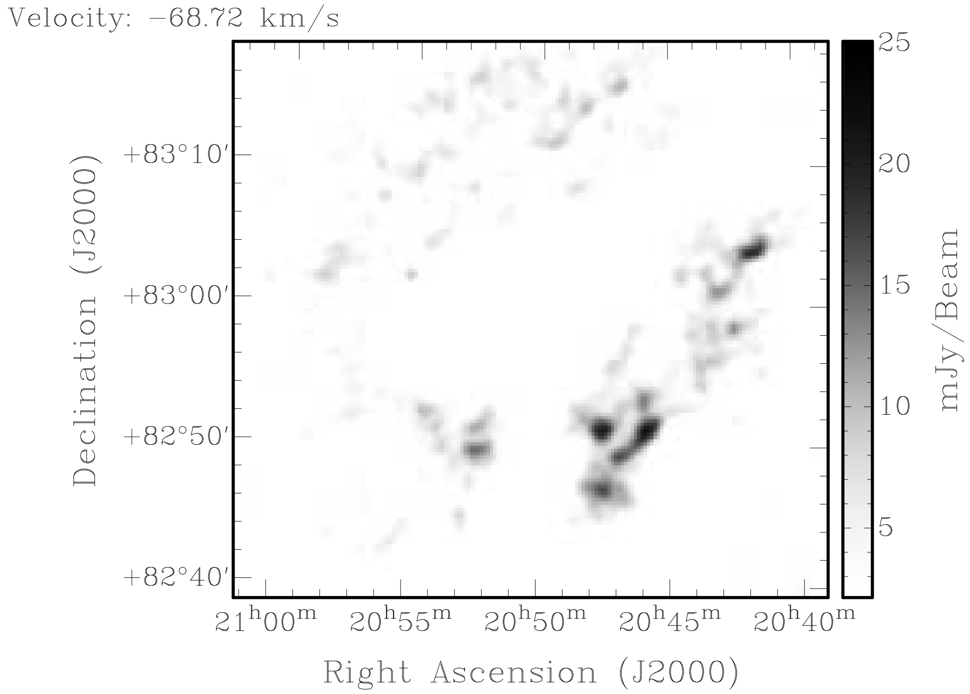

Fig. 5.34: *An RA-DEC map of* HI *emission observed with WSRT telescope centered at* α*=20*^{h}*51*^{m}*00*$''$*,* δ*=83*^{d}*01*^{m}*52*$''$*,* υ_{lsr} *=-68.72km s*$^{-1}$. HI *emission below the 1-*σ_n *of 2.2mJy/beam have been blanked out.*

the thermal stability, a comparison with the range of pressures and volume densities for R=11kpc-15kpc from Table 3 from Wolfire et al. (2003) shows, as will be discuss more thoroughly in Chap. 8, the cores are either undergoing a phase transition towards the cold gas or contain a significant amount of molecular hydrogen which is difficult to trace.

Using my estimates of the volume density and diameter for the cores in Table 5.10 I found an average mass of 3±3 $M_\odot$. The total mass of the 11 cores is ~33 $M_\odot$. For comparison the mass of the HI clump 116.20+23.55 from the Effelsberg observations is 120 $M_\odot$. The 11 cores cover a total area of 15arcmin^2 while the clump in the Effelsberg observation covers an area of 625arcmin^2. Single dish observations trace both the extended warm envelope plus the cold compact phase while the synthesis observation traces only the compact cold component. Therefore from the above I find that the 11 cores cover only 2.4% of the area while they contain at least as much as 30% of the total visible HI mass in this area.

I have also detected in the same WSRT image cube at υ_{lsr} =-84 km s^{-1}, separated kinematically from the previous collection of cores, a few HI objects with size up to a couple of arc-min. The channel map of the HI brightness temperature emission for this region is given in Fig. 5.35. The co-ordinates of the brightest objects are

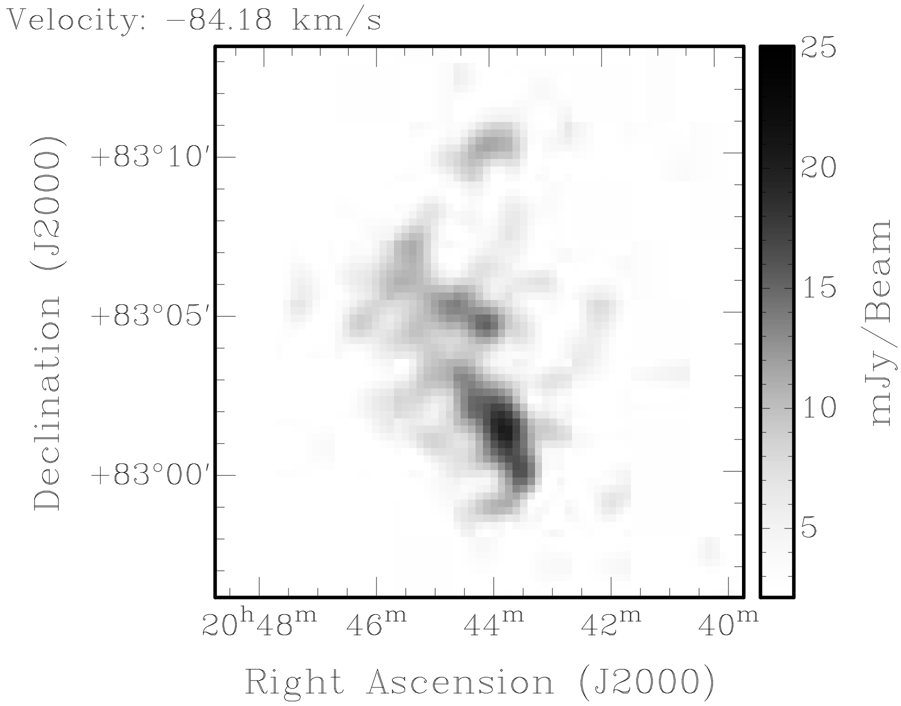

Fig. 5.35: *An RA-DEC map of* HI *emission observed with WSRT telescope centered at* α*=20*^{h}*43*^{m}*48*$'$*,* δ*=83*^{d}*04*^{m}*44*$'$*,* υ_{lsr} *=-84.18km s*$^{-1}$*.* HI *emission below the 1-*σ_n *of 2.2mJy/beam have been blanked out.*

α=20^{h}43^{m}46$'$,δ=83^{d}10^{m}20$'$ at υ_{lsr} =-85.2km s^{-1} and α=20^{h}43^{m}49$'$,δ=83^{d}01^{m}29$'$ at υ_{lsr} =-84.1km s^{-1}. In Fig.5.36, a spectrum from the Effelsberg observation is shown from the location of the WSRT HI objects. As seen there at υ_{lsr} =-68 km s^{-1} the peak emission from the clump 116.33+23.55 is detected. At slightly higher line-of-sight velocity, approximately at υ_{lsr} =-84 km s^{-1}, a second peak is detectable which has a T_B =$\sim$ 0.9 K. This feature shows up at a single pixel in the Effelsberg map. Those objects that represent HI cores have properties similar to the cores of the clump 116.33+23.55 and since they are spatially and kinematically close they must be surrounded by the same warm medium. According to the υ_{lsr} and the Bonn model (Kalberla et al., 2007) they are located further out, at a distance of 9.5 kpc which corresponds to a Galactocentric distance R of 14.6 kpc and a height of 3.8 kpc.

In table. 5.9 and 5.10 their observational and physical properties are given. The HI cores at υ_{lsr} =-84 km s^{-1} have an average angular size s=114$\pm$14$''$, which implies an almost double size from the cores at υ_{lsr} =-68 km s^{-1} since their average diameter is $s = 4.2 \pm 1.1$ pc. The cores are also very cold with a $T_{kin}$$\sim$300 K but they have a smaller volume density of $< n >= 1.4 \pm 0.4$ cm^{-3}. According to Table 3 from Wolfire et al. (2003) the range of pressures for R=15 kpc where thermal equilibrium is possible, is 487-1400 K$\cdot$cm^{-3}. The average pressure of the cores is P=430$\pm$140 K$\cdot$cm^{-3} which agrees within the errors. On the other hand the volume density is somewhat smaller

	α hh:mm:ss	δ dd:mm:ss	υ_{lsr} km s^{-1}	$\Delta\upsilon_{1/2}$ km s^{-1}	s $''$	N_{HI} 10^{18} cm^{-2}
a	20:52:29	82:49:53	-69.8	3.1	74	24(4)
b	20:52:00	82:50:37	-69.8	2.9		12(2)
c	20:47:29	82:47:15	-68.7	3.7	78	24(3)
d	20:47:31	82:51:27	-68.7	2.5	78	16(3)
e	20:45:52	82:51:28	-68.7	3.0	96	19(3)
f	20:43:21	82:51:28	-66.7	3.3	61	15(2)
g	20:43:19	82:57:58	-67.7	3.2	59	15(2)
h	20:41:44	83:04:13	-68.7	3.8	103	32(4)
i	20:42:18	82:58:52	-68.7	3.9	61	14(2)
j	20:43:21	82:54:14	-66.7	3.3	62	15(2)
k	20:43:19	82:57:58	-67.7	3.3	58	15(2)
l	20:43:46	83:10:20	-85.2	3.4	102	19(3)
m	20:43:49	83:01:29	-84.1	4.0	127	28(4)

Tab. 5.9: *Observational parameter of cores observed with WSRT.* υ_{lsr} *is the line-of-sight velocity.* $\Delta\upsilon_{1/2}$ *is the line width of the clump.* s *is the angular size.* N_{HI} *is the* HI *column density.*

	d kpc	R kpc	z kpc	D pc	T_{kin} K	$<n>$ cm^{-3}	P $K\cdot$cm^{-3}	M_{Hi} M$_\odot$
a	7(2)	13	2.5	2.5(0.7)	215(30)	3.1(1.0)	670(240)	4(4)
b	7(2)	13	2.5		190(30)			
c	7(2)	13	2.5	2.6(0.8)	300(40)	2.9(1.0)	880(325)	4(4)
d	7(2)	13	2.5	2.6(0.8)	140(30)	1.9(0.7)	270(115)	3(3)
e	7(2)	13	2.5	3.3(0.9)	200(30)	1.9(0.6)	380(130)	5(4)
f	7(2)	13	2.5	2.1(0.7)	240(40)	2.3(0.8)	560(215)	2(2)
g	7(2)	13	2.5	2.0(0.7)	225(35)	2.4(0.9)	530(215)	1(1)
h	7(2)	13	2.5	3.5(1.0)	330(40)	3.0(0.9)	980(320)	10(9)
i	7(2)	13	2.5	2.0(0.7)	340(40)	2.1(0.8)	710(280)	1(1)
j	7(2)	13	2.5	2.1(0.7)	240(40)	2.3(0.8)	560(215)	2(2)
k	7(2)	13	2.5	1.9(0.6)	245(40)	2.4(0.8)	600(220)	1(1)
l	9.5(2)	15	3.8	4.7(1.3)	250(40)	1.3(0.4)	320(110)	11(10)
m	9.5(2)	15	3.8	5.9(1.6)	350(40)	1.6(0.5)	540(180)	24(21)

Tab. 5.10: *Physical Parameter of cores observed with WSRT array.* d *is distance from the Sun.* R *is the galactocentric radius.* z *is the height above the plane.* D *is the spatial diameter.* T_{kin} *is the kinetic temperature.* $<n>$ *is the volume density.* P *is the pressure in the clump.* M_{Hi} *is the visible* HI *mass.*

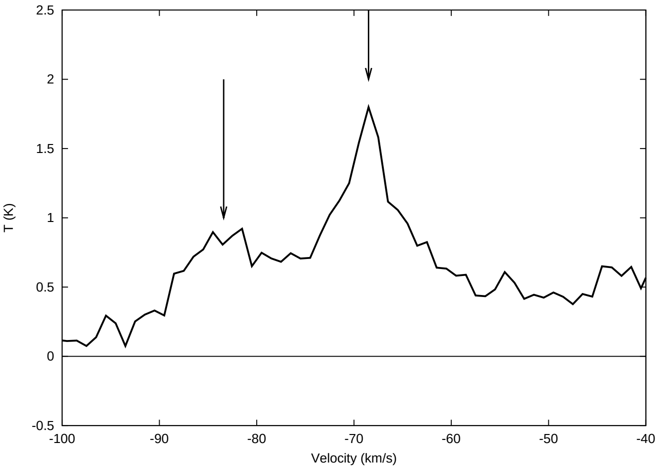

Fig. 5.36: *An average spectrum of the position l=116.3°,b=23.7° from the Effelsberg observations. The arrow at* υ_{lsr} *=-84km* s^{-1} *points to the location of the WSRT object while the arrow at* υ_{lsr} *=-68km* s^{-1} *points to the location of clump 116.33+23.55.*

than the minimum 1.9 cm^{-3} allowed for the cold phase of the gas. So these cores are undergoing phase transition towards the cold phase or hide a significant amount of molecular gas (Chap. 8).

5.3 V.L.A observations

5.3.1 Technical Analysis

I made follow-up observations of the HI clump 115.00+24.00 which is the second typical clump detected with the Effelsberg telescope. I used the Very Large Array (VLA) telescope located in New Mexico. The VLA [4] is a 27-element array. Each antenna has a diameter of 25 m. The antennas are positioned in a Y shape and there are four different possible configurations of the antennas, which gives a size of the array up to 36 km, obtaining the superb resolution of 1.4″at λ =20 cm . To choose the proper configuration to observe the clump 115.00+24.00, I considered the angular size of the clumps , its $\Delta\upsilon_{1/2}$ and the resolution needed. The configuration of the array used for the observation of the clump is given in Table 5.11. More information about the possible VLA configurations can be foun in the telescope stature summary [5].

To reduce the VLA interferometric data I used as software the NRAO Astronomical Image Processing System (AIPS) [6]. I followed the standard data reduction procedure

---

[4] More detailed information about the Array is found on:http://www.vla.nrao.edu/genpub/overview/

[5] http://www.vla.nrao.edu/astro/guides/vlas/current/

[6] http://www.aips.nrao.edu/aips_faq.html

Configuration	DnC	Velocity Separation	0.64km s^{-1}
Largest Ang.Scale	$\sim$15$'$	Time on source	6-h
Synthesized beam	12.5$''$	Primary Calibrator	3C286 & 3C48
Bandwidth	0.78 MHz	Time on Pr. Calibrators	1-h
Channels	256	Phase Calibrator	2344+824
Channel Seper.	3.05 kHz	Time on Ph. Calibrator	40min
Observing Band	21-cm	σ_n	2.25mJy/beam

Tab. 5.11: *The table describes the resources and configuration used to observe at the position 115.00+24.00 with the VLA. The* σ_n *given is the theoretical estimate for the above parameters.*

as described in details in the appendix B of the AIPS cookbook [7].

5.3.2 Results

The image map from the VLA observations was smoothed using a Gaussian beam of 60$''$. The final dimension are 42$'$x 42$'$, is centered at α=20$^{\rm h}$29$^{\rm m}$00fs, δ=82$^{\rm d}$08$^{\rm m}$00$'$ and cover a velocity range from -93 km s^{-1} up to -78 km s^{-1}. A channel map from the image cube at υ_{lsr} =-84.50 km s^{-1} is given in Fig. 5.37.

At υ_{lsr} =-84.5km s^{-1} the Effelsberg telescope detected a HI clump. The VLA observations in the same region have identified 8 HI objects which are associated with the clump 115.00+24.00. The average size of the cores is s=87$\pm$11$''$. The υ_{lsr} $\sim$-85 km s^{-1} corresponds to a distance of 9.5kpc, at Galactocentric radius R=14.5 kpc and height z=4 kpc. Therefore the cores have an average size of D=4.3$\pm$1.1 pc. The average kinetic temperature of this sample of cores is T_{kin}=430$\pm$60 K. This is slightly higher than the T_{kin} found for the sample of the previous section. The sample of these cores is also denser, with an average $<n>= 3.9\pm 1.1$cm^{-3}. As a result, the pressures of the clumps are also higher with an average $P = 1590 \pm 490$K$\cdot$cm^{-3}. While this is higher than the pressure P=535$\pm$23$K\cdot$cm^{-3} estimated for the extended envelope from the Effelsberg data, it agrees with the range of allowed pressures for thermal equilibrium from Table 3 in Wolfire et al. (2003), which for R=15kpc is 487-1400$K\cdot$cm^{-3}. So the cores are in thermal equilibrium with the extended envelope. Regarding the visible mass of the HI cores, their total mass is 107 M$_{\odot}$. The visible HI mass measured with the Effelsberg radio telescope in the case of the clump 115.00+24.00 is 222M$_{\odot}$. So the cores contain 48% of the visible clump HI mass while the remaining 52% should be associated with the extended warmer component which is not detected with the VLA telescope. Still, despite carrying a significant amount of mass the total area covered by the cores is only 3% of the corresponding HI clump area of 484 arcmin^2.

---

[7] http://www.aoc.nrao.edu/aips/cook.html, Appendix B

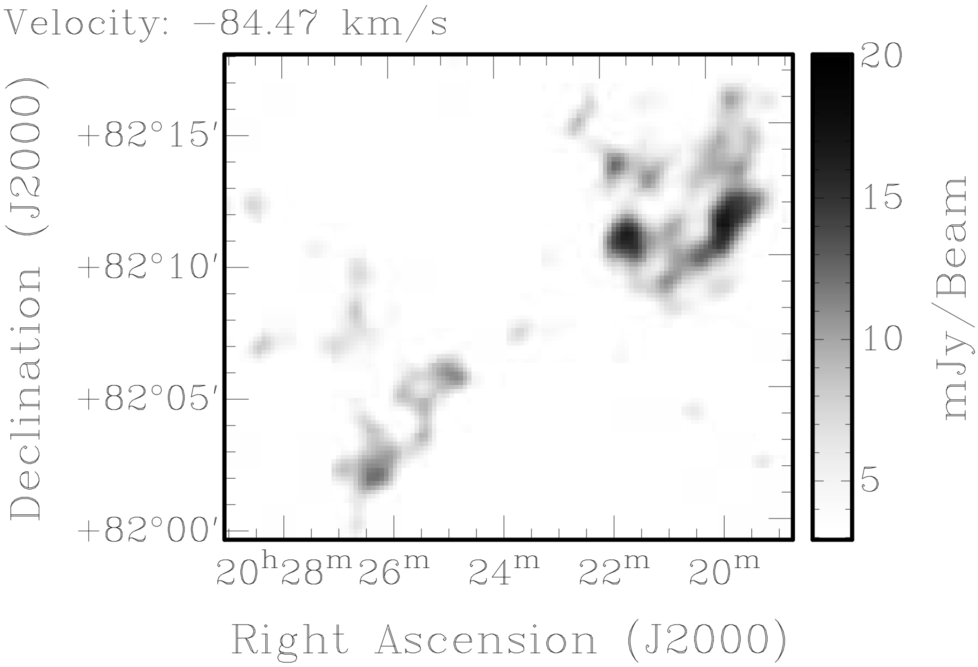

Fig. 5.37: *An RA-DEC map of* HI *emission observed with VLA array centered at* $\alpha=20^{h}29^{m}00'$, $\delta=82^{d}08^{m}00'$, υ_{lsr} *=-84.50km* s^{-1}. HI *emission below the 1-*σ_n *of 3Jy/beam have been blanked out.*

	α hh:mm:ss	δ dd:mm:ss	υ_{lsr} km s^{-1}	$\Delta\upsilon_{1/2}$ km s^{-1}	s $''$	N_{HI} 10^{18} cm^{-2}
a	20:23:58	82:15:13	-87.7	4.3	124	45(6)
b	20:22:24	82:15:49	-87.1	4.7	102	76(9)
c	20:21:36	82:13:46	-84.5	4.3	88	68(8)
d	20:21:34	82:10:35	-85.1	2.8	57	43(6)
e	20:26:38	82:09:48	-85.8	5.8	82	32(4)
f	20:26:11	82:02:27	-83.2	4.0	105	33(4)
g	20:25:56	82:04:57			54	29
h	20:25:07	82:05:25			84	37

Tab. 5.12: *Observational parameter of cores observed with VLA.* υ_{lsr} *is the line-of-sight velocity.* $\Delta\upsilon_{1/2}$ *is the line width.* s *is the angular size.* N_{HI} *is the observed* HI *column density.*

5.4 Summary of Interferometry Results

The WSRT and the VLA high resolution observations confirmed the expected presence of small scale structure in the HI clumps 116.33+23.55 and 115.00+24.00. These

	d kpc	R kpc	z kpc	D pc	T_{kin} K	$< n >$ cm^{-3}	P $\mathrm{K \cdot cm}^{-3}$	M_{Hi} $\mathrm{M}_{\odot}$
a	10.0(3)	15.0	4.0	6(2.0)	410(60)	2.4(0.9)	1010(410)	19(20)
b	10.0(3)	15.0	4.0	5(1.0)	490(70)	5.0(1.1)	2440(570)	32(20)
c	9.5(2)	14.5	3.8	4(1.0)	410(60)	5.7(1.6)	2360(750)	25(20)
d	9.0(2)	14.5	2.5	2(0.7)	170(40)	5.6(2.1)	950(420)	7(4)
e	9.5(2)	14.5	3.8	4(1.0)	730(80)	2.7(0.7)	2000(560)	12(9)
f	9.5(2)	14.5	3.8	5(1.0)	350(60)	2.2(0.5)	780(220)	12(8)

Tab. 5.13: *Physical Parameter of cores observed with the VLA array. d is the distance from the Sun. R is the distance from the Galactic centre. z is the height above the plane. D is the spatial diameter. T_{kin} is the kinetic temperature. $< n >$ is the volume density. P is the pressure. M_{Hi} is the visible* HI *mass.*

HI clumps, when observed with high resolution, are resolved into a collection of cold HI cores, surrounded by an extended warm envelope undetectable in the interferometry observations. Since the cores have a small angular dimension when observed with Effelsberg together with the surrounding extending emission, they appear as an HI clump. Despite their low filling factor the cores carry a significant amount of visible HI mass since they seem to be up to 30 times denser than the HI feature observed with Effelsberg. As a result they are in a pressure equilibrium with the surrounding extended envelope. It is also possible that these two components are in a thermal equilibrium (Chap.7). So the cold cores reside inside the warm medium as stable entities without dispersing or undergoing phase transition.

Stil et al. (2006) have detected a population of HI clump at peculiar velocities using the D configuration of the VLA array. These clumps are located in the inner Galaxy and lie very close to the Galactic plane. Stil et al. (2006) proposed that they are part of the same population of clumps detected by GBT Lockman (2002), widespread throughout different locations in the Galaxy. A comparison between my sample of HI cores and their sample shows that:

- my sample is composed of colder gas since it has lower line widths $\Delta\upsilon_{1/2}$.
- the Stil et al. (2006) sample has ~2 times large size and ~3 times greater volume densities. Since the terminal velocity is used for the distance estimate, the distance uncertainty is small and cannot account for the difference with our sample.
- The visible HI mass in Stil et al. (2006) ranges from $9\mathrm{M}_{\odot}$ up to $2500\mathrm{M}_{\odot}$, compared to 1-$32\mathrm{M}_{\odot}$ in my case.
- The derived volume densities and T_{kin} temperature for the Stil et al. (2006) sample imply also pressures which range from 1800 $\mathrm{K \cdot cm}^{-3}$ up to 10^5 $\mathrm{K \cdot cm}^{-3}$, in most of the cases higher than the pressure of our sample.

These are not necessary contradictory results. Stil et al. (2006) considers data in the inner Galaxy while my sample in the outer galaxy. While a pressure as high a 10^5 K·cm^{-3} in their sample must be attributed to turbulence, according to Table 3 of Wolfire et al. (2003) the smaller the Galactocentric distance R is, the higher the pressure and the volume density of the cold gas are expected to be. Therefore cores which are located in the inner Galaxy, as in the case of Stil et al. (2006) are expected to be denser than the cores in the outer part of the Galaxy, as our cores are.

6 Arecibo Observations

6.1 Introduction

Although the 100-m Effelsberg telescope can provide maps with good resolution and sensitivity to detect HI clumps, the mapping process is slow and high resolution is needed to confine the physical parameter of the HI clumps. An interferometer is appropriate only for follow up observations of specific clumps since it is not sensitive to extended emission. The only other single dish telescope which has increased resolution, sensitivity and mapping speed is the 305-m Arecibo radio-telescope. So I used it to map a region of the sky to search for clumps taking into account the limited declination range. I will discuss here the technical details of the observation and present the results.

6.2 Technical details

I used the 305-m Arecibo telescope to observe a field selected from the fourth Galactic quadrant at 21-cm. The position was selected with the help of map 2.5. I took into account the restriction of the Arecibo telescope to observe within a declination range of -1°20′ up to 38°02′. Since all of the fields observed with Effelsberg are located at the first and second quadrant, I decided to select a field from the fourth quadrant to probe a different location of the sky. The field is centered at α= 08 $^{\mathrm{h}}$05 $^{\mathrm{m}}$00″, δ= 02 $^{\mathrm{d}}$45 $^{\mathrm{m}}$00″ (l=219°, b=17.58°). The dimension of the map is $\Delta\ \alpha$=1$^{\mathrm{h}}$10$^{\mathrm{m}}$ and $\Delta\delta$=5$^{\mathrm{d}}$30$^{\mathrm{m}}$.

I mapped this region with the Arecibo L-band Feed Array (ALFA)[8] which is a multi-beam receiver with the capability to survey areas of the sky rapidly. As a backend I used the spectrometer GALFA[9] which is an instrument dedicated for Galactic surveys. It has a bandwidth of 7 MHz with a total number of 8192 channels. At 21-cm this gives a high spectral resolution of 0.18$\mathrm{km\,s^{-1}}$. I applied a smoothing to the velocity axis so the final spectral resolution of the maps is 0.72$\mathrm{km\,s^{-1}}$.

I have conducted the observations in a typical GALFA manner. I used the basket weaving observing mode (Stanimirović et al., 2006). In this modes the telescope observes at the meridian, moving only in zenith angle at a given rate, thus covering a zig-zag pattern of the sky as the earth moves. On consecutive days, shifted scans are obtained so the whole region of interest in slowly covered. In Fig. 6.38, an example of two basket-weave scans is shown. The resulting map has almost full-Nyquist sampling, independent of the sampling rate. The most faint HI clump detected with Effelsberg has a $T_L = 0.62$ K. The expected T_A for Arecibo would be more than 4 K. So I used the

---

[8] A description can be found in http://www.naic.edu/alfa/

[9] A detailed documentation is found in http://www.naic.edu/alfa/galfa/docs/galspect/

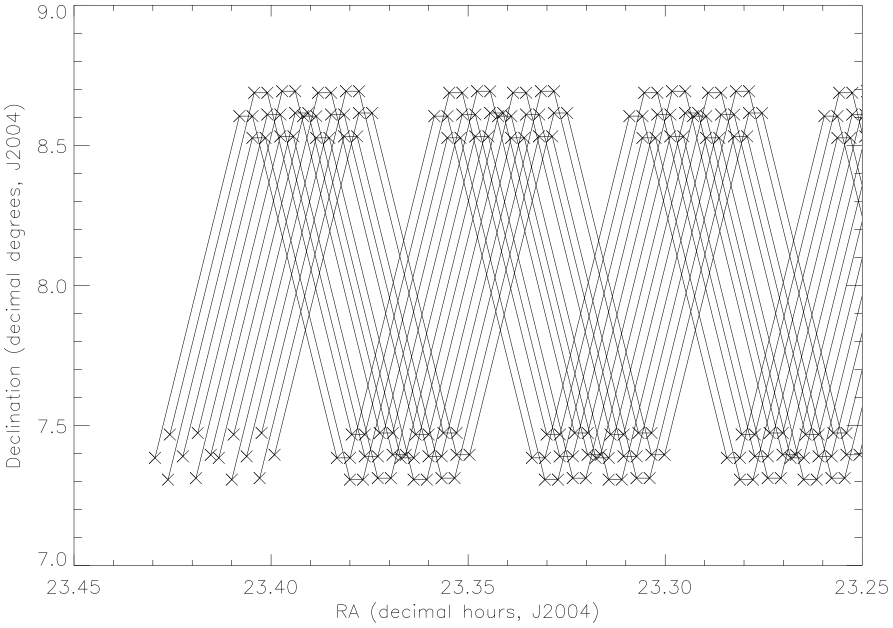

Fig. 6.38: *An example of basket weave scans(Courtesy of Snezana Stanimirovic)*

fast “gear”, that is the fastest speed for the mapping, which gives an integration time 2.4 sec per pixel. This results in a $\sigma_n \sim 0.6$ K noise level for my map, enough to detect the clumps.

The baseline calibration was done using the Smart Frequency Switching method (Heiles, 2007) specially developed for the GALFA projects. For the data reduction I used a pipeline of IDL programs developed by C. Heiles and J. Peek especially for the reduction of GALFA HI data[10]. The final result is a HI data cube with an angular resolution of $3.83'$ and a velocity resolution of $0.72 \mathrm{km\,s^{-1}}$.

6.3 Extended emission in Arecibo and Stray Radiation correction

Using a radio telescope with a total solid beam angle Ω_A, we measure the antenna temperature T_A, a convolution between antenna pattern P and the true brightness distribution of the sky T given by (Bracewell, 1956)

$$T_A = \int P(x-x') \cdot T(x',y') dx'dy' \tag{6.10}$$

---

[10] More information in http://www2.naic.edu/alfa/galfa/docs/pipe_doc_aug06.pdf and Stanimirović et al. (2006)

This equation includes radiation received from the main beam with a solid angle Ω_{mb} and from the side-lobes with a solid angle $\Omega_s = \Omega_A - \Omega_{mb}$. In case of a strong source with an angular dimension of the order of the main beam size, the contribution in the T_A from the side-lobes is not important. In the 100-m Effelsberg telescope the main beam efficiency η_{mb} is more than 70% while in the Arecibo 300-m the average main beam efficiency for the 7-pixel ALFA receiver system is $\sim$ 60%, so the radiation received from the far side-lobes contributes very little to the T_A, we can therefore safely consider that $T_B = T_A/\eta_{mb}$. The radiation received in the first side-lobes may have the effect of slightly deforming the source.

On the other hand the measurement of the true brightness temperature T_B distribution of an extended source in the sky is far more complicated. As pointed out in Kalberla et al. (1980) up to 50% of the observed profile area at high latitude can be attributed to time variable radiation received from the far side lobes. So a correction procedure is needed where we separate the radiation received in the main beam from the radiation received from the residual antenna pattern. The correction applied to the 100-m Effelsberg data is described in Kalberla et al. (1980).

As described in Heiles et al. (2001), the Arecibo reflector is fixed with respect to the ground while the feed moves with respect to the reflector. Thus, as the source is tracked, the antenna pattern characteristics of the telescope can change in a complicated way. It is extremely difficult to apply a stray radiation correction in a similar fashion as for the 100-m Effelsberg telescope. As already mentioned in the previous paragraph, a source with a small angular size and in particular a HI clump is unaffected by stray radiation. In the case of the extended emission, since the correction is not possible, I need to find a way to estimate the effect of stray radiation in the data. Data from the Effelsberg 100-m Radio telescope were not available for the same position as the region observed with Arecibo. Instead the LAB survey (Kalberla et al., 2005b) was used to evaluate the effect of stray radiation in the Arecibo maps. LAB is corrected for stray radiation with the residual errors in the profile wings due to defects in the stray radiation correction below 40 mK. First of all I smoothed the Arecibo maps to the $36'$ resolution of the LAB survey. This is done using the task “Smooth” in the MIRIAD software package, by convolving the maps with a beam of Gaussian shape. Then random positions of the maps were selected and the spectra were compared between the Arecibo and the LAB survey, searching for inconsistencies between the spectra in the wings of the main Galactic line.

From Fig. 6.39a-f the comparisons of the spectra for five random positions are shown. Fig. 6.39b is at a position close to the edge of the map. It is the only position where the spectrum taken from Arecibo varies significantly from the spectrum of the LAB survey, especially on the positive velocity wing. This is most probably an artifact of the smoothing process, where there are masked pixels in the area of the Gaussian convolution. The other spectra are nearly identical, showing only a slight differences. Part of it can be attributed to the difference of the data reduction process, like calibration,

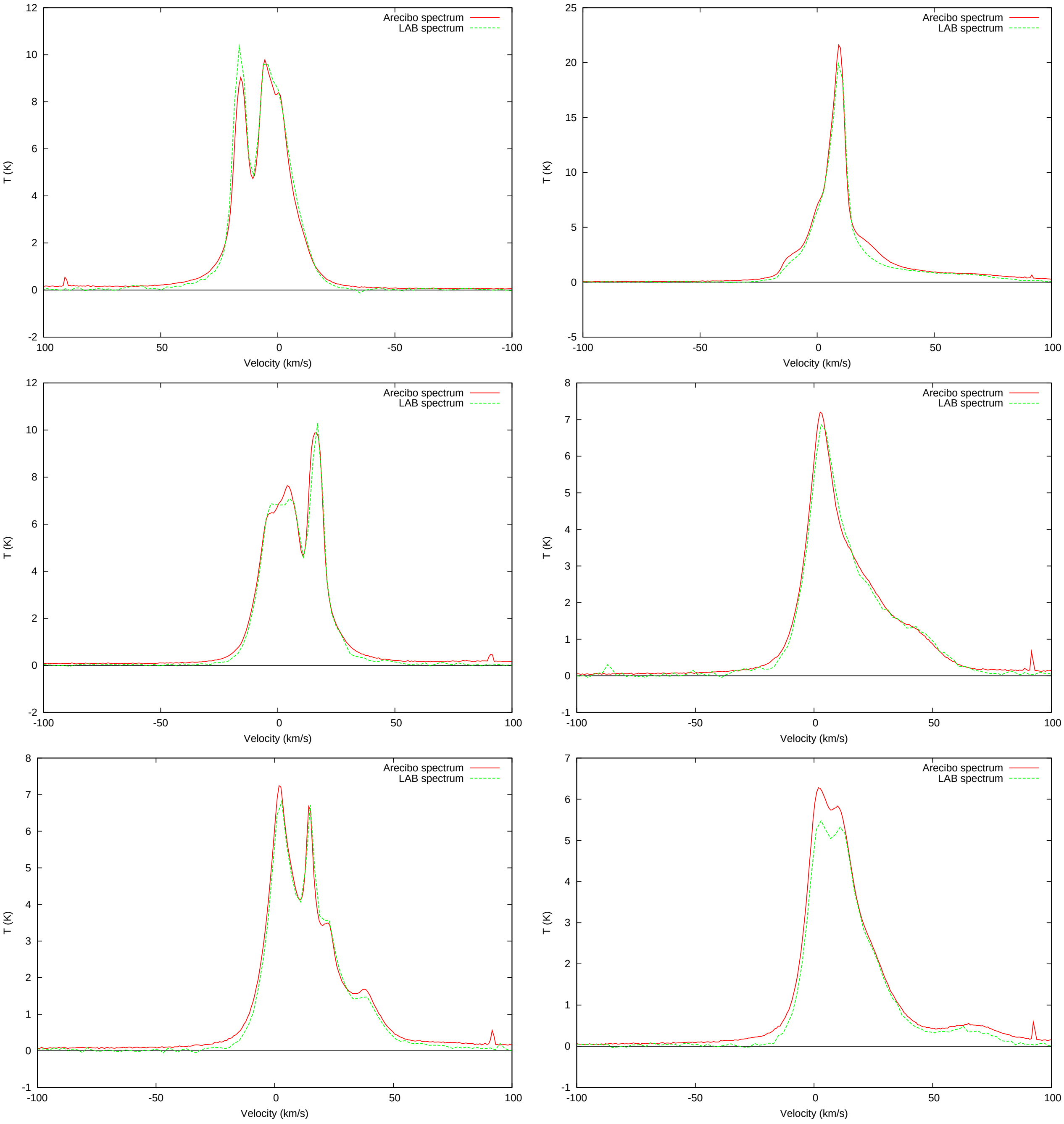

Fig. 6.39: *A comparison between spectra from the LAB survey and those observed with the Arecibo telescope. The Arecibo data have been smoothed to the resolution of the LAB survey of* $36'$*. a) Top Left: Position l=222.5°, b=22° b) Top Right: Position l=219°, b=13.5° c) Middle Left:Position l=222°, b=22° d) Middle Right: Position l=219°, b=20° e) Bottom Left: Position l=219.5°, b=18.5° f) Bottom Right: Position l=216.5°, b=17°*

baseline correction etc., between the LAB survey and the Arecibo data. Part of it, is caused by the scaling of the Arecibo data to the LAB survey resolution and finally stray radiation also increases the T_A in the Arecibo data.

Generally, I concluded that, while there is some stray radiation contamination in the Arecibo data, it does not affect my data significantly. Since the velocity morphology of the velocity wing is identical, the extended structures detected in the Arecibo data are real and not caused by stray radiation. The only minor effect the stray radiation may have, is to increase the estimated columd density in the Arecibo data. Since the two spectra show only small systematical differences, the uncertainty is not expected to be significant.

6.4 Results

The HI emission map observed with the Arecibo 300-m telescope covers a region of $17.5^\circ \times 5^\circ$ with an angular resolution of $3.8'$. The central position is l=219.5° and b=17.23° and the υ_{lsr} range covered is from 100 $\mathrm{km\,s^{-1}}$ up to -100 $\mathrm{km\,s^{-1}}$. No major HVC complex is associated with this region. While no correction for stray radiation was applied to the maps, as discussed in section 6.3, it does not affect the spectral profiles.

HI emission associated with the Galaxy should have positive υ_{lsr}, according to the Bonn Mass model Kalberla et al. (2007). Above υ_{lsr} =89 $\mathrm{km\,s^{-1}}$ there is no HI emission and below $\sim$ 30 $\mathrm{km\,s^{-1}}$ HI emission is starting to be associated more closely with the disk. In this range of υ_{lsr}, a peak temperature map of HI emission is made, shown in Fig. 6.40. It is created by calculating the peak temperature for each position. While it can be misleading regarding the actual size of the clumps since there is confusion between objects located in adjacent positions which are kinematically separated, it gives a good overall view of the structure of the HI emission. In Fig. 6.40 within this velocity range exists a very faint extended component. It was already shown in subsection 6.3 that this component is real and not an artifact due to stray radiation. The peak temperature T_P of the extended component is up to 3 K. The column density between υ_{lsr} =60 $\mathrm{km\,s^{-1}}$ and 30 $\mathrm{km\,s^{-1}}$ can reach up to $100 \pm 6 \cdot 10^{18}$ $\mathrm{cm^{-2}}$. This extended component is similar to the envelope surrounding the HI clumps detected with the 100-m Effelsberg telescope.

There are a number of positions with high peak temperatures T_P and narrow line widths $\Delta\upsilon_{1/2}$, similar to the regions observed with the Effelsberg telescope which can be associated with HI clumps surrounded by the extended envelope. The observational properties of these clumps are seen in Table. 6.14. The clumps show narrow line widths similar to the Effelsberg sample with an average $\Delta\upsilon_{1/2}\sim$4.9±0.7 $\mathrm{km\,s^{-1}}$, implying a $T_{kin}\sim$530±75 K. 75% have υ_{lsr} smaller than 50 $\mathrm{km\,s^{-1}}$. According to the Bonn mass model (Kalberla et al., 2007) their mean distance is d=4±0.6 kpc while

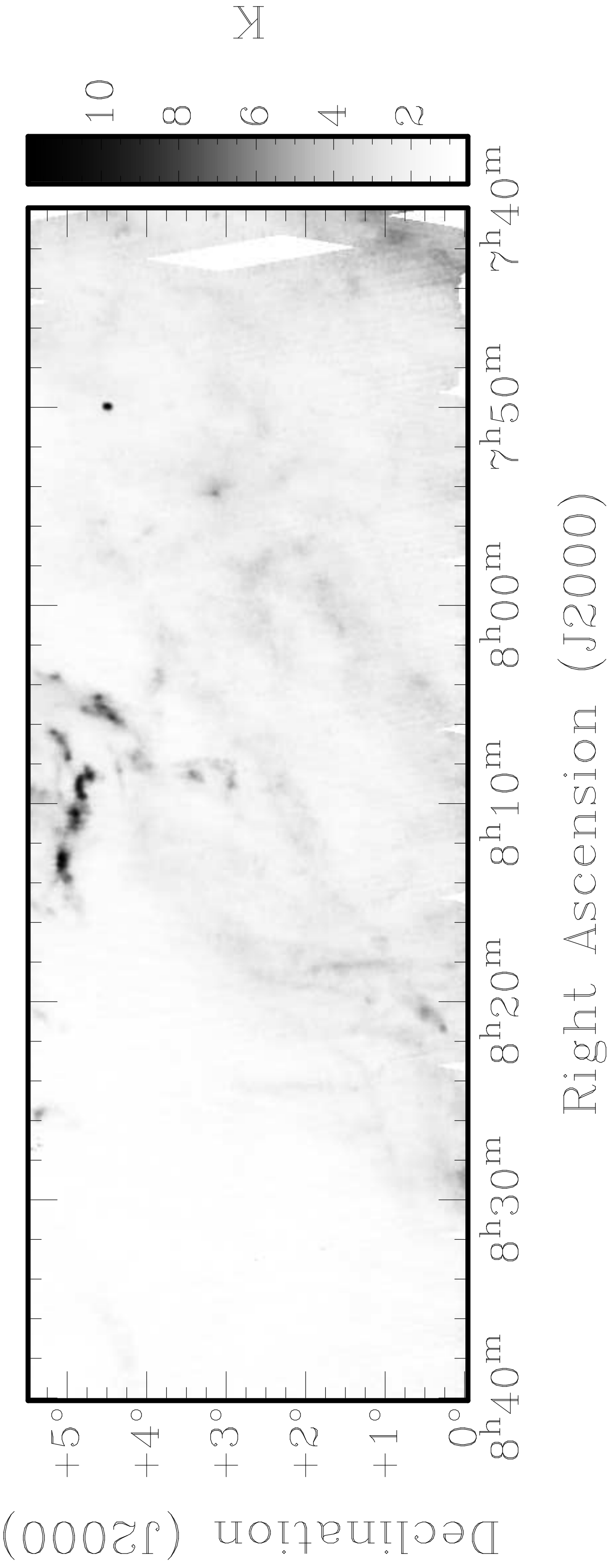

Fig. 6.40: *A peak temperature map of* HI *emission at a position centered at* $\alpha = 08^{\mathrm{h}}05^{\mathrm{m}}00''$, $\delta = 02^{\mathrm{d}}45^{\mathrm{m}}00''$. *The range of* υ_{lsr} *is from 29.8* $\mathrm{km\,s^{-1}}$ *up to 88.7* $\mathrm{km\,s^{-1}}$. HI *emission with peak temperature lower than 0.6K has been excluded. Blank positions have not been observed.*

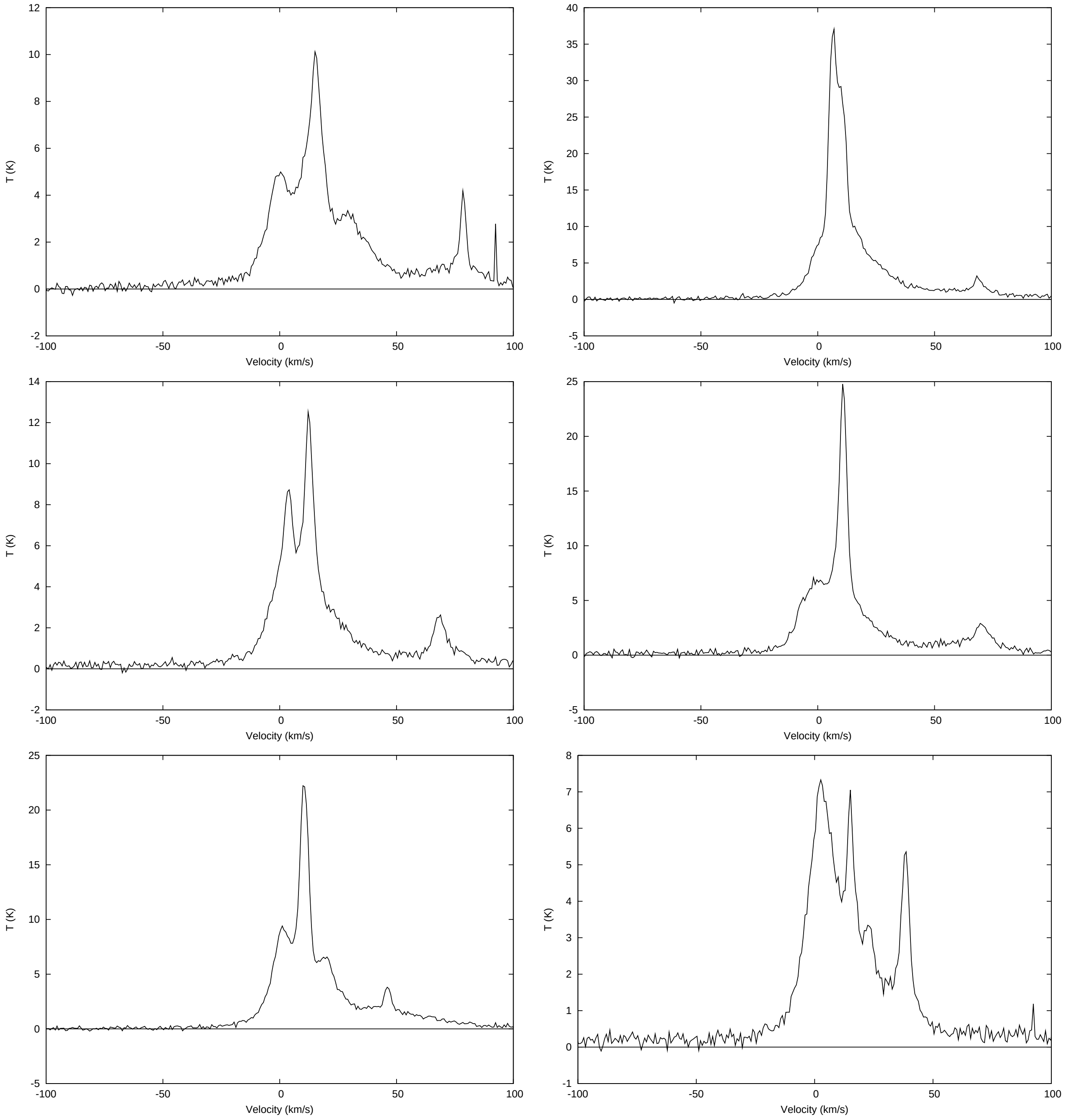

Fig. 6.41: *Spectra of the clumps detected with the Arecibo telescope. A spectrum of the clump a:) Top Left: An average spectrum of 217.5+15.16 at* υ_{lsr} *=78km* s^{-1}*. b) Top Right: 217.5+11.96,*υ_{lsr} *=68.1km* s^{-1} *c) Middle Left: 220.28+15.16,* υ_{lsr} *=68.9km* s^{-1} *d) Middle Right: 218.38+13.10,* υ_{lsr} *=69.6km* s^{-1}*e) Bottom Left:215.72+12.29,* υ_{lsr} *=46.0km* s^{-1} *f) Bottom Right: 219.39+18.53,* υ_{lsr} *=38.6km* s^{-1}*.*

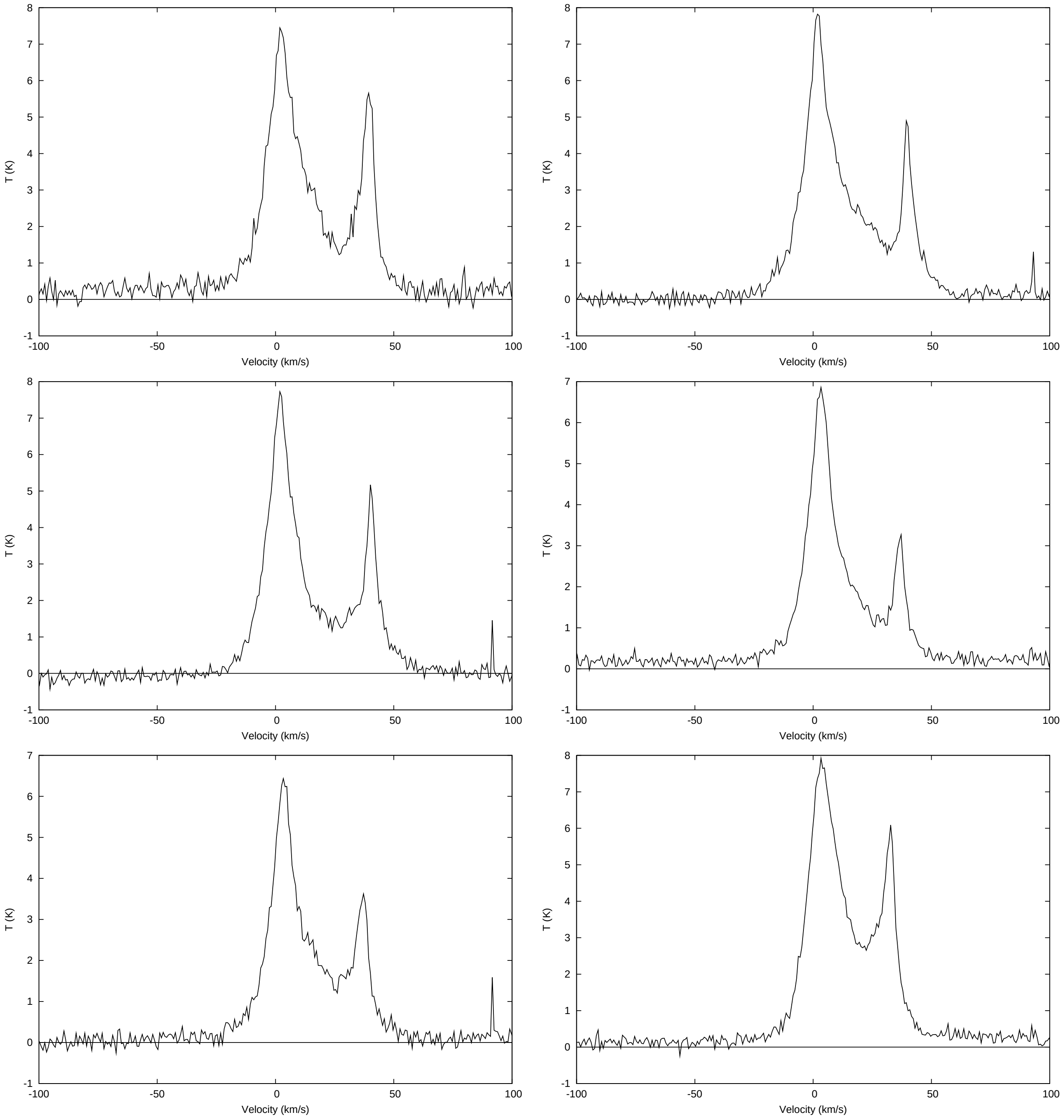

Fig. 6.42: *Spectra of the clumps detected with the Arecibo telescope. a) Top Left: 218.85+18.77,* υ_{lsr} *=39.4* $\mathrm{km\,s^{-1}}$ *b) Top Right : 217.90+19.06,* υ_{lsr} *=39.4* $\mathrm{km\,s^{-1}}$ *c) Middle Left: 217.99+18.83,* υ_{lsr} *=40.1* $\mathrm{km\,s^{-1}}$ *d) Middle Right: 218.48+22.24,* υ_{lsr} *=36.4* $\mathrm{km\,s^{-1}}$ *e) Bottom Left: 217.83+21.03,* υ_{lsr} *=37.2* $\mathrm{km\,s^{-1}}$ *f)Bottom Right:216.57+18.46,* υ_{lsr} *=32.8* $\mathrm{km\,s^{-1}}$*.*

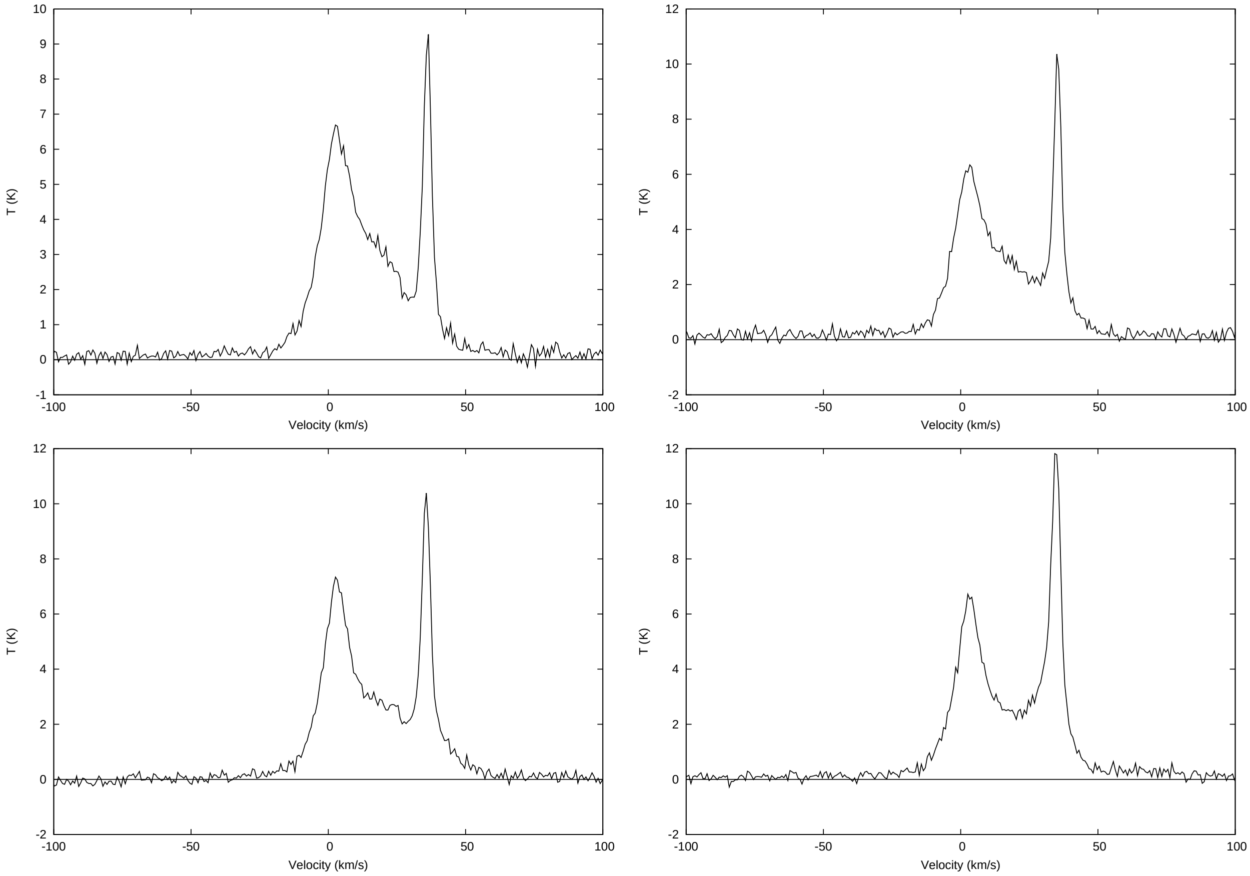

Fig. 6.43: *Spectra of the clumps detected with the Arecibo telescope. a) Top Left: 217.56+19.29,* υ_{lsr} *=35.7* $\mathrm{km\,s^{-1}}$ *b) Top Right: 217.50+19.46,* υ_{lsr} *=35.0* $\mathrm{km\,s^{-1}}$ *c) Bottom Left: 217.60+19.76,* υ_{lsr} *=35.7* $\mathrm{km\,s^{-1}}$ *d) Bottom Right: 217.74+20.38,* υ_{lsr} *=35.7* $\mathrm{km\,s^{-1}}$

their average distance is 5.6±0.8 kpc. For comparison, the Effelsberg sample has a mean distance of 7.5 kpc and an average distance of 6.6 kpc. The angular dimension of the HI clumps has a mean of $6'$, implying a mean diameter of 8.5 pc. In comparison the Effelsberg HI clumps have a mean diameter of 28 pc and the cores a mean diameter of 2.5 pc.

In Fig. 6.41, 6.42, 6.43 the spectrum for each clumplet is shown. Table. 6.15 has the estimates of the physical properties of the HI clumps. As seen, the clumps are dense, denser than the Effelsberg clumps and exhibit high pressures. If we take into account the angular and spatial dimensions of the clumps, it can be easily ascertain that the Arecibo sample shows more similarities with the HI cores detected with the synthesis Array than with the sample of HI clump detected with the Effelsberg telescope. A comparison with Table 3 from Wolfire et al. (2003) shows that, all the clumps except clump 215.72+12.29 have pressures and volumes densities within the allowed phase space for the cold neutral phase, so it is possible that they co-exists with the extended

	α hh:mm:ss	δ dd:mm:ss	υ_{lsr} km s^{-1}	T_L K	$\Delta\upsilon_{1/2}$ km s^{-1}	s $'$	N_{HI} 10^{18} cm^{-2}
217.50+15.16	07:53:43	02:55:00	78	4.2	3.2	6	50(8)
217.51+11.96	07:42:24	01:26:00	68	3.2	<5	5	63(6)
220.28+15.16	07:58:40	00:32:00	69	2.6	6.8	6	68(6)
218.38+13.10	07:47:56	01:12:00	70	2.8	$\sim$10	7	76(5)
215.72+12.29	07:40:16	03:08:00	46	1.8	3.5	5	25(4)
219.39+18.53	08:09:00	02:57:00	39	4.4	4.2	5	50(6)
218.85+18.77	08:08:52	03:26:00	39	5.6	6.7	9	75(6)
217.90+19.07	08:08:16	04:22:00	39	3.2	3.4	6	42(6)
217.99+18.83	08:07:36	04:11:00	40	3.5	3.9	7	42(6)
218.48+22.24	08:20:36	05:20:00	36	2.3	6.3	7	30(3)
217.93+21.03	08:15:20	05:14:00	37	2.3	5.9	4	36(5)
216.57+18.40	08:03:36	05:11:00	33	3.7	4.4	4	51(6)
217.56+19.29	08:08:28	04:45:00	36	7.2	3.5	4	75(11)
217.50+19.46	08:09:00	04:53:00	35	8.8	3.5	7	81(12)
217.60+19.76	08:10:14	04:56:00	36	8.9	3.5	6	88(13)
217.74+20.38	08:12:40	05:06:00	36	9.0	5.0	11	118(12)

Tab. 6.14: *Observational quantities of the* HI *clumps detected with the NAIC Arecibo 300-m telescope. Columns a & b are the equatorial coordinates of the clumps. Column C is the line of sight velocity* υ_{lsr} *. Column D is the peak temperature* T_L*. Column E is the line width* $\Delta\upsilon_{1/2}$*. Column F is the angular diameter of the clump* s*. Column J is the column density. The uncertainty is given in the parenthensis.*

envelope in thermal equilibrium (More Chap.8).

In the Table. 6.16, I compared the peak temperature of the clumps between the Arecibo and the LAB spectra. The ratio K of the peak temperatures ranges between 2.27 up to 6.57, with a mean of 3.37. According to Appen.12 this does not exclude the presence of small scale structure in the Arecibo clumps but unlike the Effelsberg clumps, this is not necessary from the perspective of the stability of the clumps. If we assume that the Arecibo clumps break into cores of an arcmin in size, similar to the Effelsberg clumps, the small scale structure should be very limited to a a few cores for each clump. This is different from the Effelsberg case where at least 10 cores were observed by synthesis observations. In the case of the column densities the ratio between the Arecibo and the LAB column densities ranges between 1.92 and 5.12. Since the Arecibo observation trace clumps which are undetectable with the LAB , the high ratios show that the clumps carry a significant amount of visible HI mass at that position.

Table. 6.17 gives the mean value and the range of the measured properties of the clumps and compares them with the values for the LVC from Stanimirović et al. (2006). The clumps in this paper are located close to the anti-center region and since

	d kpc	R kpc	z kpc	D pc	T_{kin} K	$< n >$ cm^{-3}	P $K \cdot$ cm^{-3}	M_{Hi} M$_{\odot}$
217.50+15.16	13.5(2.5)	20	3.5	22(5)	220(50)	0.7(0.2)	160(60)	160(85)
217.51+11.96	10.0(1.5)	17	2.0	13(3)	<550(80)	1.5(0.4)	<825(250)	72(37)
220.28+15.16	9.5(1.0)	17	2.5	17(3)	1000(100)	1.3(0.3)	1320(330)	121(49)
218.38+13.10	10.0(1.5)	17	2.2	20(4)	2200(150)	1.3(0.3)	2820(680)	178(75)
215.72+12.29	5.5(0.5)	13	1.1	8(2)	270(50)	1.0(0.3)	280(80)	9(4)
219.39+18.53	4.0(0.5)	12	1.2	6(1)	390(70)	2.7(0.7)	1040(300)	12(6)
218.85+18.77	4.0(0.5)	12	1.2	10(2)	990(100)	2.4(0.4)	2370(550)	48(17)
217.90+19.07	4.5(0.5)	12	1.5	8(2)	250(50)	1.6(0.4)	420(130)	19(8)
217.99+18.83	4.5(0.5)	12	1.4	10(2)	340(60)	1.4(0.3)	480(130)	25(10)
218.48+22.24	4.0(0.5)	12	1.5	9(2)	870(150)	1.1(0.2)	980(320)	14(5)
217.93+21.03	4.0(0.5)	12	1.4	5(1)	760(80)	2.2(0.7)	1680(420)	6(3)
216.57+18.40	3.5(0.5)	11	1.1	4(1)	440(70)	3.7(1.2)	1600(500)	7(4)
217.56+19.29	4.0(0.5)	12	1.2	4(1)	260(50)	5.6(1.8)	1480(510)	9(5)
217.50+19.46	4.0(0.5)	12	1.2	7(1)	270(50)	3.5(0.8)	950(260)	29(12)
217.60+19.76	4.0(0.5)	12	1.2	7(1)	270(50)	4.1(1.0)	1085(290)	28(12)
217.74+20.38	4.0(0.5)	12	1.3	12(2)	540(80)	3.1(0.6)	1680(400)	112(36)

Tab. 6.15: *Derived quantities of the* HI *clumps detected with the Arecibo NAIC 300-m telescope. Column A gives the distance d. Column B gives the Galactocentric radius R. Column C gives the height z. Column D gives the spatial diameter of the clump D. Column E gives the T_{kin}. Column F gives the volume density $< n >$. Column G gives the pressure P. Column H gives the visible* HI *mass*

the $dv/dR \sim 0$, it is not possible to determine their distance using the line-of-sight velocity. The authors had to utilize thermal equilibrium arguments (described in 8) to get an estimate of the distance. Therefore I do not compare physical properties depending on the distance and I compare only the properties measured directly from the observations. The comparison of the two samples shows the clump of this work have a wider range of properties. And in the region observed by me, I probe denser and heavier HI clumplets. Still the $\Delta\upsilon_{1/2}$ and the similar angular size shows that it is possibly the same population of clumps since it is part of the same gas phase.

6.5 Clump at α=07$^{\rm h}$049$^{\rm m}$46.60$''$, δ=04$^{\rm d}$32$^{\rm m}$32.006$''$

Up to now all the detected HI clumps do not show any velocity gradient, implying no rotation or any other internal motions. In the Arecibo map I have identified a spherical HI object, which if an HI clump, is the first one to show evidence for intrinsic motion.

Fig. 6.45 is a RA-DEC position map of the HI emission centered at α= 07$^{\rm h}$49$^{\rm m}$46.60$''$, δ=04$^{\rm d}$32$^{\rm m}$32.006$''$, υ_{lsr} =47.5 km s^{-1}(l=215.54°, b=15.04°). In the center of the map a

	T_{Arec} K	T_{LAB} K	$\frac{T_{Arec}}{T_{LAB}}$	N_{Arec} 10^{18} cm^{-2}	N_{LAB} 10^{18} cm^{-2}	$\frac{N_{Arec}}{N_{LAB}}$
217.50+15.16	4.21	0.64	6.57	49.83	9.71	5.12
217.51+11.96	3.23	0.79	4.08	62.54	12.55	4.98
220.28+15.16	2.62	0.46	5.69	67.65	19.99	3.38
218.39+13.10	2.85	0.98	2.90	76.12	27.72	2.74
215.72+12.29	3.80	1.61	2.35	65.05	18.24	3.56
219.39+18.53	5.35	1.47	3.63	80.31	21.06	3.81
218.85+18.77	5.65	1.49	3.77	115.86	42.81	2.71
217.90+19.07	4.90	1.89	2.59	92.10	47.79	1.92
217.99+18.83	5.16	1.48	3.46	114.67	52.98	2.16
218.48+22.24	3.11	0.57	5.45	57.37	13.05	4.39
217.93+21.03	3.62	1.59	2.27	90.68	25.16	3.60
216.57+18.46	6.09	2.17	2.80	148.26	62.93	2.35
217.56+19.29	8.67	2.78	3.11	100.03	40.41	2.47
217.50+19.46	10.36	3.15	3.28	110.65	44.38	2.49
217.60+19.76	10.38	3.32	3.12	117.21	44.48	2.46
217.74+20.38	10.54	2.81	3.75	146.87	41.21	3.56

Tab. 6.16: *The Arecibo temperature is the peak temperature at the position of the clump.The LAB temperature is the brightness temperatire T_B as interpolated from a nearby positions. The column density is calculated over the same range of velocities.*

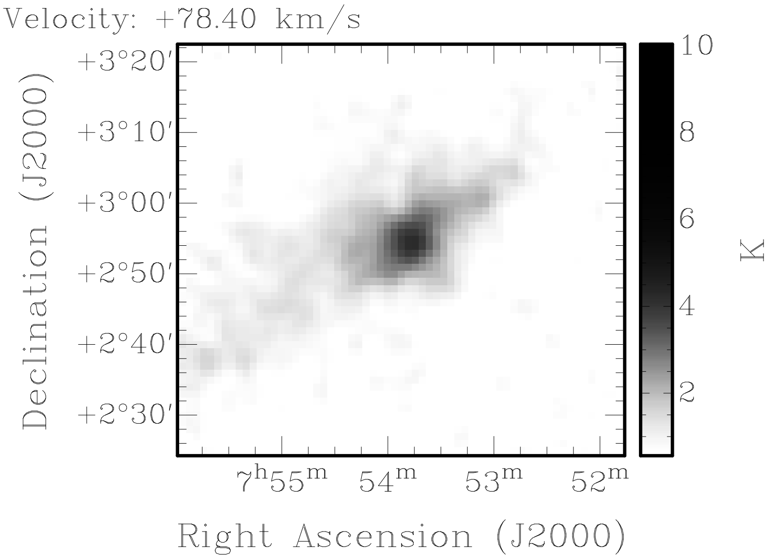

Fig. 6.44: *A map of* HI *emission observed with the Arecibo telescope showing the clump 217.5+15.16. Emission below 1-σ level of 0.6K is cut off.*

	T_L K	$\Delta\upsilon_{1/2}$ km s^{-1}	N_{Hi} 10^{18} cm^{-2}	Angular Size $'$
Median				
Stanimirović et al. (2006)	-	4.00	20	-
This work	3.6	4.71	56.84	6.255
Range				
Stanimirović et al. (2006)	1.6 - 4.1	3-7.6	10-30	6-12
This work	1.82-9.04	3.2-10	24.77-117.51	4-11.28

Tab. 6.17: *I compare the properties of the* HI *clumps for R>8.5kpc, with the* HI *clumps at the anti-center from Stanimirović et al. (2006). Both observation were done using the Arecibo 300-m telescope. The first two row give the median while the second of the two the range.*

nearly spherical HI object is detected. The spectrum at the peak is given in Fig. 6.46. The $\Delta\upsilon_{1/2}$ at the peak is $\Delta\upsilon_{1/2}$=2.7±0.7 km s^{-1}, which implies a kinetic temperature of T_{kin}=160±40 K, while averaging over the clump gives a line width $\Delta\upsilon_{1/2}$=3.4km s^{-1}, implying T_{kin}=250±50 K. When moving in radius from the center of the object towards the edge the line width $\Delta\upsilon_{1/2}$ increases slightly.

The temperature at the peak is equal to T=11.5K. I have calculated a zero moment map to estimate the column density of the clump and the radius. The column density map is seen in Fig. 6.48. The peak column density as extracted from the map is $N_{peak} = 63 \pm 12 \cdot 10^{18}$ cm^{-2}. Assuming that the center of the clump is at the position of the peak of the column density at α=07^{h}049^{m}46.60$'$, δ=04^{d}32^{m}32.006$'$, I have measured the column density N_{HI} along the right ascension and the declination axis. In diagram. 6.47, the plot of the average column density versus the radius in pixels is given, where one pixel equals 1$'$. From the diagram it is seen that the column density distribution can be approximated nicely by a Gaussian function. A fit of a Gaussian function to the diagram gave a full width at half maximum of 6.4$'$. This is considered to be the diameter of the object.

I have calculated the first moment which is the intensity-weighted velocity of the spectral line as a measure of the mean velocity of the gas and the velocity field of the gas. I over-plotted the velocity field over the column density of the object in Fig. 6.49. The velocity field resembles a stable entity whose motions are gravitationally bound, rotating under the influence of gravity. Especially in the inner part it has equally spaced parallel contours expected for a solid body rotation velocity field. The minor axis around which the motion takes place has υ_{lsr} =47.7 km s^{-1} while the average velocity dispersion υ_{σ}=0.47 km s^{-1}. It is also interesting to note that the minor axis has a direction which seems to be almost perpendicular to the Galactic plane.

A velocity field like this is not observed in the other HI clumplets, which are most probably supported by external pressure and they are not expected to be gravitationally stable. I have used the SIMBAD database to search around the position of the peak

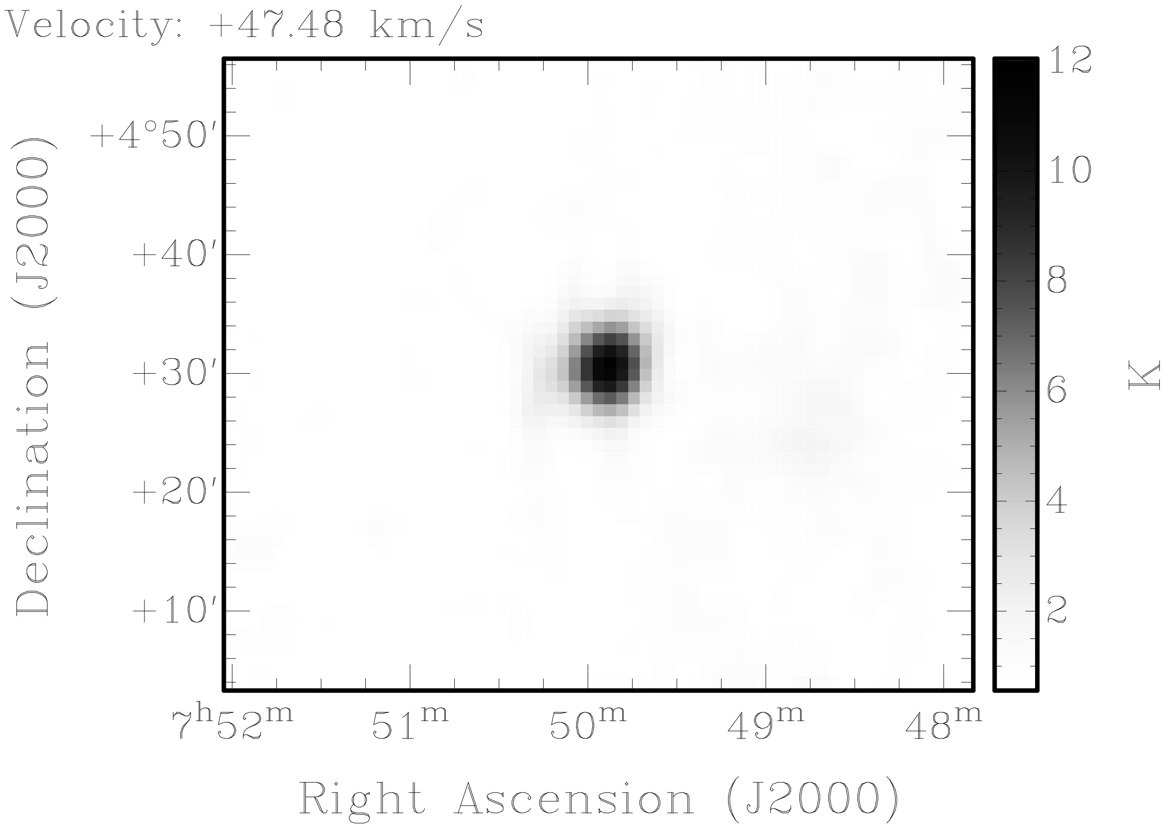

Fig. 6.45: *A RA-DEC map of the* HI *emission centered at position* α*=07*^{h}*049*^{m}*46.60*$''$*,* δ*=04*^{d}*32*^{m}*32.006*$''$*. Emission below* σ_n *of 0.6K has been cut.*

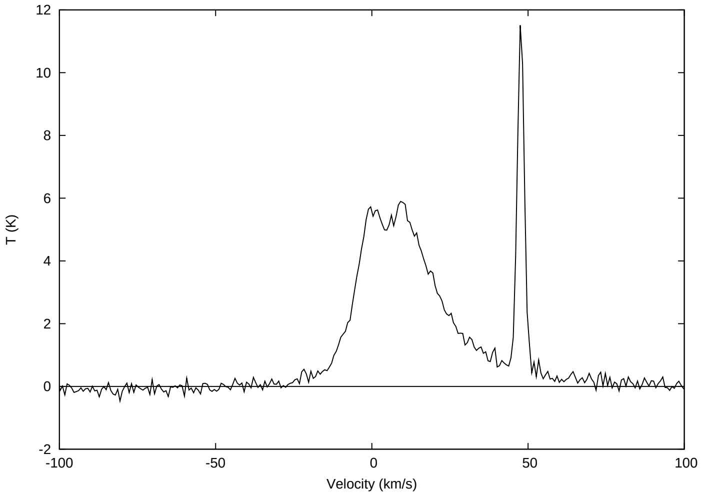

Fig. 6.46: *A spectrum of the clump 215.54+15.04 taken with the Arecibo 300m telescope. The peak of the clump is seen at* υ_{lsr} *=47.48km s*$^{-1}$*.*

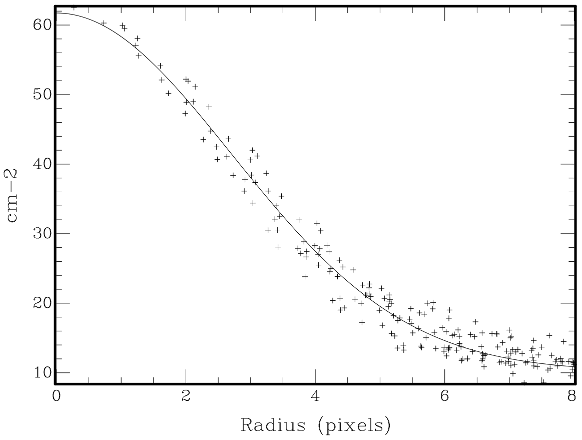

Fig. 6.47: *A diagram of column density N_{HI} versus radius R of the clump in pixels. One pixel represent the distance of 1′. The plot was generated by azimuthally averaging the image plane data and producing a plot of average value versus radius. It was then fitted with a Gaussian function.*

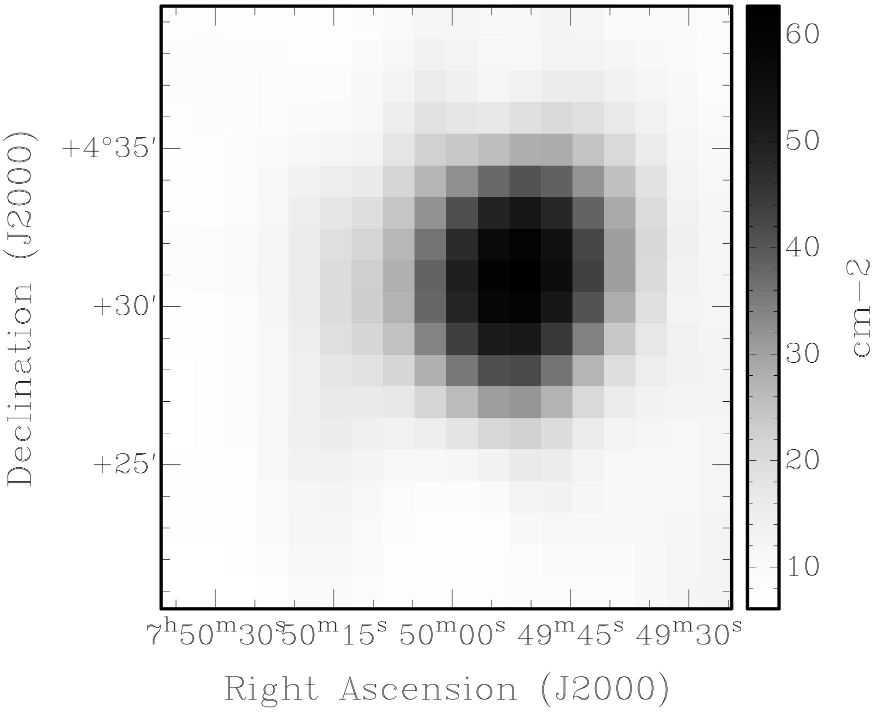

Fig. 6.48: *A column density map of the clump 215.54+15.04. The unit are in 10^{18} cm^{-2}.*

of the column density to a radius of 6′ for objects that have enough HI and may be associated with this position. No object was found at this position. Since also the velocity dispersion is very small I have excluded the possibility of it being a galaxy.

Assuming that it is a HI clumplet as part of the gaseous halo and following the Galactic

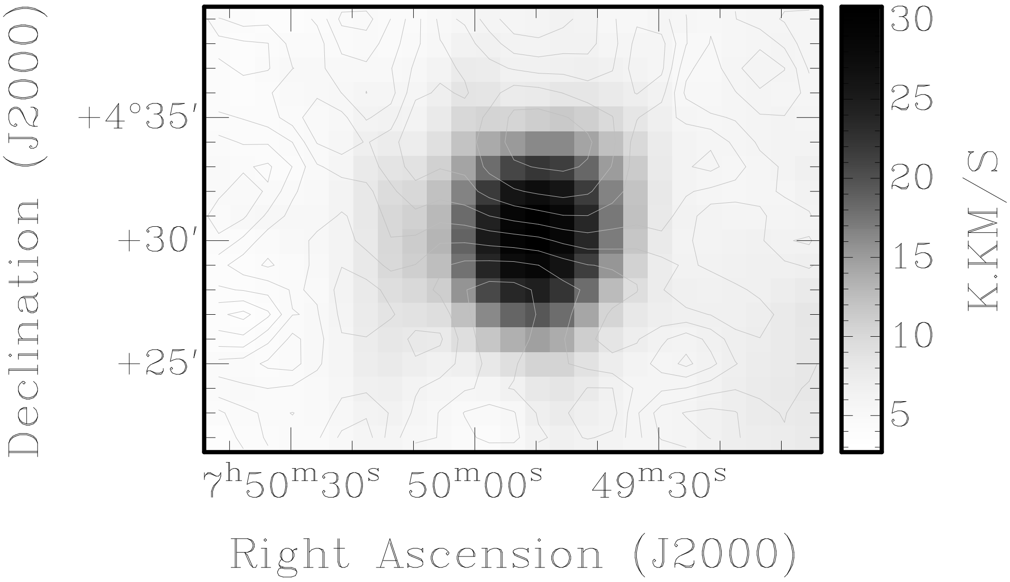

Fig. 6.49: *A RA-DEC map of the column density of the* HI *object. Overlaid as contours is the first moment map of the HI object. The contour levels start from the min (lower declination) of 47.1 km* s^{-1} *up to the max (higher declination) of 48 km* s^{-1} *with a step of 0.1 km* s^{-1}*, half of the velocity resolution of the cube. The units of the column density are in* 10^{18} cm^{-2}*.*

rotation, I can estimate the distance. I considered the velocity of the peak to be the central velocity of the clump and for υ_{lsr} =47.7km s^{-1}, I estimated a distance $d = 5.8 \pm 0.7$ kpc, galactocentric radius $R = 13.5$ kpc and height $z = 1.5$ kpc. For this distance the diameter of the HI clumplet is 10.8±2.1 pc. This implies an average peak volume density of $< n_o > = 1.87 \pm 0.5 \cdot \mathrm{cm}^{-3}$. Assuming the clump is spherical and the volume density distribution is described by a Gaussian function, the total mass of the HI in the clump is $M_{HI} = 70 \pm 30$ $\mathrm{M}_\odot$.

I will now try to calculate the mass M in a different way. If the object is stable, as appears evident from its rotation, it must be gravitationally bound. Then it is easy to calculate the mass from the virial theorem $M_v \sim \frac{u^2 \cdot R}{G}$. Assuming that the virial radius is 5.4 pc, and that the observed velocity dispersion is due to rotation, then the mass is $M = 273 \pm 270$ $\mathrm{M}_\odot$. This is ~4 times larger than the mass estimate M_{HI}=70±30 $\mathrm{M}_\odot$. A simple error propagation analysis shows that the error in the estimate of M_v depends strongly on the uncertainty of the velocity measurement. Since our velocity resolution is coarse in comparison to the velocity dispersion, a possible uncertainty in the determination of velocity is high. So it is difficult to decide whether the assumption of gravitational stability is true, whether the distance determination is wrong and the clump is further out, or whether the clump contains an important amount of additional baryonic matter like H_2 which it is difficult to detect. One possible model which can explain the characteristics of an objects similar to the one we observed was proposed by Kiguchi et al. (1987). In it, under the assumption that a cloud is embedded in a stationary extended medium and is axisymmetric, both conditions met for our object, the equilibrium structure of rotating isothermal clouds is calculated. It is found that for a stable configuration the central volume density ρ_c must be 30 times larger than the boundary volume density ρ_* and the radial profiles are given for a number of parameters such as rotational and angular velocity and mass. Unfortunately the Arecibo data do not probe deep enough nor do they have the necessary velocity resolution to give the necessary information regarding the boundary conditions and the velocity field, so more synthesis observation with high dynamical range and spectral resolution are currently underway to test the validity of this model.

7 Thermal equilibrium of the neutral component of the gaseous Galactic halo as inferred from the study of the physical properties of HI clumps

7.1 Introduction

In the previous three chapters I have presented the observational and physical properties of a sample of HI clumps detected with the Effelsberg and Arecibo telescope, associated with the neutral component of the gaseous Halo. Follow-up observations for two of the Effelsberg HI clumps were done using the WSRT and the VLA synthesis array. A comparison of the physical properties of our sample with models for the neutral ISM, like the model in Wolfire et al. (2003), can give us an insight into the condition of the neutral gaseous Halo. The model in Wolfire et al. (2003) describes the balance between different phases of the neutral ISM as function of the constituents of the ISM (i.e., metalicities, dust-to-gas ratio, etc).

In this chapter, I will first summarize the properties of all the different sample of HI clumps detected with different telescopes and by different observers. A short description of the model in Wolfire et al. (2003) will follow. Finally I will compare my sample of the HI clumps with the model and discuss stability and evaporation of the HI halo clumps.

7.2 Summary of the Observational and Physical Properties of the HI clumps.

Before comparing the physical properties of my sample with the thermal equilibrium model for the neutral phase of the ISM, it is useful to make a comparison between the samples of HI clumps observed using different telescopes in different parts of the Milky Way. Besides estimating the effect of telescope resolution in measured properties of the clumps, it is possible to evaluate in what extend all the samples are part of the same population of Galactic material.

The 90% range of the properties of the HI clumps is given in Table.7.18, while in Table. 7.19 the median of the properties is given. The sample of this work is divided in four parts, in the Effelsberg telescope sample, in the Arecibo telescope sample, in the VLA sample and in the WSRT sample. The tables also include the sample detected with the 100-m GBT telescope (Lockman, 2002) with a resolution similar to the one of the Effelsberg telescope, the sample detected with the Arecibo telescope (Stanimirović et al., 2006) and the sample detected in the VLA Galactic Plane Survey (Stil et al., 2006). Lockman (2002) and Stil et al. (2006) used the terminal velocity (Chap. 2) to determine the distance since they probe the inner Galaxy. Stanimirović et al. (2006)

estimated the distance in the observed anti-center region using pressure equilibrium considerations. This is the only applicable method in this region but shows the largest distance uncertainty (Chap. 8).

As already discussed in Chap. 4 the Effelsberg and the GBT sample, despite originating from different parts of the Galaxy, generally show very similar properties. For comparison the samples from the VLA, WSRT, and Arecibo observations, while measuring column density of the same order, have detected HI object which are denser, smaller and possibly in equilibrium with their surroundings. These objects are associated with the small scale sub-structure of HI clumps and defined as cores. This difference in the observations, is the result of the telescope resolution. The $9'$beam resolution of the Effelsberg and GBT telescopes do not resolve the $\sim 1'$ sized HI cores. They are measured as a single structure, an HI clump, with a median size of $18'$ in case of the Effelsberg telescope. On the other hand VLA and WSRT have the necessary resolution to resolve these HI cores and as a result the sample has an average angular size of $1.4'$ and $1.2'$ respectively. In the case of the 300-m Arecibo telescope with a resolution of $\sim 4'$, the sample has a mean size of $6'$. So the size of the detectable HI object is between the size observed with the single dish Effelsberg observations and the interferometry observations. The effect of telescope resolution can be proven further by the comparison of the Arecibo sample (Stanimirović et al., 2006) with the samples obtained by the other telescopes. The quantities which are unaffected by the resolution of the observations, column density N_{Hi} and the line width $\Delta\upsilon_{1/2}$, show a median similar to the GBT and the Effelsberg sample. The quantities which depend on the telescope resolution, have ranges similar to my Arecibo observations and close to the interferometry observation. Therefore lower angular resolution tends to smooth over the clumps, so that the conglomeration of cold HI cores surrounded by the warm HI envelope appears as a single HI clump while high angular resolution observations can observe these cores directly.

Regarding the properties, all samples besides Stil et al. (2006), have column densities of the order of $10^{19}\mathrm{cm}^{-3}$ independent of the distance. This is a range expected for both the cold and the warm neutral medium, for $b>10^\circ$ as measured from absorption studies (Heiles & Troland, 2003b). Stil et al. (2006) probes a region along the Galactic plane with $b<10^\circ$. According to Heiles & Troland (2003b) it is expected to show higher column densities N_{Hi} of the order of $10^{20}\mathrm{cm}^{-3}$. For the line widths, $\Delta\upsilon_{1/2}$, all the different samples measure very narrow lines, as seen from their median in Table. 7.19, with the GBT sample skewed towards higher widths and the WSRT sample skewed towards smaller widths. Since the ISM is turbulent (Chap. 9), the thermal temperature of the clumps is expected to be lower than the one measured.

The similarity in these two properties, the column density and the line widths, and additionally the similar angular size as seen in Table. 7.18 points to the fact that all the HI clumps in the different HI samples belong to the same population which is spread out at different heights. Regarding the Stil et al. (2006) sample, it has higher

	N_{Hi} 10^{18} cm^{-2}	$\Delta\upsilon_{1/2}$ km s^{-1}	s $'$	D pc	<n> cm^{-3}	M_{Hi} $M_{\odot}$	d kpc	R kpc	|z| kpc
Effls.	6-68	3.0-11.6	9-27	9-60	0.07-0.7	4-770	3.5-9.5	10.5-15	1-3.7
Arcbo.	30-88	3.4- 6.8	4- 9	4-20	1.0 -4.1	7-160	4 -10	17 - 12	2.5-1.1
VLA	32-68	2.8- 5.8	0.9-1.7	2-6	2.2 -5.7	7-32	9-10		
WSRT	14-28	2.9- 3.9	1- 1.7	2-5	1.6 -3	1-11			
Lockman	7-63	5.4-26.3		19-35	0.1-0.9	12-290			0.6-1.2
Stanim.				0.5-8	0.8-13	0.03-7	0.2-3		0.6-0.9
Stil	90-390	4.2-11.7		1.9-11	3.4-18.4	3-20	12-250	4.3-7.7	0-0.2

Tab. 7.18: *A comparison between the samples of* HI *clumps observed with different telescopes. The table gives the 90% range of values of the* HI *clumps for all cases except Stanimirović et al. (2006). Lockman (2002) was using the 100-m GBT and the distance was estimated using the terminal velocity. In Stanimirović et al. (2006) the observations were done using the 300-m Arecibo telescope and the distance was estimated using pressure considerations. In Stil et al. (2006) the clumps were detected using the VLA and the distance was estimated using the terminal velocity. In Lockman (2002) and Stil et al. (2006)* HI *clumps are located in the inner Galaxy. In Stanimirović et al. (2006) the clumps lie in the anti-center region.*

column densities for the same angular size of clumps at similar Galactocentric distance R, therefore resulting in the other derived physical parameters like the volume density $< n >$, the diameter D and pressure P to have higher values in comparison with the other samples. Taking into account the uncertainty in the distance determination in my samples and that of Stanimirović et al. (2006) and the uncertainty in the size in the sample from Lockman (2002), it is difficult to compare the total HI masses and the diameters between different telescopes. The GBT and the Effelsberg telescope have similar resolutions, while the distance determination of the GBT clumps using the terminal velocity is the most accurate method. The fact that the range of mass and diameter is similar, indicates that also the estimate for the distance with our method is quite good, assuming of course that I detect a population of clouds with the same properties. For my Arecibo results and those from Stanimirović et al. (2006) it is difficult to compare the diameters and the mass and volume densities since the uncertainty in the distance estimate through pressure arguments is too large. Finally the authors in Lockman (2002), Stanimirović et al. (2006) and Stil et al. (2006) do not specify the density of clumps per degree, therefore it is difficult to determine if there is a difference between the inner and the outer Galaxy.

7.3 Thermal equilibrium in the neutral gas

In this section I will give a brief summary of the analytical model which gives a detailed description of the physical conditions under which it is possible to have the co-

	N_{Hi} 10^{18} cm^{-2}	$\Delta\upsilon_{1/2}$ km s^{-1}	s $'$	D pc	<n> cm^{-3}	M_{Hi} M$_{\odot}$	d kpc	R kpc	|z| kpc
Effls.	25	5.2	18	34	0.2	120	7.5	12.5	2.5
Arcbo.	57	4.3	6	8	1.9	26	4	12	1.4
VLA	40	4.3	1.4	4.5	3.8	15	9.5	14.5	3.8
WSRT	16	3.3	1.2	2.6	2.3	4	7	13	2.5
Lockman	20	12.2		24	0.2	50			0.9
Stanim.	20	4							
Stil	180	5.6	4.1	7.9	7	64	7.2		0.1

Tab. 7.19: *A comparison between the median values of the* HI *clumps observed with various telescope. In Lockman (2002) the observations were done using the 100-m GBT and the distance was estimated using the terminal velocity. In Stanimirović et al. (2006) the observations were done using the 300-m Arecibo telescope and the distance was estimated using pressure considerations. In Stil et al. (2006) the clumps were detected using the VLA and the distance was estimated using the terminal velocity. Lockman (2002) and Stil et al. (2006) clumps lie in the inner galaxy. In Stanimirović et al. (2006) the clumps lie in the anti-center region.*

existence of the cold neutral medium (CNM) and the warm neutral medium (WNM) (Wolfire et al., 2003, 1995a). The model was compared with the derived physical properties of the HI clumps to test the possibility of thermal equilibrium between the clumps and an existing envelope.

In the model it is assumed that the CNM and the WNM are heated by photoelectric processes. This means that the energy induced by the far UV field (FUV) of the OB stars is converted to heat by small dust grains and PAH's (polycyclic aromatic hydrocarbons) with a heat efficiency ∼3%. The major role of the X-ray background and the cosmic rays is to regulate the efficiency of photoelectric heating. The primary mechanism for the cooling of the CNM is through the CII (158μm) while the primary mechanism for the cooling of the WNM is through the Lyα,CII (158μm) and OI (63μm) with the electron recombination mechanism also playing an important role. It is assumed that the time of the cooling is smaller than the time between shocks in the ISM.

The CNM phase of the neutral gas and the WNM phase of the neutral gas can co-exist in thermal equilibrium only in a very narrow range of pressures and densities. The authors calculated this range for different Galactocentric radii. Table 3 of Wolfire et al. (2003) gives an overview of the acceptable conditions. A phase diagram of thermal pressure versus volume density of hydrogen nuclei can be produced to show the range of pressures and densities where the two phases can co-exists. A phase diagram from different Galactocentric radii is seen on Fig. 7.50. In this diagram gas can exist in stability in regions where $dP/dn > 0$. In the unstable region gas will move either towards the warm branch on the left or toward the cold branch on the right.

It is obvious from the description of the model that the range of pressures depends

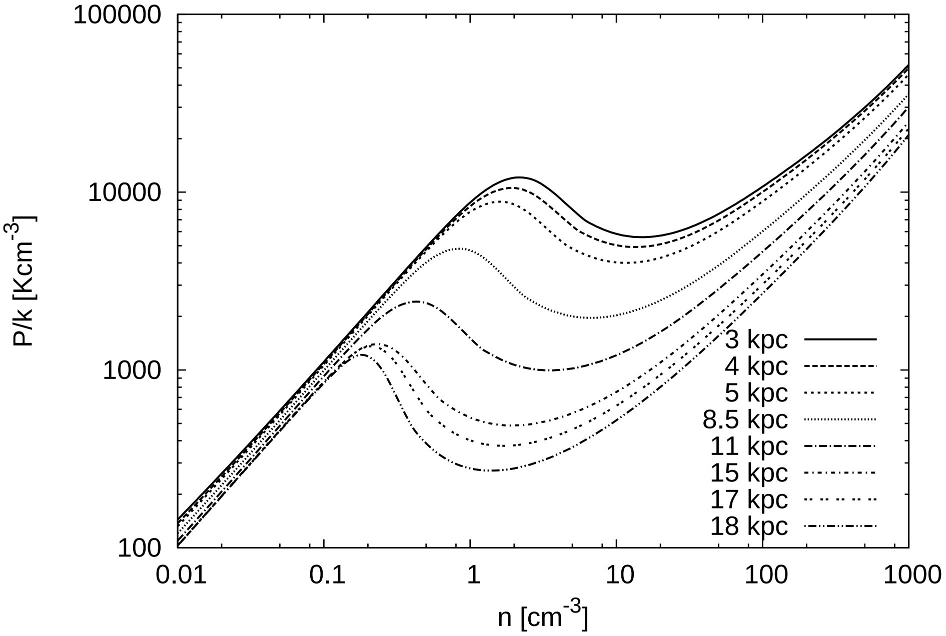

Fig. 7.50: *Phase diagram depicting thermal Pressure P/k vs hydrogen nucleus density n at different Galactocentric radii. The curves apply for column density of the order of* $10{\cdot}10^{18}$ cm^{-2}*(Courtesy by Wolfire).*

strongly on the properties of the ISM and the strength of the FUV field. Different dust-to-gas (D/G) ratio and metalicity Z will affect the two branches of the phase diagrams. For example a drop of the dust-to-gas ratio D/G from 1, assumed for the calculations, to 0.3 will see a drop in the P_{min} and P_{max} and an extension of the CNM branch to the left. The dependence of the phase diagram on the constituents of the ISM is discussed more thoroughly in Wolfire et al. (1995c).

7.4 HI clumps and thermal equilibrium

In this section I will present the comparison of the derived pressures P and volume densities $< n >$ of my sample with the phase diagrams of the model and Table 3 from Wolfire et al. (2003). It is important to note that the average volume density $< n_H >$ in the theoretical phase diagrams refers to the total density of the hydrogen nuclei, which is $n_H \sim n_{HI} + n_{mol}$ where n_{HI} is the volume density of the neutral hydrogen and n_{mol} is the volume density of the molecular hydrogen. From the line observations at 21-cm I can estimate the average HI volume density n_{Hi} , while the molecular content for the HI clumps remains unknown. Based on data from the Far Ultraviolet Spectroscopic Explorer (FUSE) satellite, molecular hydrogen was detected in absorption in an extended IVC, with a column density $\sim 0.01{\cdot}10^{18}$ cm^{-2} (Richter et al., 2003).

Assuming, similar molecular hydrogen contents for the HI clumps, there are two possibilities:

- The molecular hydrogen has the same filling factor as the HI clump so the average density is very low and can be safely neglected
- the molecular hydrogen has a very low filling factor, implying a high density which cannot be neglected in the calculation of the total density of the hydrogen nuclei.

The molecular content in my sample has not been studied extensively. The general consensus is that in the latitudes where the clumps are found, the molecular content is usually very low (Crane, 1988). Therefore I assume the first possibility to be true so than $n_H \sim n_{HI}$ where n_H is the total average volume density of the hydrogen nuclei and n_{HI} is the average volume density of the HI in the clumps.

Another important factor that needs to be taken into account, is that the phase curves of the model are calculated for the Galactic plane while my clumps reach heights up to a few kpc above the disk. The authors in Wolfire et al. (2003) assume that the FUV depends only on the surface density of the OB-stars and changes as a function of radius. But since the OB-stars have a scale height of up to 0.07kpc (Reed, 2000), due to dust extinction from the disk and the lack of UV from the upper 2π of the Galaxy and great distances, the FUV field is expected to be lower (Wolfire et al., 1995c). Depending also on the exact condition of the formation of the HI clumps, metalicities and dust-to-gas ratio content, the phase diagram for the halo may differ from the disk phase diagram. Nonetheless from Fig. 1 of Wolfire et al. (1995c) it appears that a) only in the case of primordial gas which has low metalicity and dust-to-gas ratio the results vary significantly and b) for heights up to 4kpc the phase curve does not deviate significantly from the disk curve. It shows slightly smaller P_{min} and P_{max} values resembling disk phase curves at higher Galactocentric radii.

First I will compare to the phase diagrams the sample of HI clumps detected with the 100-m Effelsberg telescope. Fig. 7.51 is showing the comparison between the phase diagram and the HI sample. The plot includes also two points where the pressure and volume density were estimated for the broad extended envelope of the HI clumps. As seen in the figures one of the envelope is located in the region of thermal stability for the warm gas. It is also within the range of pressures where it is possible for cold gas to co-exist with envelopes. The second extended envelope has a volume density expected for the warm gas but the pressure is low. For the HI clumps, in Fig. 7.51, it is seen that 60% of them are located well outside the region of thermal stability and pressure equilibrium, strongly violating isobaric conditions. The clumps have volume densities appropriate for the warm medium, with some of them having pressures even lower than the extended envelopes. This result contradicts the observed narrow line widths $\Delta\upsilon_{1/2}$ of the HI clumps which imply low kinetic temperature T_{kin} in agreement with

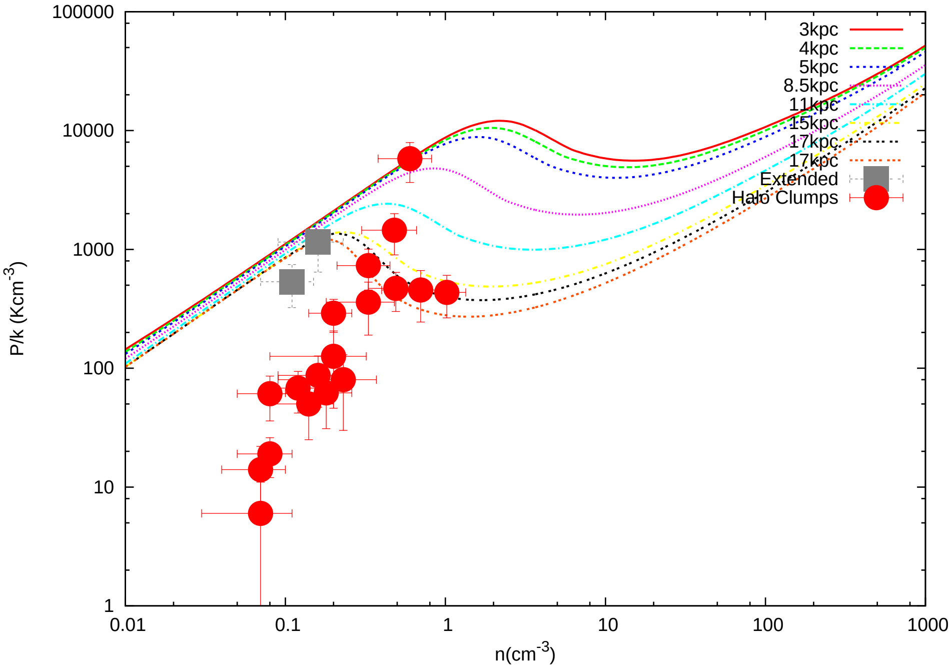

Fig. 7.51: *A comparison between the Effelsberg sample of* HI *clumps and the phase diagrams depicting thermal Pressure P/k vs hydrogen nucleus density n at different Galactocentric radii. The curves apply for column density of the order of* $10{\cdot}10^{18}$ cm^{-2}

the temperatures predicted for the corresponding Galactocentric distances from the model in Table 3 (Wolfire et al., 2003). As discussed in Chap. 4, the above result points to the presence of small scale sub-structure in the clumps which is found in the interferometry observation for two of them. For the HI clumps 117.94+24, 117.51+25.19, 115.35+23.35, as discussed in Chap.4, an $\Delta\upsilon_{1/2}$ greater than 10 km s^{-1}implies an association with the extended warm medium rather than the cold clumps. For the remaining 4 HI clumps, 112.-12.44, 116.5+21.45, 113.33+27.00, 112.96-13.03, the Table 3 from Wolfire et al. (2003) shows that for their respective locations, the volume densities and pressures lie outside the range for isobaric thermal equilibrium. The low pressure can imply, as for the other clumps, a presence of sub-structure while the low column density may imply molecular gas. It cannot be excluded that the clumps are thermally unstable, either condensing or expanding.

The Arecibo sample of HI clumps gives a different result. In Fig. 7.52, the phase diagram versus derived pressures and volume densities are depicted for a range of Galactocentric radius from 11 kpc up to 20kpc. In comparison with the Table 3 of Wolfire et al. (2003) and also in the phase diagram, the clumps have the necessary pressure corresponding to the region of thermal equilibrium. The densities are generally smaller than the ones expected for the cold phase, so in Fig. 7.52 they clutter in the thermal instability region. This implies that the clumps are in a transition phase either condensing, becoming colder or expanding and becoming part of the warm compo-

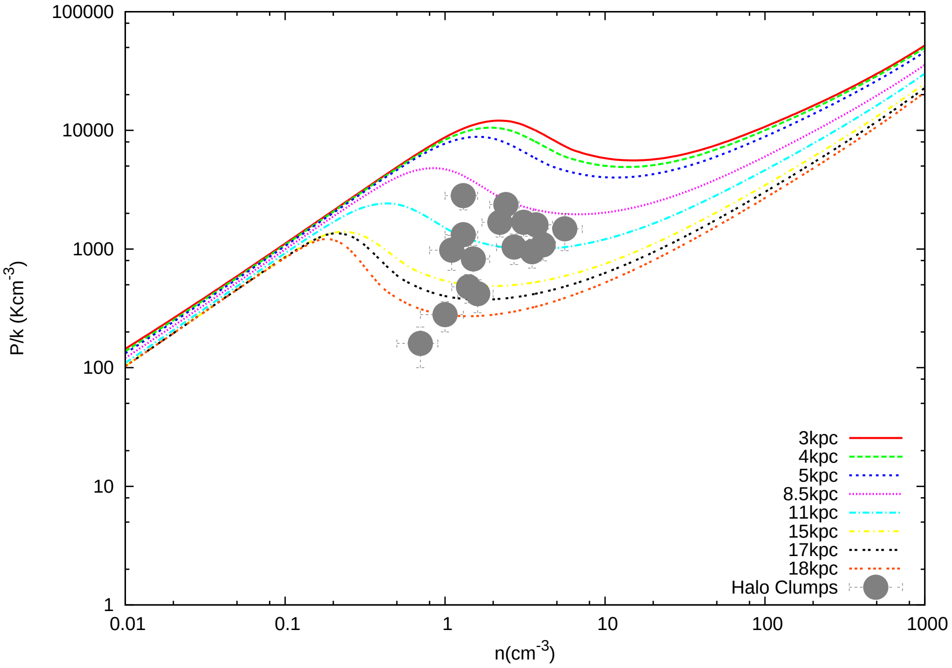

Fig. 7.52: *A comparison between the Arecibo sample of* HI *clumps and the phase diagrams depicting thermal Pressure P/k vs hydrogen nucleus density n at different Galactocentric radii. The curves apply for column density of the order of* 1010^{18} cm^{-2}

nent. Of course the unknown molecular content cannot exclude the possibility that the clumps are actually in thermal equilibrium with the surroundings. The good agreement of the Arecibo sample with the phase diagram as seen in the Fig. 7.52 in contrast to the strong deviation of the Effelsberg sample in Fig. 7.51 is a result of the different resolution of the two telescopes. The Arecibo telescope as a result of the $3.5'$ beam can discern better the substructure of the clumps while the $9'$beam of the Effelsberg telescope is not good enough, as is evident from the interferometry observation, to resolve the cold cores. As a result the properties of the Arecibo sample should be compared with the interferometry samples and not with the Effelsberg sample.

Fig. 7.53 shows the comparison between the VLA/WSRT core samples and the phase diagram. The HI cores of the VLA have $R \sim 15$ kpc, while the WSRT cores have an estimated R from 13kpc up to 15 kpc. A comparison with the phase diagram corresponding to the same Galactocentric radii shows that the WSRT cores with υ_{lsr} =-68 km s^{-1}are located barely within the range were thermal equilibrium is possible. For the WSRT cores at υ_{lsr} =-84km s^{-1}, one is located in the thermal instability region, the other core, while it has a volume density matching to the expected one for the CNM, exhibits smaller pressure than the one expected for the CNM at R=15kpc. For the VLA cores, while the volume densities are high enough to be in the cold phase, they exhibit pressures higher than allowed for their Galactocentric radius. This can be explained assuming that the turbulence is dominant in the region of the core and it af-

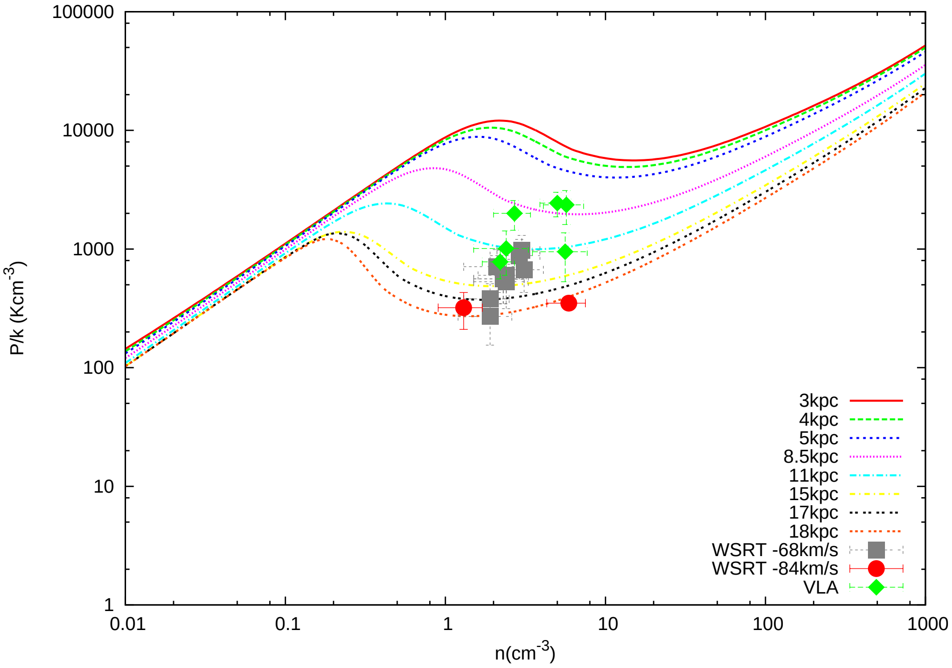

Fig. 7.53: *A comparison between the WSRT & VLA samples of* HI *clumps and the phase diagrams depicting thermal Pressure P/k vs hydrogen nucleus density n at different Galactocentric radii. The curves apply for column density of the order of* $10 \cdot 10^{18}$ cm^{-2}

fects strongly the T_{kin} measured from the line width $\Delta\upsilon_{1/2}$ and thus the pressure. All in all, it seems that the cores found with the interferometer can be in thermal equilibrium with the thermal gas, even without taking into account the presence of molecular hydrogen.

7.5 Stability and evaporation of the HI clumps

The HI halo clumps in this work detected with the Effelsberg 100-m telescope are gravitationally unstable as discussed in Chap. 4. When observed with a high resolution, two of the HI clumps are resolved in a number of cold cores. Using the relation 12.75 from Rohlfs & Wilson (2004) to estimate the virial masses, yields values from 2500 $M_{\odot}$ up to 11000 $M_{\odot}$ for the cores. This is three orders of magnitude higher than the estimate of the total visible HI mass for the cores. Similarly, the HI clumps detected with Arecibo have virial masses from from 1700 $M_{\odot}$ up to 125000 $M_{\odot}$, which is two to three orders of magnitude higher than their HI masses. Therefore even the cores do not seem to be gravitationally stable. The single dish observations (Chap.3,6) have detected a broad faint extended medium. The Arecibo HI clumps and the HI cores can be in thermal equilibrium with this envelope as seen in the previous section. In this case it implies that the cores exist in isobaric conditions, so the envelope engulfs them and confines them. In the absence of such an envelope the HI core will disperse. In the case of the VLA cores their lifetime is $t_{disp} \sim 0.8$Myrs while for the WSRT cores their lifetime is $t_{disp} = 0.4$Myrs. The Arecibo HI clumps have a longer lifetime of $t_{disp} = 2$Myrs. This absence of external support and self-gravitation implies that the clumps are dynamical entities constantly destroyed and formed by the turbulence in the ISM (Mac Low & Klessen, 2004)

The presence of an extended warm envelope plays an additional role for the cores. It protects them from fast evaporation. Using equation 47 from McKee & Cowie (1977) shows that in the absence of a warm envelope, for a hot medium of 10^6K (temperature of the halo plasma) the mass loss, in the case of the VLA and WSRT cores with an average diameter of 3.40 pc, is $\sim 4.5 \cdot 10^{18}\mathrm{g} \cdot \mathrm{s}^{-1}$. This in turn means that the core with an average mass of $\sim 10\ \mathrm{M}_{\odot}$ will evaporate in 142 Myrs. If the cores are embedded in a warm envelope with a temperature of ~7000 K (average temperature of the envelope in the thermal equilibrium region of the phase diagrams Wolfire et al. (2003)) then the mass loss due to evaporation is $\sim 3.7 \cdot 10^{17}\mathrm{g} \cdot \mathrm{s}^{-1}$, an order of magnitude lower, and the core will evaporate in 1.5 Gyrs. Therefore it seems that the warm envelope provides the ideal environment for the formation of cold condensations in the form of HI clumps which would be difficult to survive as isolated objects in the Galactic halo.

8 Power spectrum analysis of the Arecibo data

8.1 Introduction

Turbulence was recognized early on to play an important role in the astrophysical processes (Chandrasekhar, 1949). Turbulence in the ISM occurs when a dimensionless number, the Reynolds number which depends on length scale, the velocity scale and the kinematic viscosity, is greater than a critical value which is of the order of $10^2 - 10^4$. In case of the interstellar medium (ISM), a typical Reynolds number value is $10^7 - 10^8$, so its nature is expected to be highly turbulent (Scalo, 1987). In this case, turbulence defines the spatial distribution and affects the physical properties of the gas. In the HI gas turbulent motions are one of the major causes for the line broadening of the spectral lines, dominating usually over thermal broadening. In the case of the Galactic Halo gas, turbulent motions seem to be especially important. As discussed by Wolfire et al. (2003), the turbulence can define the spatial and temporal structure of the thermal pressure. It can help to transfer energy and mass from the disk to the Halo and to re-distribute it. But more importantly it is proposed that it is the large scale turbulent motion that provide the necessary support for the neutral gas layer of the Galactic Halo (Lockman & Gehman, 1991; Kalberla & Kerp, 1998). Galactic rotation (Fleck, 1981) is possibly generating the large scale motions. In this chapter, I will use the Arecibo data cube, which is able to probe different spatial scales, to study the turbulent nature of the HI gas in a statistical sense in the probed regions.

8.2 Analysis

Turbulence gives rise to stochastic random fields which are expected to be correlated (Pogosyan & Lazarian, 2005). The best way to study turbulence is using a statistical description. The correlation function of the density field $\rho(x)$ depends only on the distance r between two points and is given by $C(r) =< \rho(x) \cdot \rho(x+r) >$. From the Wiener-Khinchin theorem it is given that the Fourier transform of the auto-correlation function $C(r)$ equals to the square of the Fourier transform of the $\rho(r)$, called power spectrum $P(k)$. Kolmogorov (1941) found that for an unmagnetized incompressible viscous fluid the direction averaged 3D-energy spectrum is given by the Kolmogorov scaling $E(k) \sim 4\pi k^2 P(k) \sim k^{-5/3}$ where $P(k)$ is the power spectrum. This means that over the inertial range where neither energy injection nor energy dissipation is important, the energy spectrum can be described by a single power law. The power spectrum of the Kolmogorov turbulence is described by a power law $P(k) \sim k^\gamma$ where the spectral index γ is given by $\gamma = \tau - N$ (Pogosyan & Lazarian, 2005) as a function of the correlation scaling τ and the dimensionality of space N. In the case of a Kolmogorov power spectrum $n = -2/3$. Studying the power spectrum of a spatial distribution can give us information about the nature of the turbulence.

From an HI observer's points of view, an HI data cube is a collection of channel maps with brightness temperatures which depend to the first order on the density distribution. Each channel defines a position-position map which give us the density fluctuation at a specific υ_{lsr} . Since I have established in Chap. 2 that a specific υ_{lsr} translates to a specific distance, we can assume that a channel maps gives us the density field $\rho(x)$ at this specific distance. Therefore, taking the square of the Fourier transform of the map, we are able to calculate the spatial power spectrum (SPS) and thus studying the properties of the turbulence of the HI gas.

Studies of the spatial power spectrum (SPS) of the Galactic HI resulted in different values for the spectral index. Crovisier & Dickey (1983) applied the statistical study in a region along the Galactic plane at $l \sim 52^\circ$ using WSRT data and single dish data from the Nancay and Arecibo telescopes. They covered a spatial frequency range from 100 to 6000 wavelengths ($0^\circ.5^{-1}$ to $35^{\circ-1}$) for the small spatial frequencies and found a typical index of -2.0 for the single dish observations and a typical index of -3.0 for the WSRT observation. Kalberla & Stenholm (1983), using a single dish telescope to study the HI both in emission and in absorption, estimated an index of -2.4 and -2.5 respectively. Dickey et al. (2001) used the data from the Southern Galactic Plane Survey and studied the SPS of the interstellar neutral hydrogen in the fourth Galactic quadrant along the plane. The power spectrum of the warm gas was found to steepen with an index from ~ -3 to 4 with the increase of the velocity binning. Since I had the opportunity to map a large area on the sky using the high resolution of the Arecibo telescope, I will calculate the SPS from the Arecibo maps to study turbulence in the lower halo region.

I have calculated the two dimensional spatially averaged power spectrum (SPS) for each velocity range of the image maps. The Arecibo data cube has a dimension of $990'$ by $330'$ with a pixel resolution of $1'$. So I can study the SPS from a scale of 16.5°down to the beam size of $3.35'$. The map is not corrected for self-absorption and it initially has 281 velocity channels with a channel width of $\sim 0.7 \mathrm{km\,s^{-1}}$. To calculate the 2D SPS for a specific channel width, for each velocity υ_{lsr} , first of all I applied the FFT algorithm from MIRIAD and calculated the amplitudes of the Fourier transform of the image cube. Then the amplitudes were squared resulting in the uncorrected spatial power spectrum of the image cube H^2. For the Arecibo map the given temperature T_A is the convolution of the brightness temperature T_B with the Gaussian beam b of $3.35'$, $T_A = T_B \otimes b$. $T_B\ (x)$ is analogous to the density field $\rho(x)$ of the image map. The Fourier transform of the beam b is B and the Fourier transform of the $T_B(x)$ is F. Then the uncorrected spatial power spectrum H^2 is given by :

$$H^2 = B^2 \cdot F^2$$

To calculate the corrected power spectrum of the image F, which is connected with the true density distribution, we need to deconvolve the uncorrected SPS accordingly. This is done for the SPS of each velocity υ_{lsr} by dividing the uncorrected SPS by the

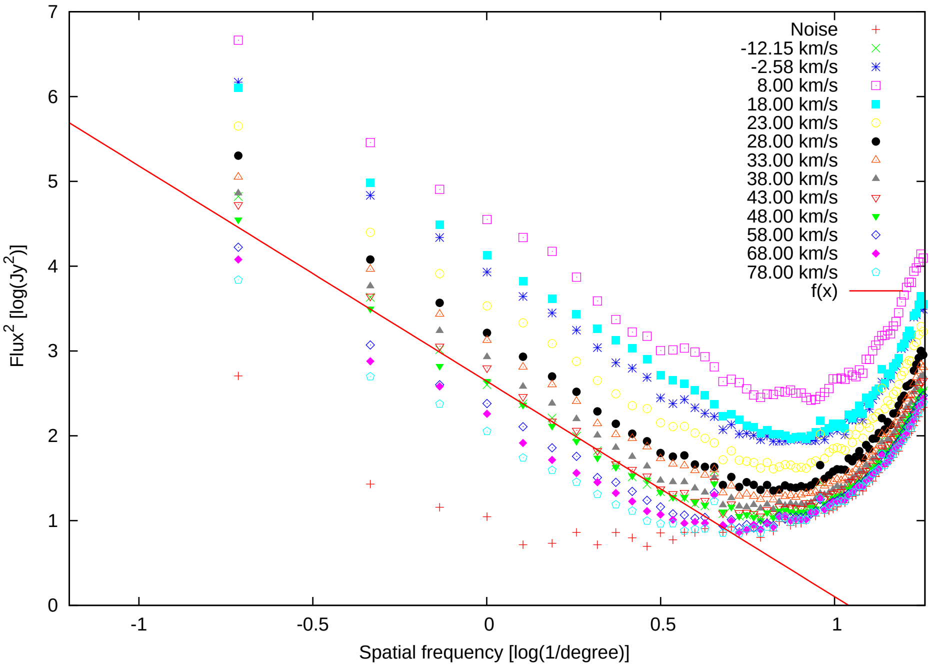

Fig. 8.54: *The spatial power of the* HI *emission in the Arecibo region. The x-axis is the spatial frequency measured as the logarithm while the y-axis gives the power in units of* Jy^2. *The plot shows the SPS for a range of velocities from -12.15km* s^{-1}*up to 78km* s^{-1}*with different color. The noise is the SPS of a channel where no emission is present. The function f(x) represents a power law with an index of -2.53 . The largest scale is 5°while the smallest scale is the beam size of 3.35′.*

Fourier transform of the Gaussian beam B. Once this is done, I estimated the average power spectrum for each velocity range. In the Fourier plane I averaged over 150 concentric annuli of equal width dk, where $k^2 = u^2 + v^2$ and u and v are the coordinates of the Fourier plane measured in wavelengths λ. The average 2-D SPS is fitted with a power law to extract the spectral index γ which is then compared between different velocities. Since for different channel width the line-of-sight depths varies, I finally calculated the 2-D SPS for different widths.

8.3 Results

Using the procedure described in the previous section I have calculated the 2-D SPS of the Arecibo image cube with a channel width of 0.7km s^{-1}, for the range of υ_{lsr} from -15 km s^{-1} up to 80 km s^{-1}where HI emission is present. Also the power spectrum for υ_{lsr} < -20 km s^{-1} was also calculated for channels were no HI emission is present. In Fig. 8.54 the SPS for a range of velocities from -12.15 km s^{-1} up to 78 km s^{-1} is shown. The plot covers two orders of magnitude in scale, from 5° down to the beam size of 3.35′. This figure shows that the SPS at all velocities, expect the channels

υ_{lsr} km s^{-1}	γ	A $(log(Jy^2)$
-12.15	-2.83	2.71
-2.58	-2.62	3.92
8.00	-2.71	4.53
18.00	-2.65	4.12
23.00	-2.64	3.54
28.00	-2.67	3.19
33.00	-2.61	3.09
38.00	-2.74	2.88
43.00	-2.58	2.72
48.00	-2.51	2.63
58.00	-2.40	2.36
68.00	-2.44	2.22
78.00	-2.35	2.05

Tab. 8.20: *The table gives the spectral index of the power law and the logarithm of the amplitude A for different υ_{lsr} for a velocity resolution of 0.7km s^{-1}.*

with no HI emission, can be fitted by a power law, over a range of angular scales from 5° down to $\sim 14'$. According to the Bonn Milky Way model this represents at υ_{lsr} =38km s^{-1} a length scale from 349pc down to 16.2pc. This can be interpreted as the inertial range where there is a lossless transfer of energy from larger to smaller scales. A least-squares-fit is applied to the SPS of each velocity to estimate the power law index γ. The results are given in Table 8.20. Considering only those velocities with a well defined amplitude $A \geq 3$, from υ_{lsr} =-2.58 km s^{-1} up to υ_{lsr} =33 km s^{-1}, we obtain an average index $\gamma = -2.65$. This has to be compared with the value -2.67 which is the expected index for a 2-D SPS of a Kolmogorov spectrum. Above 43 km s^{-1} the spectral index is shallower than -2.67 . This is evidence that the turbulence in the ISM in this region of the sky can be described as Kolmogorov turbulence. The spectral index found, ranging from -2.35 to -2.83 is shallower than the slope found in Dickey et al. (2001) for the ISM in the inner part of the Galaxy and closer to the index value of -3 found in Kalberla & Stenholm (1983). This implies that smaller scale fluctuations are important in this part of the Galaxy.

In the previous calculation I assumed that the measured 2-D spatial power spectrum reflects the real spatial density fluctuations of the regions probed. As discussed by Lazarian & Pogosyan (2000); Pogosyan & Lazarian (2005) the reality is far more complex, the resulting spatial power spectrum of an HI emission map depends both on the density and the velocity fluctuations caused by the turbulent field in the observed region. As a result the measured power index of the SPS might differ from the true index of the power spectrum of the density fluctuations. The measured SPS will be more shallow depending on the relative strength of the velocity fluctuation and the thickness(channel width) of the studied region. In other words this means that the velocity fluctuations can partially generate structures in the intensity maps at small scales which can be erroneously identified as clouds or clumps. This is a phenomenon very similar to velocity crowding although the origin is quite different.

To disentangle and study separately the effect of the velocity and the density fluctuations a method is outlined by Lazarian & Pogosyan (2000); Pogosyan & Lazarian (2005) where the 2-D SPS is estimated for slices of different velocity thickness, that is maps of different channel widths. Depending on the thickness we can infer the importance of the velocity fluctuations and then estimate the density index. Unfortunately different effects like the mixture of cold/warm gas, the velocity gradient, the thermal line-width etc make the interpretation of such a study a very complex task. Nevertheless I tried to study the behavior of the power spectrum for different channel widths and explain it with simple intuitive arguments. In order to do so, I initially averaged the image cube by different channel width from the original 0.73 $\mathrm{km\,s^{-1}}$ up to 56.21 $\mathrm{km\,s^{-1}}$. Following the method described in the previous subsection I then estimated the spatial power spectrum for all the channel maps of each channel width. I then fitted the spatial power spectrum for each channel map and estimated for each channel width the averaged slope over the range where there is HI emission. Finally I plotted the average slope of the power law against the channel width. This plot is seen in Fig. 8.55.

As seen from this figure, for channel width 0 $\mathrm{km\,s^{-1}}$ up to 20 $\mathrm{km\,s^{-1}}$ the power index increase is steep from ~ 2.6 to ~ 2.8. Above 20 $\mathrm{km\,s^{-1}}$, the index stays consistently within the range of 2.8-2.9. The spread of the values of the power law index in this channel width range is due to averaging processes and the fact that for channel widths more than 20$\mathrm{km\,s^{-1}}$ each HI data cube has very few channel maps. The behavior in Fig. 8.55 is expected since, as we average over more velocity channels the smaller structures which represent different true scale ranges over different υ_{lsr} 's, are merged together by averaging the maps. Thus the power in the small scales is decreasing while at the same time the power of the large scales is increasing which results in the steepening of the power index. After a specific channel width, which for our case is around 20 $\mathrm{km\,s^{-1}}$, the power remains constant. At this point the velocity fluctuations have most probably been smoothed out, so further velocity averaging cannot lead to an increase of the power index. The inertial range for the channel width of 20 $\mathrm{km\,s^{-1}}$ still goes down to $11'$ but this cannot be interpreted as a specific scale due to the averaging over structures of different scales. According to Lazarian & Pogosyan (2000), the index γ is then interpreted as the intensity power slope which is the results of the index of power spectrum of the density fluctuations n modulated by the power index of the velocity fluctuations m according to the formula $\gamma = n + m/2$. For the thinnest slice with an intensity power index of $\sim$-2.6 and assuming that the velocity fluctuations exhibit a Kolmogorov spectrum of a power index of 2/3, the index of the density fluctuations is then -2.93, which is very close to -3 given as a universal slope for the turbulent spec-

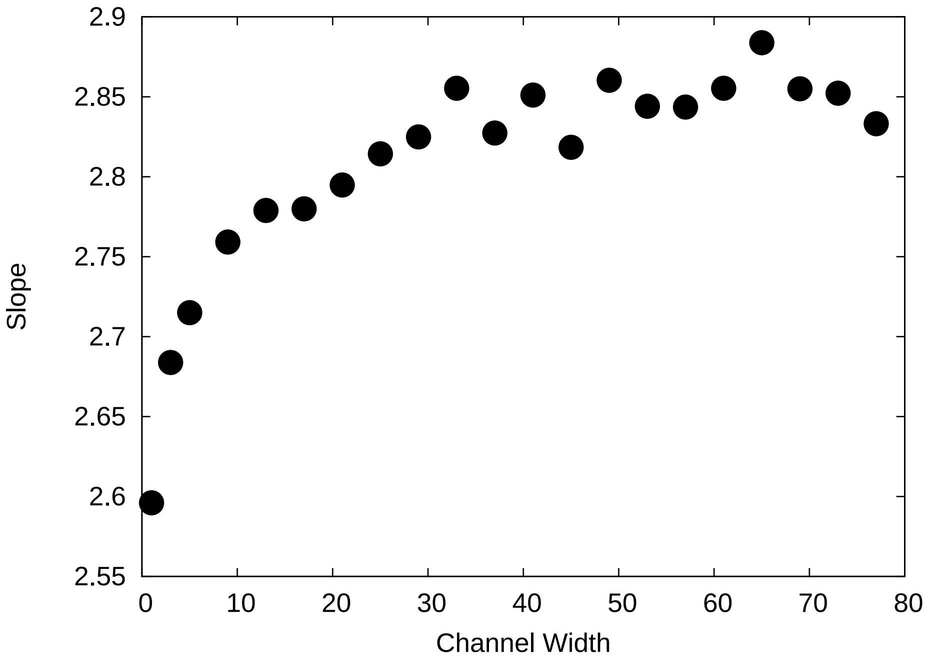

Fig. 8.55: *Power-law slope vs channel width. The power law slope for each channel width is the average over all the individual slopes for each channel map where there is* H I *emission.*

trum in Lazarian & Pogosyan (2000). In comparison to the similar study of Dickey et al. (2001) my results resemble the findings in region 2 at his study. This similarity is superficial since as explained the behavior of the index vs channel width in his studies is affected by self-absorption due to the very low-latitude of the studies. For my study on the other hand the region has relatively high latitude so I am not expecting it to be affected by self-absorption. Also it is important to note in this section that Lazarian & Pogosyan (2000) predicts that the changing of the velocity resolution stops affecting the SPS slope with channel width when it becomes larger than the thermal velocity width. For my study this is close to 20km s^{-1}, while this counts as high thermal velocity for cool gas, it can be considered to be the velocity of the warm extended medium in the neutral gaseous halo.

As mentioned in the previous subsection, I have applied a beam correction to the FFT map before calculating the average power spectrum. To test how this correction affects our results I have compared the SPS for the initial image cube with a velocity resolution of 0.73 km s^{-1} at two υ_{lsr} ranges, for 28 km $\mathrm{s}^{-1}$and 48 km s^{-1}. For the corrected and uncorrected SPS I estimated the slope using a least square fit. For the uncorrected spectrum I found in the case of υ_{lsr} =28 km s^{-1} a slope of -2.84 while for υ_{lsr} =48 km s^{-1} I got -2.58 km s^{-1}. In comparison with the slope of the corrected SPS which are -2.68 and -2.51 respectively, the uncorrected SPS has a slightly steeper power law. This is due to the beam correction which suppresses slightly the lower spatially frequencies but enhances at the same time the high frequencies. Still the uncorrected

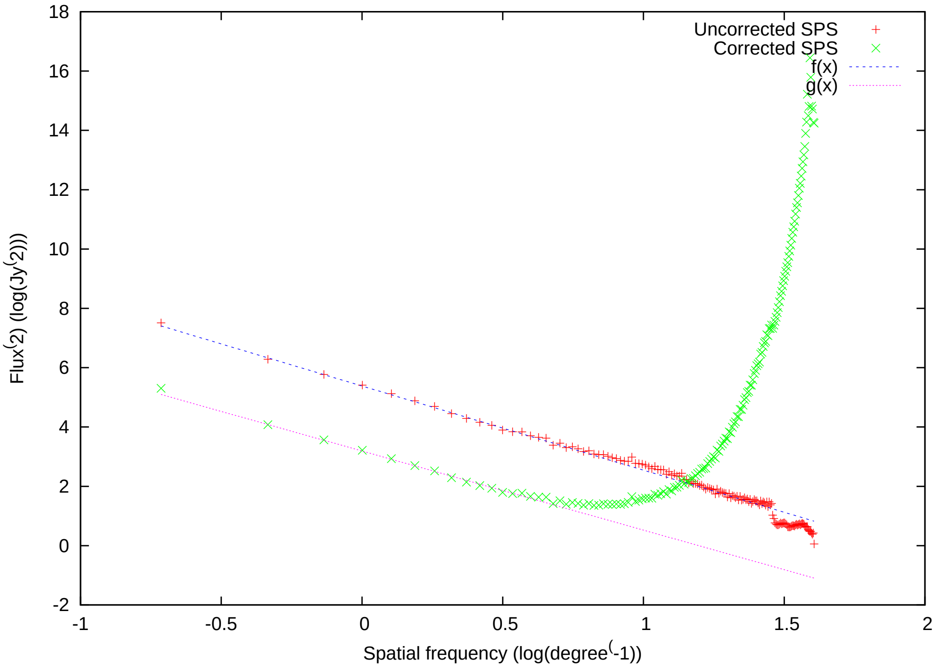

Fig. 8.56: *A comparison of the SPS for the corrected and uncorrected maps for a velocity width of 0.7km* s^{-1} *at* υ_{lsr} *=28km* s^{-1}*. Red dots are the uncorrected SPS while green dots are the corrected SPS. The red line is a fit to the former while the blue line is the fit to the later. The figure covers spatial scales from 10° down to 1.8′.*

slope is very close to the expected value of -2.67 for a 2D SPS. The beam correction cannot account for the difference between our results and the slope range of -3 to -4 estimated in Dickey et al. (2001). In Fig. 8.56 and Fig. 8.57, I give the SPS for υ_{lsr} =28 km s^{-1} and υ_{lsr} =48 km s^{-1} respectively, including both the uncorrected and the corrected SPS. Since I divided with the spatial power spectrum by the beam a different power law is expected. What is strikingly different between the two SPS for a specific υ_{lsr} is the inertial range. While in the case of the corrected spectrum the inertial range ends at a spatial scale of 12-14′, in the case of the uncorrected spectrum the inertial range appears to cover almost the total spatial range. High spatial frequencies however, are affected by beam smoothing and should be disregarded. As a final note I have reached to two important conclusions, first of all assuming that the modulation in the density fluctuation due to the velocity turbulent field is minimal, then the density 2-D spatial power spectrum exhibits a Kolmogorov like spectrum behavior. Second and most important is the realization that in case the velocity fluctuations are important in the study of the nature of the gaseous neutral Halo the HI intensity channel maps have to be interpreted with extreme care. All in all I do not claim this to be a complete study of the subject of turbulence in the gaseous neutral halo but a first analysis on the possible implications of turbulence in the halo. More thorough analysis is needed comparing different regions in different latitudes to reach more robust results.

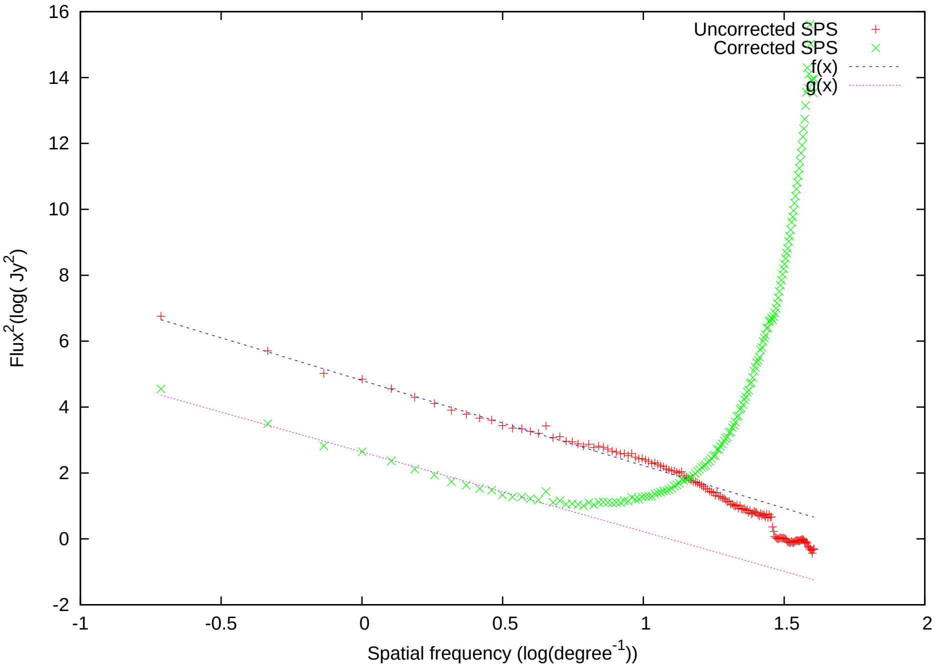

Fig. 8.57: *A comparison of the SPS for the corrected and uncorrected maps for a velocity width of 0.7km* s^{-1} *at* υ_{lsr} *=48km* s^{-1}*. Red dots are the uncorrected SPS while green dots are the corrected SPS. The red line is a fit to the former while the blue line is the fit to the later. The figure covers spatial scales from* 10° *down to* $1.8'$

9 Discussion

9.1 Introduction

In Chap. 3 I have discussed the determination of the observational and physical quantities for the HI clumps. In order to measure these, a number of assumptions are needed which impose uncertainties in the determination of the parameters. In this chapter I will discuss the importance of errors in the different measurements. A comparison of various Galactic models used for the distance estimates will show that the uncertainties in the distance determination greatly affect the results. Finally I will present a simple simulation which can correlate the observational parameters of the HI clumps with the Galactic fountain mechanism to answer the question if there is a connection between the two phenomena.

9.2 Measurements and errors

In Chap. 2.6, I have discussed how to calculate the physical parameters of the clumps from observational measurements taken using a radio-telescope. Therefore I can estimate a range of parameters to describe the physical conditions in the neutral Galactic halo and in the clumps themselves. After calculating the physical quantities, it is important to estimate the errors introduced during the measurement of the observational parameters. Applying a simple error propagation, assuming always that the spectrum of the HI clumps can be described by a Gaussian, I find the following formulas for the errors of each measure quantities:

$$\Delta T_{kin} = 2 \cdot \delta \upsilon_{width}$$

where ΔT_{kin} is the percentage error of the T_{kin} and $\delta \upsilon_{width}$ is the percentage error of the $\Delta \upsilon_{1/2}$,

for the linear size of the clumps D:

$$\Delta D = \sqrt{(\Delta s)^2 + (\delta d)^2}$$

where ΔD is the percentage error of the linear size of the clump, Δs is the percentage error of the angular size of the clump and δd is the error in the distance determination.

For the column density of the clumps N_{HI}

$$\Delta N_{Hi} = \sqrt{(\Delta T_B)^2 + (\delta \upsilon_{width})^2}$$

where ΔT_B is the percentage error in the brightness temperature T_B ,

for the average volume density $< n >$

$$\Delta N_{Hi} \; = \sqrt{(\Delta T_B)^2 + (\delta \upsilon_{width})^2 + (\delta s)^2 + (\Delta d)^2}$$

and finally for the pressure P/k

$$\Delta N_{Hi} \; = \sqrt{(\Delta T_B)^2 + 3 \cdot (\delta \upsilon_{width})^2 + (\delta s)^2 + (\Delta d)^2}$$

.

In my observations using the 100-m Effelsberg and the 300-m Arecibo Radio-telescope, the calibration errors of measurement of the T_B are in the range of 1%-2%. In the determination of the $\Delta\upsilon_{1/2}$ in the spectra of the H I clumps, I consider the error to be equal to the channel separation. Assuming that there is no uncertainty in the distance determination and in the determination of the size of the clumps then using the formulas above, the error in the estimate of the physical values should not be greater than 10% on average. I have to note that in the case of the Arecibo observations, as discussed in Chap. 5 the baseline correction introduces some uncertainty to low T_B spectra, furthermore the spectra are not corrected for stray radiation. From the comparison of the LAB and Arecibo spectra these effects seem to be minimal, still they slightly increase the error in the determination of the physical parameters. The error contribution from the measurements is not greater than 5%

In the case of the VLA and WSRT observations, it is more difficult to ascertain the error in the physical quantities. While the errors introduced through the calibration process are again of the order of 2%, it is difficult to weight the effect of the CLEAN processes in the measurement. A comparison between the fluxes for different cut-off levels of the CLEAN algorithm indicates a reasonable estimate of the uncertainty of the physical values of the order of 20%.

The error estimates above do not take into account the uncertainties introduce by the distance determination. This is the more serious reason for an increased uncertainty in the physical parameters. As it will be explained in the next subsection, the determination of the distance through kinematical estimates is the most secure method to follow in the outer part of the Galaxy. Still it has two serious drawbacks. I have to assume that the H I clumps follow closely the Galactic rotation, deviations from it can introduce an unknown uncertainty in the determination of the distance. Since as explained in Chap. 1 the clumps are part of the Galactic halo this assumption seems to be valid. More importantly as seen in the next section from a comparison between distances estimated using different Galactic velocity field models, the uncertainty in the determination of the distance ranges from 6% up to 36%. The errors introduced by calibration etc, as described earlier, have a minor effect in the accuracy of the determination of the derived physical parameters, so the uncertainty in the distance plays the dominant role.

	Model 1 d(kpc)	Model 2 d(kpc)	Deviation %	Model 3 d(kpc)	Deviation %
113.33+27.00-40.5	4.0	4.9	22.5	5.2	30.0
116.20+23.55-68.0	7.0	8.2	17.1	8.7	24.3
114.71+29.60-89.5	11.0	14.0	27.3	15.0	36.3
217.50+15.16+78.4	13.5	14.7	8.8	16.0	15.6
216.57+18.40+32.8	3.5	3.7	5.7	4.0	14.28

Tab. 9.21: *A table of comparison between derived distances from different model for a random selection of clumps. a) Model 1: Kalberla (2003) b) Model 2:* $v_{rot} = 220 km\, s^{-1}$*, co-rotation c) Model 3: Brand & Blitz (1993)*

9.3 Distance determination

In Chap. 1, I have discussed the three different methods to determine the distance. As seen in the previous subsection 9.2, the uncertainty in the distance determination affects greatly the estimates for all the other different parameters of the clumps. The determination of distances using the terminal velocity is the most accurate method, depending only on the knowledge of the rotation curve but unfortunately this is applicable only in the inner part of the Galaxy. The standard method for determining the distance kinematically, as applied in this work, depends on the assumption of the Galactic velocity field but has the advantage that it can be applied also to the outer parts of the Galaxy. In my work I used the velocity field described in Kalberla (2003). To weight the uncertainty introduced to the distance determination using this method, I compared for a random selection of clumps the distances as estimated using a) the aforemention velocity field (model 1), b) a velocity field assuming a constant rotation velocity of 220km s^{-1}outside the solar radius and co-rotation with increasing z-height, c) a velocity field assuming a Brand & Blitz rotation curve (Brand & Blitz, 1993), d) and a velocity field model by Gómez (2006). For the last model the distance of the sun from the center is assumed to be 8kpc and the velocity field is given only for b=0°, so in order to do the comparison I estimated distances for b=0°in the model 1 and I scaled the distance result to correspond to R_o=8kpc.

In Table 9.21, I show the derived distances from different models. The Bonn model, in comparison with the model 2, has a deviation in the distance estimate ranging from 6% up to 22% depending on the position. This deviation can be attributed to the difference between the lagging halo of the Bonn model and the co-rotating halo of model 2. In case of the Brand&Blitz rotation curve the deviation is higher, ranging from 15% up to 36%.

In Table 9.22, I compare the Bonn model with the model of Gómez (2006). Since he uses R_o=8 kpc while our model has R_o=8.5 kpc, I scaled up his distance estimates by a ratio of 1.06. As seen from the table in comparison to the Bonn model the Gómez

	Model 1 d(kpc)	Model 4 d(kpc)	Deviation %
113.33+0-40.5	3.9	3.4	-12.82
116.20+0-68.0	6.7	6.3	-6.97
114.71+0-89.5	9.6	8.68	-9.58
216.57+0+32.8	3.2	2.74	-14.37

Tab. 9.22: *A table of comparisons between derived distances from different models for a random selection of clumps. a) Model 1: Kalberla (2003) b) Model 4: Gómez (2006)*

(2006) model gives smaller distances, deviating from 7% up to 15% percent, affecting the size of the clumps in a similar way. The Brand & Blitz (1993) model is the standard model to use for the kinematical distances in Milky Way, so I used it to define the distance uncertainty in the clumps.

Despite the uncertainty of the kinematical method to determine clump distances, it can provide us with enough information to confine the physical properties of the clumps within a small range while at the same time making only a minimal assumption about their properties. Other methods, such as estimating distances using pressure, yield far greater uncertainties. In order to ascertain this, I have estimate the distance of the clumps at 219.39+18.53 with a velocity of 38.6 $\mathrm{km\,s^{-1}}$ using pressure considerations. I used the model for thermal equilibrium between the cold and the warm neutral phase as described by Wolfire et al. (2003). In order to use this model I have to assume that the gas in the Galactic Halo has similar metalicity and dust-to-gas ratio with the disk, with a FUV field of similar strength. Also this assumption assumes that the photo-electric heating and the cooling through the heavy elements, are the dominant mechanism in the halo neutral gas. Following Stanimirović et al. (2006), the volume density $<n>$ is given by $n \sim N_{HI} \cdot D$ where D is the diameter of the clump equal with $D = s \cdot d$ the angular size of the clump in rads times the distance of the clump. The pressure of the clump is given as $P \sim n \cdot T$. Therefore I conclude that $N_{HI}/s = n \cdot d$ and thus $P \cdot d = N_{HI} \cdot T/s$. The clump 219.39+18.53 has a column density of $50.51 \cdot 10^{18}$ cm^{-2}, an angular size s of $5.26'$and a kinetic temperature T_{kin}=388 K. Using the formulas above, the product $n \cdot d$ equals $10.7\mathrm{cm}^{-3}$kpc, and the product $P \cdot d$ equals 4158 Kcm^{-3}kpc. This calculation assumes spherical symmetry of the cloud. From Table 3 in Wolfire et al. (2003), the range of pressure where thermal equilibrium is possible in different Galactocentric distances, varies between a low and a high value. For the solar neighborhood the range of pressures where thermal equilibrium between the CNM and WNM phase is possible, is from $1960\mathrm{Kcm}^{-3}$ to $4810\mathrm{Kcm}^{-3}$. Assuming the clumps are located close-by using the product $P \cdot d$ implies a distance of the clump in the range 0.864kpc to 2.1kpc and a size from 1.32pc up to 3.2pc. For a Galactocentric distance of 11kpc the range of allowed pressures is 995 Kcm^{-3} to 2420 Kcm^{-3}, in this case the clump would have a distance within the range of 1.7 kpc up to 4 kpc implying a size from 2.6 pc up to 6 pc. As seen even for a specific Galactocentric radius the uncertainty in the distance estimate is very high using the pressure considerations. More importantly there is no physical reason to give a preference to one Galactocentric radius R over another one, since the clumps can reside at any distance from 8.5 kpc up to 18 kpc according to the calculations of Wolfire et al. (2003). Therefore this method can be used only to give an initial estimate as used in Stanimirović et al. (2006) for a region close to the anti-center. Despite the uncertainties, the kinematical determination is the best method to estimate the distance of the clumps in the outer parts of the Galaxy.

9.4 Galactic fountain

Lockman (2002) proposed that the HI clumps are formed as a result of the Galactic fountain mechanism. This implies that this phenomenon plays an important role in the creation and maintenance of the Galactic gaseous halo. First formulated in Shapiro & Field (1976) as a mechanism to explain the presence of a Galactic hot corona, it was suggested by Bregman (1980) as a possible origin for the HVC's. It is a mechanism which continually feeds gas to the Galactic Halo. According to these two papers which outline the principals of a Galactic fountain mechanism, a hot gaseous bubble produced by a supernova explosions streams upwards through the cooler gas of the disk due to buoyancy. The velocity of a bubble perpendicular to the plane υ_z is smaller or equal with the sound speed c which is estimated to be c=170 km s^{-1}(Shapiro & Field, 1976) or 130 km s^{-1}(Kahn, 1981). Depending on the efficiency of the cooling mechanism of the bubble (mainly radiative) and thus the cooling time t_c the possible outcome for the bubble can be one of the following two: a) if the radiative mechanism is inefficient and the t_c is large then the bubble expands adiabatically and ends up in a layer of gas with similar temperature and density, exerting pressure on the gas beneath and forming a corona in hydrostatic equilibrium, b) if the radiative cooling is efficient and the t_c is sufficiently small, then before reaching great heights, the bubble undergoes a phase transition, cools, becomes denser and looses its buoyancy. At this stage the formed cool cloud follows a ballistic motion, with initial $\upsilon_z \sim c$, bringing them back to the plane. It is proposed that the HI clumps constitute exactly this late stage of the Galactic fountain mechanism where the cool clumps move under the Galactic gravitational field towards the plane. While it is difficult to observe the initial hot phase of the Galactic fountain, it is fairly easy to observe the late phase in the form of HI clumps.

In order to test the possibility for our HI clumps to be the late stage results of a Galactic fountain, I performed a simple ballistic simulation under the Galactic gravitational field in order to compare the expected observational properties of a Galactic fountain HI clump with the properties of our clumps as measured with radio-telescopes. The quantity to compare is the line-of-sight velocity υ_{lsr} . The code describes the motion of a test particle under the gravitational field of the Milky Way with an initial velocity υ_z perpendicular to the plane. Thus it simulates in a simple way the motion of an

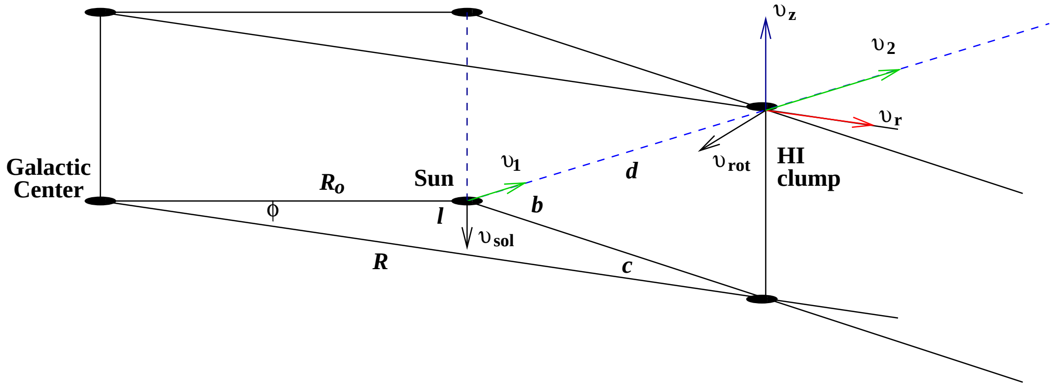

Fig. 9.58: *A plot showing an* HI *clump undergoing a ballistic orbit at a specific time t of it orbit in reference with the sun and the Galactic center.*

HI clump just formed from a hot gas bubble. The initial parameters are the starting position given in Galactocentric radius R and height z, the velocity of the upward motion υ_z and the time range. The gravitational field under which the motion takes place is described in Kalberla et al. (2007). I also assumed that the angular momentum is conserved and that there is no drag force applied to the test particle. The last assumption may be important in high ejection velocities since $F \sim \upsilon^2$, but to maintain simplicity it was not implemented in the code. The code gives the motion of the test particle as a function of time. As an output I get the Galactocentric radius $R(t)$, the height $z(t)$, the velocity perpendicular to the plane $\upsilon_z(t)$, the rotational velocity $\upsilon_{rot}(t)$ and the velocity with a radial direction $\upsilon_r(t)$. I have used as a starting location different random positions along the Galactocentric radius R and z, for the initial velocity υ_z I assume that $\upsilon_z = c$ and I used the values of 130 $\mathrm{km\,s^{-1}}$ and 170 $\mathrm{km\,s^{-1}}$ as described earlier. For the time limit I let the simulation run for 4 Gyrs, but I limited the orbit up to a position when the test particle returns to the plane again.

The aim of the simulation is to compare it with the observational data. For my samples of HI clumps in the Galactic halo, the longitude l, the latitude b and the υ_{lsr} is known. As described earlier I have determined kinematically the distance, so also the R and z is known. I used this initial R and z value and I selected the simulation result with the given similar position. From the resulting $\upsilon_{rot}(t)$, $\upsilon_r(t)$ and $\upsilon_z(t)$ I have calculated the expected line of sight velocity $\upsilon_{lsr\ m}$ with the help of Fig. 9.58

In this figure ϕ is the Galactocentric azimuth, υ_{sol} is the rotational velocity in the position of the sun equal with 220 $\mathrm{km\,s^{-1}}$.

The $\upsilon_{lsr\ m}$ is then given by the following equation:

$$\upsilon_m = \upsilon_z \cdot sin(b) + \upsilon_{rot} \cdot sin(c) \cdot cos(b) + \upsilon_r \cdot \cos(c) \cdot cos(b) - \upsilon_{sol} \cdot sin(l) \cdot cos(b) \quad (9.11)$$

This is the line-of-sight velocity $\upsilon_{lsr\ m}$ one would expect if the clump was caused by a

Galactic fountain, and is moving in a ballistic orbit. So finally I compare the expected line-of-sight velocity $\upsilon_{lsr\ m}$ with the observed line-of-sight velocity υ_{lsr} . We would expected this to be similar if the observed clump was ejected by the Galactic fountain mechanism.

I run the simple simulation for 32 HI clumps of the sample, assembled from the Arecibo and Effelsberg observations. First of all I assumed that the HI clumps follow a ballistic orbit towards the Galactic plane. Upon reaching the dense Galactic disk the HI clump cannot continue its orbit and becomes part of the galactic disk material again. The initial parameters for each HI clump were the same: **a)** The Galactocentric radius ranged from 5 kpc up to 13 kpc with a step of 1 kpc, **b)** the heights z from the plane are 0kpc, 0.5kpc, 1kpc, 3kpc, 5kpc, 7kpc, **c)** the initial velocity υ_z is less than the sound speed c at 90 $\mathrm{km\,s^{-1}}$ and 100 $\mathrm{km\,s^{-1}}$, at the sound speed at 130 $\mathrm{km\,s^{-1}}$ and 170 $\mathrm{km\,s^{-1}}$(Shapiro & Field, 1976; Kahn, 1981), slightly more than c at 200 $\mathrm{km\,s^{-1}}$. For each of the clumps I run a series of simulations for all the combination of initial parameters. In each run I compared the position of the HI clumps R_c,z_c in Galactocentric coordinates with the R and z as calculated from the simulation. If $|R_c - R| < 0.5$ kpc and $|z_c - z| < 0.5$ kpc I considered that the position of the clump coincides with one of the position of the orbits. The limit of 0.5 kpc takes into account the uncertainty for the determination of the distance. Once I found a match for the clump position, I then used the equation 9.11 to determine the expected line-of-sight velocity $\upsilon_{lsr\ m}$ according to the model. Its was then compared with the measured υ_{lsr} from the observations of the HI clumps. If the deviation is smaller than 10% I assumed there is also a match in line of sight velocity and that the observed HI clumps can be a result of a Galactic fountain flow, if the difference is greater than 10% I considered that there is low probability for the observed HI clumps to be associated with a galactic fountain flow.

For 16 of the 31 HI clumps tested, the simulation failed to reproduce the position and velocity requirements, only when I used unphysical values for the starting velocity, for example $\upsilon_z = 400$ $\mathrm{km\,s^{-1}}$, did I manage to match the observational values with the simulations. It is interesting to note that this sample is composed entirely from the Arecibo sample. As seen also from the Arecibo observations, the maps presented in the section 6 are more similar with clumps resembling to be a result of turbulence than Galactic fountain flows.

For the remaining 15 HI clumps the simulations produced positions where I found a close match between the expected line-of-sight velocity $\upsilon_{lsr\ m}$ and the measured υ_{lsr} velocity for the clump in a given position. This implies that it is possible for a product of a Galactic fountain to have similar velocities with the ones observed in the HI clumps. In the Table. 9.23 I give the observational values for each clump and the results of the ballistic simulations. In each clump there were more than one initial set of parameters for which the simulation match the observation. So for each position I give all of the results.

In all the cases the time it takes for the particle to reach from its initial position to the plane is around 100Myrs. As can be seen from the table the initial speed υ_z is a lot less than the sound speed in most of the cases, being either 90 km s^{-1} or 100 km s^{-1}. υ_c gives the motion of the particles in a direction perpendicular to the plane while t_{cr} is the time passed from the initial position R_st and z_st. As seen in the Table 9.23, in most cases υ_c<0 and t_{cr} is close to 100 Myrs. I infer that it is more probable to detect the HI clumps at the end of their ballistic orbits. Some have υ_c>0 and the t_{orb} is very small showing that we expect to detect the HI clump in the beginning of their orbits. Another important initial parameter which can help us is the initial position in the z axis. While I also used as a starting parameters higher z heights, the initial parameter that yielded the matching results range from z=0kpc to z=1kpc above the place. Assuming that the supernova explosion happens in the Galactic plane and that the hot gas rises with a velocity $\sim$ 100 km s^{-1} (also the starting velocity) it then takes approximately 10 Myrs to reach a height of 1kpc. In this time the hot gas has to cool and form a cold clump at z=1 kpc a cold clump which will then follow a ballistic orbit. Then the cooling time of the hot gas t_c should be of the order of 10 Myrs. This solution is very similar to the ones proposed in (Shapiro & Field, 1976) although the initial velocity is smaller than the proposed speed of sound. As a result of the simulations, the possibility exists that one of the mechanisms to create HI clumps in the Halo is the Galactic fountain. Of course we should not neglect the fact that the HI clumps observed with Arecibo failed to be reproduced by the simulations and that they show evidence for a turbulent nature of the Galactic neutral gas.

9.5 Comparison with the CNM phase:Clumps or sheets

Heiles & Troland (2003b) conducted a 21-cm absorption line survey using the Arecibo 300-m radio telescope in order to study the properties of the warm (WNM) and the cold neutral media (CNM) in the Galactic disk. The authors studied a number of regions in the solar neighborhood and analyzed a number of HI CNM clouds measuring spin temperatures T_s and column densities. Using additional measurements of the CNM pressure from CI line observations, the authors determined the line-of-sight size of the clouds for two regions, the “Triad Region” and the “Small Region of Heiles (1967)”. Measuring the apparent size of the clouds they were able to estimate the ratio r of length-to-thickness which was found to be 280 and 70 for the two regions respectively. Therefore they presented observational evidence towards the isotropic morphology of the CNM clouds. In connection with this result they discussed two descriptive models for the morphology of the CNM: **a)** the popular “raisin pudding” model which assumes that a large number (10^4) of isotropic CNM clouds are embedded in a WNM component in a random fashion and **b)** the “Clumpy CNM Sheet” model in which the WNM extends over large volumes with the CNM laying inside. The CNM is organized into a few large thin structures (up to hundreds of pc as estimated above). According to Heiles & Troland (2003b) the sheets contain a lot of CNM blobs, with an estimated density for one of their region of 1 cloudlet per 30pc^2. Heiles & Troland (2003b) find

	R_c kpc	z_c kpc	υ_{lsr} km s^{-1}	R_m kpc	z_m kpc	V_z km s^{-1}	V_m km s^{-1}	R_{st} kpc	z_{st} kpc	V_{zst} km s^{-1}	t_{orb} Myrs
113.33+27.00	10.5	1.8	-40.5	10.6	2.7	-34.7	-40.5	10	0	90	60
113.33+27.00	10.5	1.8	-40.5	10.6	2.3	-40.2	-44.6	10	1	90	57
113.33+27.00	10.5	1.8	-40.5	10.9	1.6	65.3	-40.6	11	0	90	20
113.33+27.00	10.5	1.8	-40.5	11.0	1.5	116.9	-38.3	11	1	130	11
113.16+25.49	10.0	1.4	-32.5	9.6	1.7	-49.4	-32.5	9	0	90	59
113.16+25.49	10.0	1.4	-32.5	9.7	1.8	-50.4	-33.4	9	0.5	90	55
113.16+25.49	10.0	1.4	-32.5	10.0	0.9	80.5	-32.4	10	0	90	10
113.16+25.49	10.0	1.4	-32.5	10.0	0.9	83.8	-29.6	10	0.5	90	4
116.20+23.55	12.7	2.8	-68.0	12.5	3.2	-71.7	-67.8	11	0	130	83
116.20+23.55	12.7	2.8	-68.0	12.5	3.3	-77.0	-68.6	11	3	90	59
116.20+23.55	12.7	2.8	-68.0	12.4	2.5	-39.6	-67.9	12	0	90	73
116.20+23.55	12.7	2.8	-68.0	12.7	2.8	-47.8	-68.0	12	0	100	78
116.20+23.55	12.7	2.8	-68.0	12.7	2.8	-39.2	-67.9	12	0.5	90	70
116.20+23.55	12.7	2.8	-68.0	12.9	3.1	-46.8	-68.1	12	0.5	100	73
116.20+23.55	12.7	2.8	-68.0	12.8	2.9	-43.5	-67.8	12	1	90	66
116.20+23.55	12.7	2.8	-68.0	13.0	3.2	-49.7	-68.0	12	1	100	70
116.33+22.80	14.3	3.5	-81.5	13.8	3.9	-99.2	-90.3	11	3	130	78
116.33+22.80	14.3	3.5	-81.5	13.9	3.7	-73.5	-81.7	12	0.5	130	89
116.33+22.80	14.3	3.5	-81.5	13.9	3.9	-74.5	-81.4	12	1	130	86
116.33+22.80	14.3	3.5	-81.5	13.8	3.6	-80.00	-82.7	12	3	100	71
116.33+22.80	14.3	3.5	-81.5	14.7	4.0	-69.9	-85.4	13	0	130	98
116.33+22.80	14.3	3.5	-81.5	14.0	3.3	-48.7	-81.6	13	0.5	100	81
116.33+22.80	14.3	3.5	-81.5	13.8	3.1	-43.9	-81.6	13	1	90	73
116.33+22.80	14.3	3.5	-81.5	14.4	3.8	-65.5	-81.3	13	3	90	69
116.50+21.45	10.7	1.5	-42.5	10.7	1.9	-51.0	-42.3	10	0	90	67
116.50+21.45	10.7	1.5	-42.5	11.0	1.1	164.1	-43.2	11	0	170	6
116.50+21.45	10.7	1.5	-42.5	11.0	1.2	91.1	-41.8	11	0.5	100	7
116.50+21.45	10.7	1.5	-42.5	11.0	1.2	86.3	-42.6	11	1	90	3
116.50+21.45	10.7	1.5	-42.5	11.0	1.1	128.3	-40.8	11	1	130	12
115.00+24.00	14.5	3.9	-84.5	14.0	4.4	-94.7	-91.7	11	0	170	97
115.00+24.00	14.5	3.9	-84.5	14.0	3.7	-77.8	-91.0	12	1	130	88
115.00+24.00	14.5	3.9	-84.5	14.8	4.4	-63.9	-85.2	13	0.5	130	93
115.00+24.00	14.5	3.9	-84.5	14.6	4.2	-66.3	-83.9	13	4	100	72
115.35+22.35	12.3	2.5	-66.5	11.9	3.0	-84.1	-71.4	10	1	130	74
115.35+22.35	12.3	2.5	-66.5	11.9	3.0	-93.8	-72.4	10	3	100	61
115.35+22.35	12.3	2.5	-66.5	12.0	2.4	-61.4	-68.9	11	0.5	100	73
115.35+22.35	12.3	2.5	-66.5	12.4	2.5	-41.1	-66.5	12	0.5	90	74

Tab. 9.23: *A table with the results of the simulation for each* H I *clump. The first four columns give the measured parameters of the clumps: the coordinates, the Galactocentric radius* R_c*, the height* z_c*, and the line-of-sight velocity* υ_{lsr} *. The last eight parameters come from the simulation: the Galactocentric radius at the end of the tranjectory* R_m*, the height* z_m*, the velocity perpendicular to the plane* V_z*, the line-of-sight velocity for the simulation* V_m*, the initial radius* R_{st}*, height* z_{st}*, velocity* V_{zst} *and the time of the orbit* t_{orb}*.*

	R_c kpc	z_c kpc	υ_{lsr} km s^{-1}	R_m kpc	z_m kpc	V_z km s^{-1}	V_m km s^{-1}	R_{st} kpc	z_{st} kpc	V_{zst} km s^{-1}	t_{orb} Myrs
117.32+24.00	13.1	3.0	-71.4	12.7	3.4	-73.4	-72.1	11	1	130	81
117.32+24.00	13.1	3.0	-71.4	12.7	3.5	-81.1	-71.5	11	3	100	63
117.32+24.00	13.1	3.0	-71.4	12.9	3.0	-49.8	-71.3	12	0.5	100	75
117.32+24.00	13.1	3.0	-71.4	13.0	3.1	-53.0	-71.5	12	1	100	72
118.01+24.59	13.2	3.1	-71.0	12.8	3.6	-73.6	-71.1	11	1	130	77
118.01+24.59	13.2	3.1	-71.0	12.9	3.0	-48.5	-70.6	12	0.5	100	74
118.01+24.59	13.2	3.1	-71.0	13.0	3.1	-51.8	-71.0	12	1	100	71
118.01+24.59	13.2	3.1	-71.0	13.3	3.0	-26.0	-71.0	13	0	90	73
117.97+24.00	13.1	3.1	-72.3	12.8	3.5	-75.5	-72.0	11	1	130	78
117.97+24.00	13.1	3.1	-72.3	12.8	3.4	-82.5	-72.1	11	3	100	64
117.97+24.00	13.1	3.1	-72.3	12.9	3.0	-51.0	-72.0	12	0.5	100	75
117.97+24.00	13.1	3.1	-72.3	13.0	3.1	-54.5	-72.4	12	1	100	73
117.97+24.00	13.1	3.1	-72.3	13.4	2.9	-29.6	-72.4	13	1	90	74
117.51+25.19	13.1	3.0	-74.0	12.9	3.4	-76.8	-77.0	11	1	130	79
117.51+25.19	13.1	3.0	-74.0	12.7	3.5	-81.1	-73.9	11	3	100	63
117.51+25.19	13.1	3.0	-74.0	12.9	3.0	-48.5	-73.7	12	0.5	100	74
117.51+25.19	13.1	3.0	-74.0	13.0	3.1	-52.2	-74.2	12	1	100	71
117.51+25.19	13.1	3.0	-74.0	13.3	3.0	-25.2	-73.8	13	0	90	73
113.32+21.74	13.4	3.0	-75.3	12.9	3.4	-80.0	-79.6	11	1	130	81
113.32+21.74	13.4	3.0	-75.3	13.0	2.9	-53.8	-75.2	12	0.5	100	77
113.32+21.74	13.4	3.0	-75.3	13.5	3.5	-72.7	-78.0	12	1	130	65
113.32+21.74	13.4	3.0	-75.3	13.4	2.9	-34.6	-75.3	13	0	90	77
112.10+27.79	10.4	1.8	-39.5	10.5	2.3	-32.3	-41.0	10	0	90	60
113.84+28.70	12.6	3.6	-69.4	12.5	3.8	-58.1	-69.6	11	0.5	130	75
113.84+28.70	12.6	3.6	-69.4	12.5	3.9	-66.1	-69.4	11	3	100	57
113.84+28.70	12.6	3.6	-69.4	12.7	3.4	-31.1	-69.4	12	0.5	100	66
113.84+28.70	12.6	3.6	-69.4	12.8	3.5	-34.6	-69.4	12	1	100	64
112.45+29.90	12.5	3.7	-65.5	12.2	3.7	-53.4	-65.4	11	0	130	75
112.45+29.90	12.5	3.7	-65.5	12.4	4.1	-58.8	-65.5	11	3	100	54
112.45+29.90	12.5	3.7	-65.5	12.6	3.5	-21.9	-65.3	12	0.5	100	62
112.45+29.90	12.5	3.7	-65.5	12.7	3.6	-25.8	-65.3	12	1	100	60

Tab. 9.24: *A table with the results of the simulation for each* H I *clump. The first four columns give the measured parameters of the clumps: the coordinates, the Galactocentric radius* R_c*, the height* z_c*, and the line-of-sight velocity* υ_{lsr} *. The last eight parameters come from the simulation: the Galactocentric radius at the end of the tranjectory* R_m*, the height* z_m*, the velocity perpendicular to the plane* V_z*, the line-of-sight velocity for the simulation* V_m*, the initial radius* R_{st}*, height* z_{st}*, velocity* V_{zst} *and the time of the orbit* t_{orb}*.*

that the second model is more consistent, not only with their observational findings of the sheet-like CNM, but also with the idea that CNM is produced from large-scale shocks.

My observations of the HI clumps of the Galactic halo show a number of similarities with the above description of the interstellar CNM. For most of the spectra the halo HI clumps show very narrow line-widths, implying association with a cold phase. The column densities in my sample and in Heiles & Troland (2003b) for the CNM are of the order of $10^{19}\mathrm{cm}^{-2}$. Also the morphology of the observations prove to be similar. Using the Effelsberg telescope we found low densities of clumps which can be associated with the large CNM clouds while the interferometry observations showed that the clumps are resolved into a large number of cores, which are similar to the cloudlets mentioned above. The Arecibo observations which mapped a large area also show the presence of colder denser structures embedded in the extended broad component. Therefore the morphology found in all our 21-cm observations is consistent with the picture of a “Clumpy CNM Sheet” model. So the question logically arises, does the HI halo clump population exhibit a similar sheet-like morphology as the CNM?

Up to now, to derive the physical parameters of my sample I have considered that the objects have a cylindrical morphology, where their apparent length s is equal to the width H. It is a fair assumption in order to derive the physical parameters due to the lack of other independent observations. The clumps are certainly not spherical, which is evident even by their apparent profiles. In the case of the HI cores detected with the VLA and WSRT, but also the large clumps from Effelsberg and Arecibo, there appears to be an elliptical rather than a spherical profile. This leads to some deviations within the errors of the derived physical quantities. On the other hand, if the HI clumps and therefore the HI cores really have a sheet-like morphology, this would have serious implication for their properties. In this case I would have possibly underestimated their volume densities and pressures by a factor which is given by the length-to-thickness ratio r. This would imply that the clumps would move further up in the phase diagrams of Chap. 8, right towards the cold branch of the diagrams.

A clump has a diameter D and a width H. At a specific distance d it has angular diameter s and angular width h. The length-to-thickness ratio is defined as $r = s/h$. Typical cases are:

- $r = 1$. In this case the clump is cylindrical and this is the assumption used in this work.

- $r = 10$, a moderate value for r which would imply thermal and pressure equilibrium in the phase diagram. For example the Arecibo sample would then have a mean volume density of 19 cm^{-3} which would place the sample well within the stable region of the CNM in the phase diagrams.

- $r = 70$, an extreme case, with the value for the ratio taken unmodified from Heiles & Troland (2003b). This implies in the case of the Arecibo sample a volume density for the clumps approximately of 130 cm^{-3}, denser than the one allowed for CNM in thermal equilibrium with a clump pressure higher than the pressure of its warm envelope.

We assume that we have a population of n HI clumps with similar diameters D which are located at the same distance from the Sun. For the case with $r > 1$ there is not a preferable orientation of the clumps towards our line of sight. The apparent diameter of the clumps ranges from s when viewed face on down to h when viewed edge on. When observed with a telescope of beam width θ there are three possible outcomes:

- The telescope resolution is sufficiently high, $\theta < h$. In this case the telescope detects all clouds of the sample. In case of a cylindrical morphology all the apparent diameters of the clumps should be identical. In case of the sheet like morphology the apparent diameter should range from s down to h. Therefore the ratio of the highest apparent diameter to the lowest one should be 10(for r=10) or 70(for r=70)
- For observations with insufficient resolution($\theta > s$), the measured apparent diameter would be almost identical for all cases, independent of the cylindrical or sheet like morphology. In the second case a selection effect would be introduced since mostly edge on clump would be detected. In any case, we would not be able to differentiate between the morphology of the clumps.
- In case of a telescope with resolution $s > \theta > h$ we would measure for the cylindrical morphology identical apparent diameters. For the sheet like morphology the telescope would detect all clumps with an apparent diameter from s approximately down to the beam size of θ. From the observational point of view, since we don't know the actual number of clumps, we are unable to discern between the different length-to-thickness ratios. A spread in the values could indicate a sheet-like structures.

A re-examination of the various telescope samples under this analysis can provide us with hints to the morphology of the HI clumps. So for each telescope sample I will compare the apparent diameters of the HI clumps located at the same distance, in order to test the above analysis. For the Effelsberg sample, the resolution is too crude, as shown from the synthesis telescope observations, to discern something about the morphology of the clumps. Sheet-like or blob-like clumps provide the same results. In the Arecibo sample, I compare from Table. 6.14-6.15 the apparent diameter s of 11 clumps which are located at a distance $\sim$ 4kpc. The minimum width measured is $4'$ which is very close to the resolution of the Arecibo telescope. So any spread in the apparent diameter values cannot be attributed to a sheet like structure. It is actually more likely that we talk about clumps of similar diameters. The samples detected with the synthesis observations have apparent diameters which do not vary significantly. In this case the cores have most probably non sheet-like morphology. Since they are part of the same region it is also probable that they have the same orientation, so their apparent diameter is the same. It is also worth to apply the same analysis for the Stil et al. (2006) sample. Using table 1 and table 3 from Stil et al. (2006) I compared the measured angular diameters for the clumps with distance $\sim$ 7 kpc. In this sample the measured angular diameters range from $2'$up to $5\,'$. So, similarly to our synthesis observations, the range of the observed apparent diameter is fairly small. All in all, from all the above samples, there is no clear indication for a dominant sheet-like nature of clumps with length-to-width ratio of the order of 70. As it is evidence from the observations, the clumps are asymmetric and show very narrow line-widths, with a mean line width from 3.3 $\mathrm{km\,s^{-1}}$to 5.3 $\mathrm{km\,s^{-1}}$. As discussed earlier in this section, pure thermal equilibrium considerations show that a more “cloudy” structure with low to moderate length-to-width ratios is more probable than a true sheet like structure with ratios of the order of 70. In addition, a sheet-like filamentary structure of the clumps would imply that the turbulence is dominant in scales comparable with the size of the clumps. This contradicts the very narrow line widths found in the Effelsberg and Arecibo data which show that the role of turbulence is not significant. This is also supported by the study of turbulence in the Arecibo map (Chap. 8). While the end of the inertial range is $\sim 14'$, the mean size of the clumps is $6'$, so while turbulence is importance for the transfer of energy from larger scale to the smaller scale and the spatial redistribution of gas, it plays a smaller role in the scales of the clumps size. Neither the line widths nor the turbulence study point to a sheet-like structure of the clumps. To learn more about the morphology and length-to-width ratio of the clumps, it will be useful to apply an analysis based on this section to a larger, more complete, sample of HI halo clumps.

10 Conclusions

The aim of my thesis was to study the nature of the neutral gaseous component in the Galactic halo. The research was focused on Galactic halo sub-structure of the neutral gas in the form of small clumps, first detected in the inner Galaxy by Lockman (2002). My target was not to conduct a full sky survey of all clumps but to assemble a sample of them primarily located outside the solar circle. In the first part of my project I used the 100-m Effelsberg Radio telescope (Chap. 4). Follow-up observations were done using two interferometer arrays, the Westerbork Synthesis Radio Telescope and the Very Large Array (Chap. 5). In the last part of my project I utilized the new 7 beam ALFA multi-beam receiver installed at the 300-m Arecibo telescope to observe a larger area in the sky (Chap. 6). The physical parameters of the clumps were estimated from the observational measurements, in order to study the more general properties of the neutral gaseous Halo. For this estimation, the distance of the clumps from the Sun needs to be determined. This was done using the Bonn Mass Model (Kalberla et al., 2007). As a side project the possibility to include spiral arms in the Mass Model and the effects on the morphology of the brightness temperature distribution maps were tested (Chap. 3). In the following paragraphs I will give a summary of the results of my projects.

Based on the method in Burton (1971), I have modeled the Galactic spiral structure using the linear density wave theory. This approach considers that the spiral arms can be described by a grand design and induce a velocity perturbation in the velocity field of the Milky Way. In combination with the Bonn Milky Way mass model (Kalberla, 2003), the spiral arms were modeled using the linear density wave theory and were described by their inclination angle i, the number of spirals arms m, the surface density contrast between the arm and inter-arm region and the angular pattern speed Ω_p. A comparison between synthetic data cubes of the models and the real data from the all sky HI LAB survey was done. Despite using a simple model I was able to produce synthetic data cubes with morphologies similar to the real spiral structure, even reproducing the exact location of spiral features in some cases. Therefore it is evident that a more refined model based on the density wave theory can be used to introduce spiral structure in Galactic models. It is important to note that the density wave theory describes **only** Grand design spiral structure while as seen in galaxy catalogs (Sandage, 1961) only a small percentage of all the the spiral galaxies exhibits such a morphology. A more important result is that, independent of the density wave theory, kinematic irregularities and not densities fluctuations are the cause of the apparent spiral structure in the all sky HI surveys. Therefore interpretation of studies such as Levine et al. (2006b), where the spiral structure is considered to be a density fluctuation, need to take this into account when studying intrinsic parameters of the spiral arms such as the pitch angle and positions but also when evaluating the kinematic influence on the gas motions. Finally, as seen in Figs. 3.23- 3.23, the presence of spiral arms in the Galactic disk can affect the apparent distribution of HI , not only in the disk but in different heights above the plane. In our models the density wave affects the morphology at least up to a latitude of $b = 4.5^\circ$, while in the real data this maybe up to $b = 8^\circ$.

The main aim of my project was to study the neutral component of the Galactic Halo. The initial observation utilizing the Effelsberg 100-m Radio telescope (Chap.4) showed that the filamentary structure of the HI halo gas detected in the inner Galaxy with the G.B.T (Lockman, 2002) extends even further, beyond the inner part of the Galaxy up to a Galactocentric radius of $R \sim$15kpc. The detected HI clumps have parameters similar to the G.B.T sample, although we found that they are predominantly composed of colder HI gas with a mean $\Delta\upsilon_{1/2}\sim$ 5 $\mathrm{km\,s^{-1}}$ in comparison with 12 $\mathrm{km\,s^{-1}}$ as found by Lockman (2002). Further observations of two clumps from the Effelsberg sample using the WSRT and the VLA telescopes provide an insight in the nature of the clumps. When observed with high resolution, the two Effelsberg clumps with an angular size of more than $20'$, are resolved into a number of cold cores with angular sizes of $\sim 1'$, implying a spatial size of a few parsecs (Chap.5). These cores carry a significant percentage of the neutral gas mass of the region despite their small filling factor. The comparison between the single dish and the interferometry data points towards a specific structure for the neutral halo gas. The colder gas lies in small cores which are embedded in large filamentary structure of warmer gas which stabilizes the cores and also protects them from evaporation. Observations with the 21-cm multi-beam receiver of the 300-m Arecibo telescope confirmed this concept with the detection of HI objects from $\sim 12'$ down to $\sim 4'$, implying spatial scale similar to the interferometry observations. These are cold with a mean $\Delta\upsilon_{1/2}$ of 4.3 $\mathrm{km\,s^{-1}}$ and are surrounded by a very extended (a few degrees) warmer medium. Some of them are estimated to have a Galactocentric distance as far as R=17 kpc.

Being able to put constrains on the physical parameters of the HI halo clumps from our observations and taking into account the detection of two-component structures, I tried to determine the possibility of thermal equilibrium between the clumps and their surrounding envelopes (Chap. 7). Wolfire et al. (2003), gives the range of the pressure versus the total density of the hydrogen nuclei where thermal equilibrium is possible between CNM and WNM. I compared the observationally derived parameters with theoretical phase diagrams. I found that the broad components lie in a region of the phase diagram where the WNM is thermally stable. For the clumps, the sample detected with the Effelsberg telescope proved to be far off the position of equilibrium for CNM but this is due to small scale structure undetected with the Effelsberg telescope. For the cores detected with the WSRT and the VLA and for the Arecibo clumps, I found that their volume densities are equal or slightly smaller than the lower limit allowed for thermal stable CNM. This implies that some of the cores are undergoing a phase transition condensing towards the cold phase or expanding towards the warm phase, while other cores are in the region of stable CNM and lie in thermal equilibrium, with the surrounding envelope. The above assumption does not take into account the presence of molecular hydrogen H_2 in the Galactic Gaseous Halo. Large scale CO(2-1) surveys confirm this assumption since the do not detect significant amount of molecular gas at $b > 10^\circ$. All this is under the assumption that molecular hydrogen does not exist in significant quantities in the Galactic gaseous Halo. Thus the total density of the hydrogen nuclei is defined by the HI volume density. However the discrepancy in the position of the cold cores may be evidence for the presence of H_2. In this case I have underestimated the true density of the hydrogen nuclei in the cores. As a result in reality the cores should be positioned further right in the phase diagrams, well within the region of the cold gas. In this case H_2 could also contribute to the volume density and pressure thus stabilizing the clumps. One possible explanation of the discrepancy between the molecular gas surveys and this result is that H_2 resides in very small concentrations, which are difficult to detect using the current telescope resolution. Dessauges-Zavadsky et al. (2007) describes a similar scenario to explain the non detection of H_2 in HVC's. Finally, another important factor to take into account is the assumption of conditions (like metalicity, dust-to-gas ratio etc) of the halo similar to the disk. Different conditions change the morphology of the phase diagrams. Using values closer to the actual values of the Halo may yield the result that the cores lie in the region of stable cold neutral gas.

Using the detected sample of HI halo clumps I have also tried to test different formation scenarios for the clumps. A study of their origin is directly linked with questions regarding the formation mechanism and maintenance of the whole Galactic halo. Lockman (2002) proposed that the clumps are the late stage products of a motion which is a result of a Galactic fountain produced by supernova explosions. To study such an association between the HI clumps and the Galactic fountain mechanism, I used a simple ballistic simulation disregarding effects such as phase-transition and drag. I made a comparison between the kinematical parameters, like υ_{lsr} predicted from the simulation with observed parameters for the detected HI clump samples. For initial vertical velocities smaller than the speed of sound, the simulation matched the υ_{lsr} and Galactocentric positions for only half of my sample. The starting height of the ballistic motion is less than 1kpc, implying that the radiative cooling mechanism must be extremely efficient to form HI clumps fast enough from the hot bubble, agreeing with the original prediction from Shapiro & Field (1976). Therefore the Galactic fountain formation mechanism cannot be excluded from kinematical point of view for the clumps residing at $R > 8.5$ kpc. Accurate simulations are needed to compare the temperature, density and pressure distribution produced by the simulation with the observational results. The second possible scenario to explain the formations of the HI clumps, proposes that they are the result of turbulence which is maintained and created by the bulk motion of the Milky Way (Fleck, 1981). This mechanism is supported by the study of the density fluctuations in the large field observed with the 300-m Arecibo telescope. As shown in Chap. 8 its 2-D spatial power spectrum exhibits a power law behavior for all the studied velocities υ_{lsr} and various velocity binnings. The index is close to the predicted Kolmogorov index of 2.66. The spatial inertial range where there exists dissipation-less energy transfer ranges from a few degrees down to 11 arc minutes which is the size of most of the largest clumps detected in the Arecibo map. Thus it seems that turbulence plays an important role in the ISM in the Galactic Halo. Furthermore Audit & Hennebelle (2005) show an example how the fragmentation of the turbulent neutral hydrogen is possible while maintaining thermal equilibrium. Their two dimensional simulation of converging turbulent flows of warm neutral gas results in dynamical condensations which produces cold neutral gas objects. Although the simulation discusses scales smaller than the ones under study and the produced cold neutral gas structures have linear dimension of the order of 0.1pc, it is striking that the morphology exhibited in their synthetic density maps (Fig.4; Fig. 5 of Audit & Hennebelle (2005)) is very similar to the morphology observed in our observation of large regions e.g the Arecibo field. In the end it is quite possible that both turbulence and Galactic fountains, are responsible for the creation and maintenence of the filamentary neutral phase, with the first one playing a role in the outer part and the second one being more dominant in the inner Galaxy.

Using my sample I compare also the halo clumps with the model predicting the morphology for the cold neutral medium. Heiles & Troland (2003b) showed that the cold neutral gas should be expected to form thin sheet like filamentary structure with a length-to-width ratio of 70 or even more. In Chap. 8 I showed that while a moderate ratio of 10 between length-to-thickness ratio should be expected from thermal equilibrium consideration, a higher ratio is not evident in the data and would produce un-physically high pressures.

Another important result is the detection of an extraordinary HI object with the Arecibo 300-m telescope. I found a small spherical object which while having parameter similar to the HI clumps, seems to show evidence for solid body rotation and self-gravitation. The object has an angular size of $6'$ which, if the distance estimate is corrected, means that it has a size of 10pc. Further investigations with high resolution are necessary to clarify the nature of this object. If these confirm the Arecibo observation, then this object will be the first one to be in stark contrast with assumed sheet-like morphology of the CNM and the HI clumps.

As a final word, the existence of the clumpy HI gaseous halo is well established. In order to learn more, a large sample of the clumps is needed now to study the properties in a sample with increased statistical significance and test the equilibrium conditions is the Galactic Halo. Observations of other wavelengths are also required to determine the content in molecular gas, the metalicity and the dust-to-gas ratio. All this will help us understand better the properties of the ISM in the Halo, its origin and interactions with the other components.

11 Appendix I

Here follows the spectra of the detected Effelsberg clumps given in Chap 4 and the table 11.25 with the observed regions.

	l °	b °	δl °	$delta$b °
Field 1	134	-43	3	3
Field 2	122.5	-43	3	3
Field 3	116.4	22.5	3	3
Field 4	141.5	25	3	3
Field 5	146.5	43	3	3
Field 6	147	41.5	2	2
Field 7	57	50.5	3	3
Field 8	46	16.5	3	3
Field 9	117	29	3	3
Field 10	116.5	25.5	3	3
Field 11	133.5	34.5	3	3
Field 12	113.5	25.5	3	3
Field 13	145.5	-42.5	3	3
Field 14	135.35	36	3	3
Field 15	113.5	25.5	3	3
Field 16	113.5	29	3	3
Field 17	120	25	4	4
Field 18	116.5	29.5	3	3
Field 19	130	-19	4	4
Field 20	132	-21.5	2	2
Field 21	144	-13.5	2	2
Field 22	113.5	-14	4	4

Tab. 11.25: *A table of all the region selected and observed at 21-cm with Effelsberg Radio Telescope. The first two column give the galactic coordinates of the center of the region while the last two define the dimensions of the scanned region*

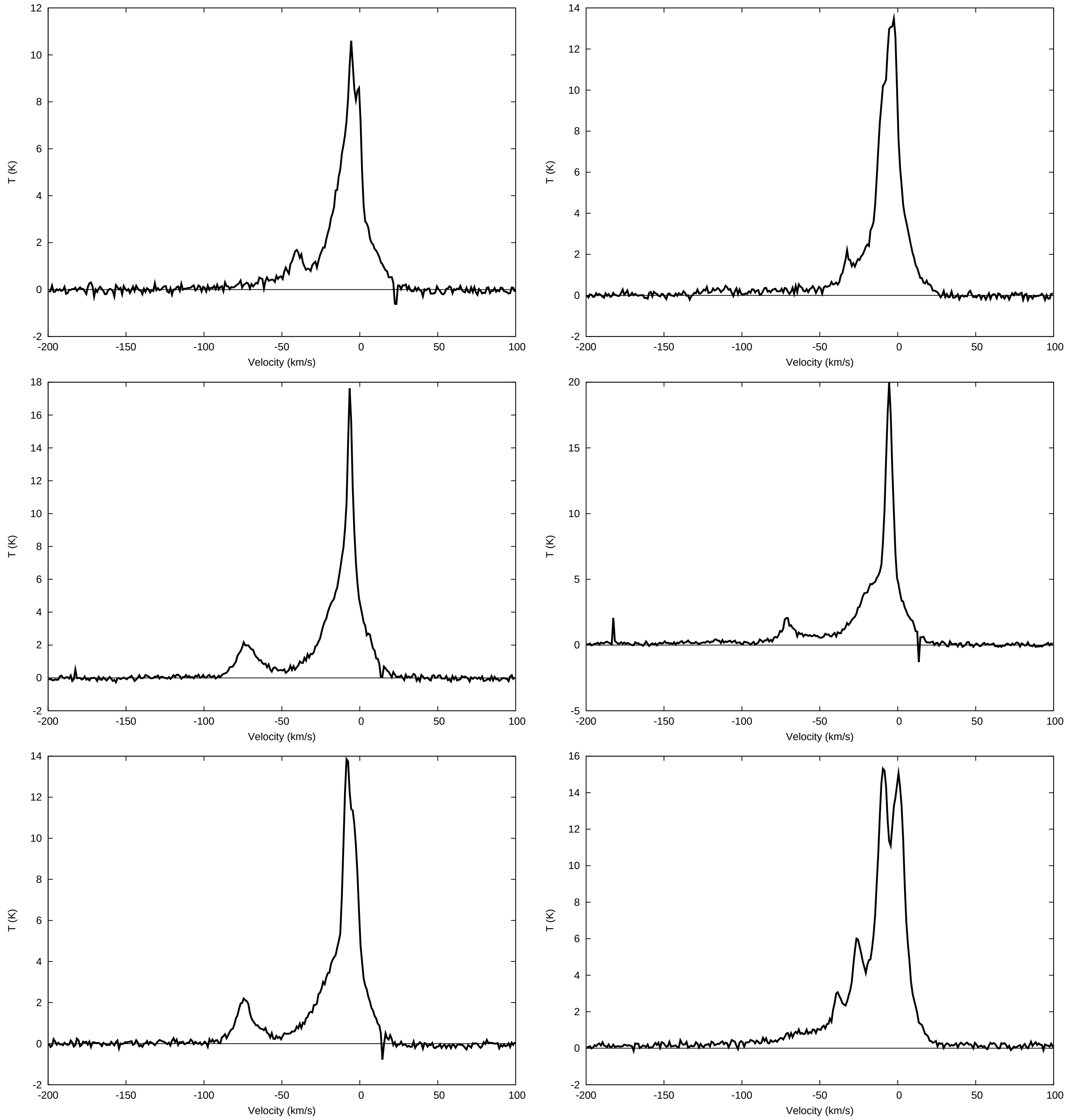

Fig. 11.59: *The spectra of the two clumps detected with the Effelsberg 100-m telescope . a) Top left: Clump 113.33+27.00 b) Top right: 113.13+25.49. c)Middle Left: Spectrum of 118.01+24.59 d) Middle Right: Spectrum of 117.97+24.00 e) Bottom Left: 117.51+25.19 f)Bottom Right:114.5-15.85*

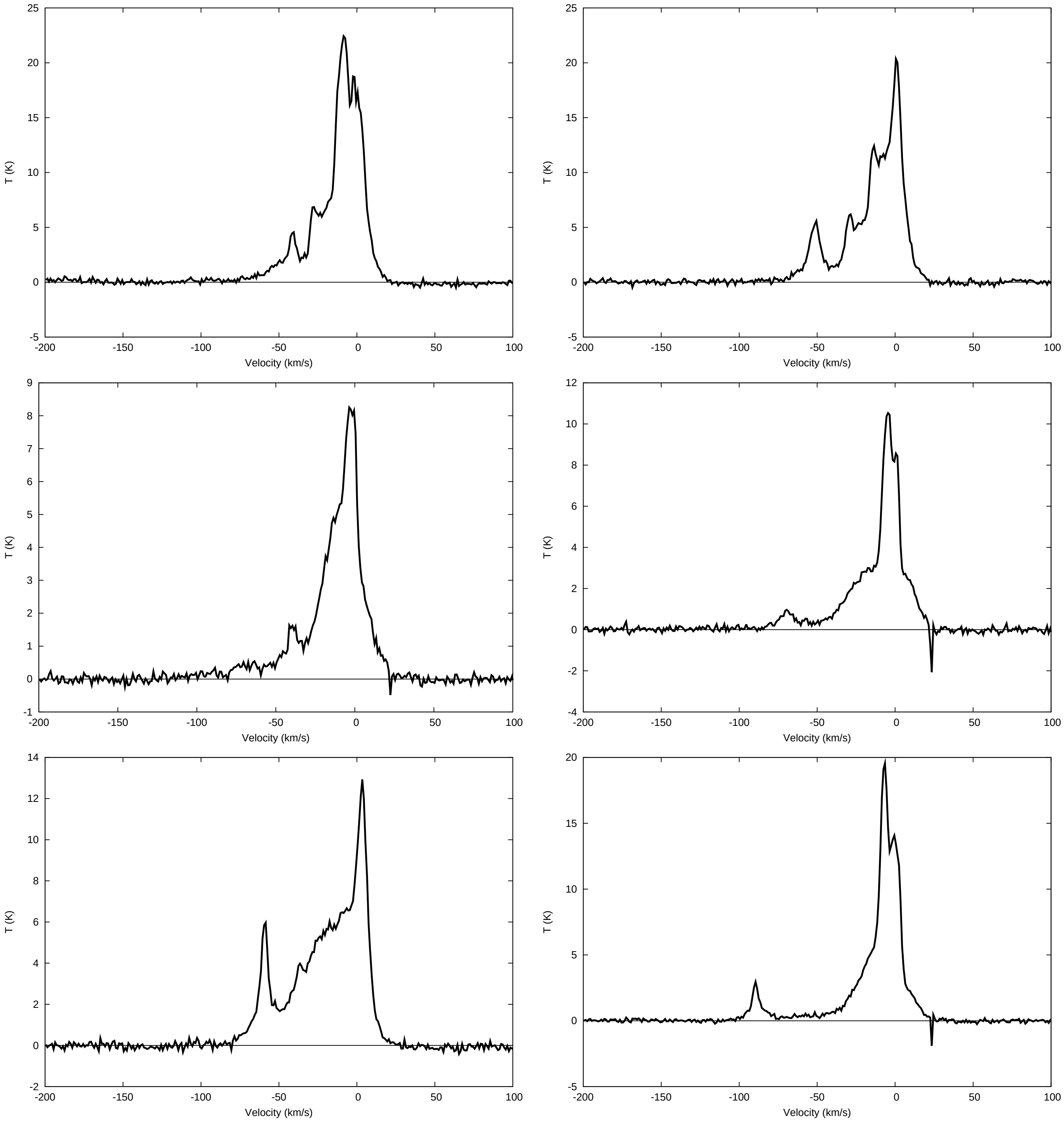

Fig. 11.60: *Spectra of the* HI *clump detected with the Effelsberg 100-m telescope. a)Top left: 112.96-13.03 b) Top right: 113.57-13.48 c)Middle left : 112.1+27.79 d) Middle Right: 113.84+28.7 e) Bottom left: 128.84-18.48 f) Bottom Right: 114.71+29.6*

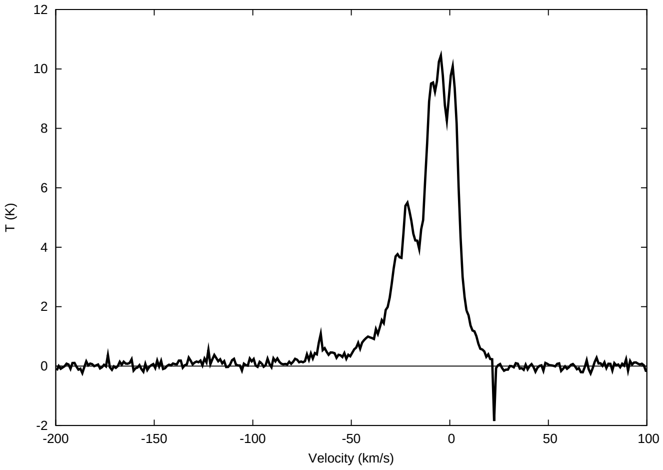

Fig. 11.61: *Spectrum of 112.45+29.9 of* HI *clump detected with the Effelsberg telescope*

12 Appendix II:Brightness temperature ratio K of a mix of warm/cold neutral gas.

We assume a telescope having a Gaussian beam with FWHM of C measures brightness temperature T_C while a telescope having a Gaussian beam with FWHM of A(A<C) measures a brightness temperature T_A. We define $K = \frac{T_A}{T_C}$. Assuming both of the telescopes observe an isolated point-source in the sky, according to Rohlfs & Wilson (2004), $K \sim \frac{C^2}{A^2}$. In the case of the LAB survey the beam has an angular size of $36'$while the Effelsberg telescope has a size of $9'$and the ratio K for an isolated point source is then 16. This formulation is valid only for an isolated compact source, therefore it is not applicable in the case of HI clumps where the morphology is different. In such a case small HI cores are surrounded by extended warm medium.

I will try to determine a relation for the ratio K which is better applicable to the HI clumps. The flux density received by a telescope from a source in the sky is $S \propto T \cdot \theta^2$ where S is the flux density, T is the brightness temperature of the source and θ is the source size. I assume we have the telescopes described earlier with beam size C and A where A<C, the region observed in the sky has extended emission of brightness temperature T_1. This extended emission surrounds an number n of cores with angular size D and brightness temperature T_2. The cores are tightly packed in a region smaller than A. Fig.12.62 describes the morphology of the observed region. Essentially this figure is similar to the expected morphology of the HI halo clumps.

The telescope with beam size C, measures a flux $S_C = S_1 + S_2$, the result of emission S_1 received from the extended source and the total emission S_2 from the cores. Therefore we find that the measured brightness temperature T_C is given by :

$$T_C = (1 - n \cdot (\frac{D}{C})^2) \cdot T_1 + n \cdot (\frac{D}{C})^2 \cdot T_2$$

Accordingly the telescope with beam size A, measures a brightness temperature T_A which is given by :

$$T_A = (1 - n \cdot (\frac{D}{A})^2) \cdot T_1 + n \cdot (\frac{D}{A})^2 \cdot T_2$$

So the ratio K of T_A over T_C in the case an extended source surrounding compact cores is:

$$\frac{T_A}{T_C} = \frac{(1 - n \cdot (\frac{D}{A})^2) \cdot T_1 + n \cdot (\frac{D}{A})^2 \cdot T_2}{(1 - n \cdot (\frac{D}{C})^2) \cdot T_1 + n \cdot (\frac{D}{C})^2 \cdot T_2}$$

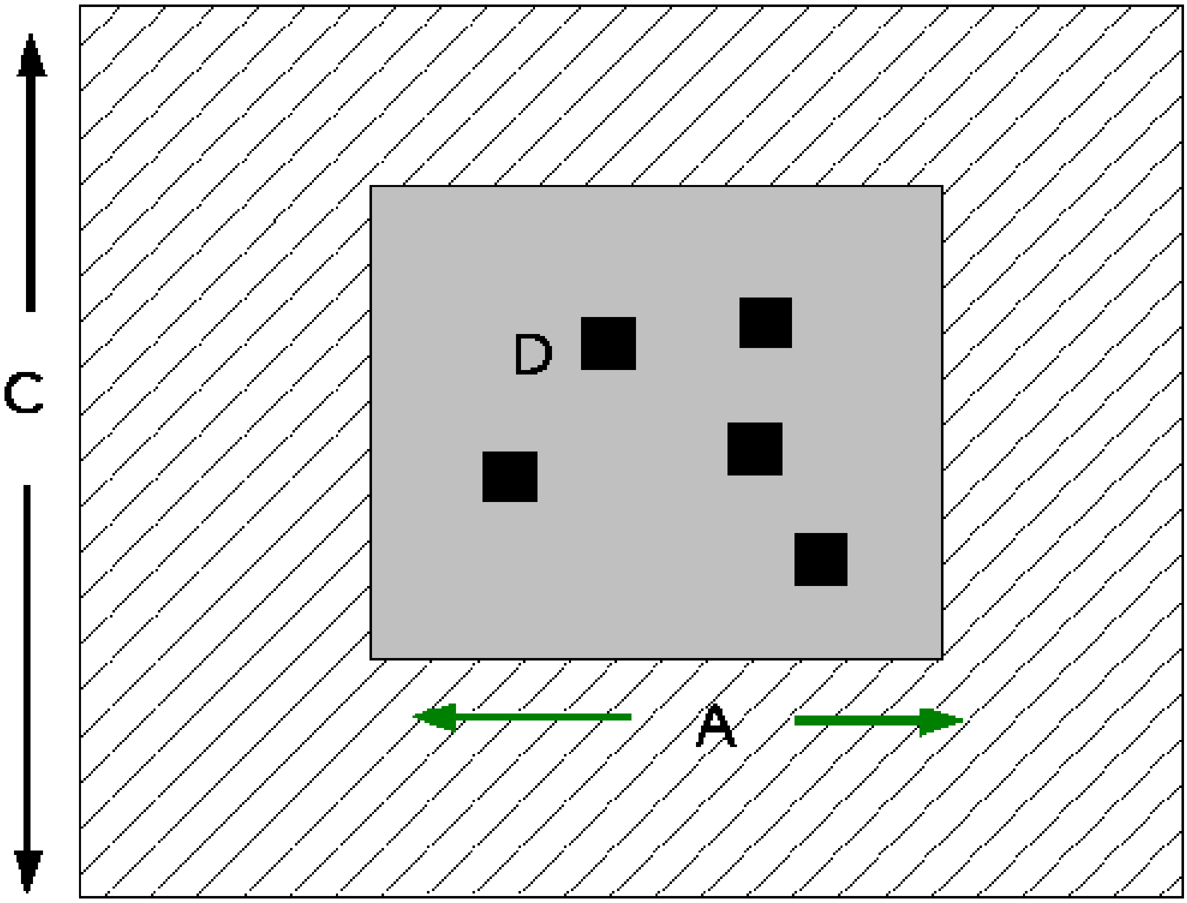

Fig. 12.62: *A drawing which represents the area covered by the beam of the LAB survey, in comparison with the area of the Effelsbergbeam and the area covered by the constituents of an* HI *clump. The beam size of the LAB survey is C, the beam size of the Effelsberg has A' while the constituents have a size of D. The number of constituents is n. They are close together and have a source temperature of T_2.They are surrounded by extended emission which fill both of the beams and has a temperature of T_1.*

Assuming a temperature for the extended envelope of 1 K, I used this values to create three figures which show the size of the different cores in relation to three different parameters. In Fig.12.63 I used for the ratio K the mean value of 3.32 found in Chap. 4 and plotted the core diameter D vs the brightness temperature of the core T_2 for different n number of clumps. In Fig.12.64 I took the number of clumps n=10 and plotted the source diameter D vs the brightness temperature T_2 for different ratio K. Finally in Fig. 12.65, I kept constant the number of clumps n and plotted the core diameter D vs the ratio K for various brightness temperature T_2 of the cores. These

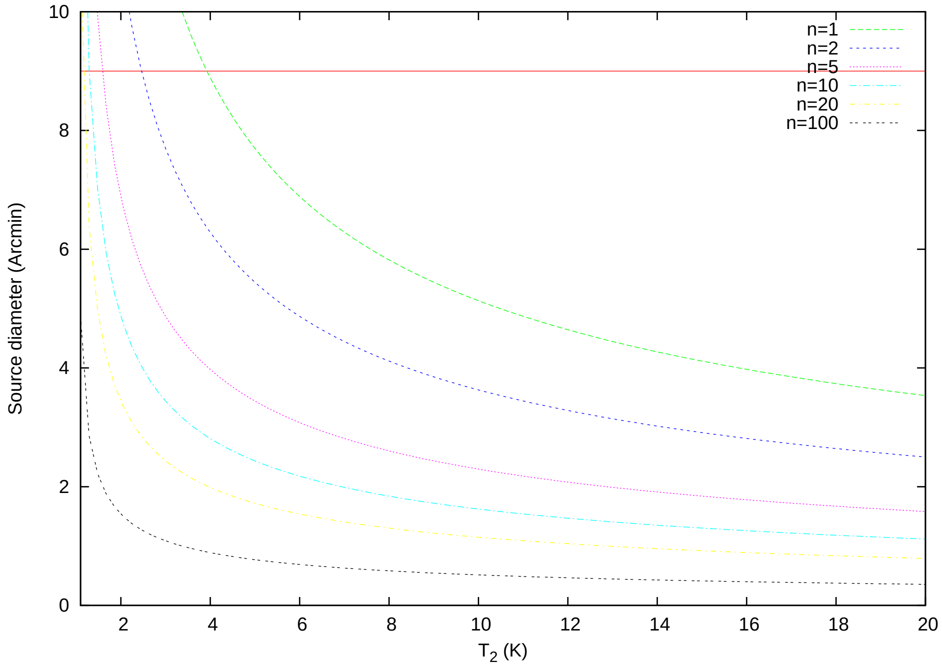

Fig. 12.63: *A diagram of the core diameter D as a function of the brightness temperature of the source* T_2 *in K for different number of clumps n. I assume the ratio* K *is* $K = 3.32$ *which is the mean value found in Chap.4. I assume the brightness temperature of the extended source is* T_1*=1K.*

three diagrams show that a low ratio K between the Effelsberg and the LAB spectrum can imply unresolved sub-structure. As long as the filling factor of the cores is low and they are surrounded by extended emission even the presence of moderate sub-structure will result in a low ratio K. As the temperature T_2 and the number of cores becomes larger, their size D must become smaller. Even in the most extreme case the size of the core is not significantly less than an $1'$.

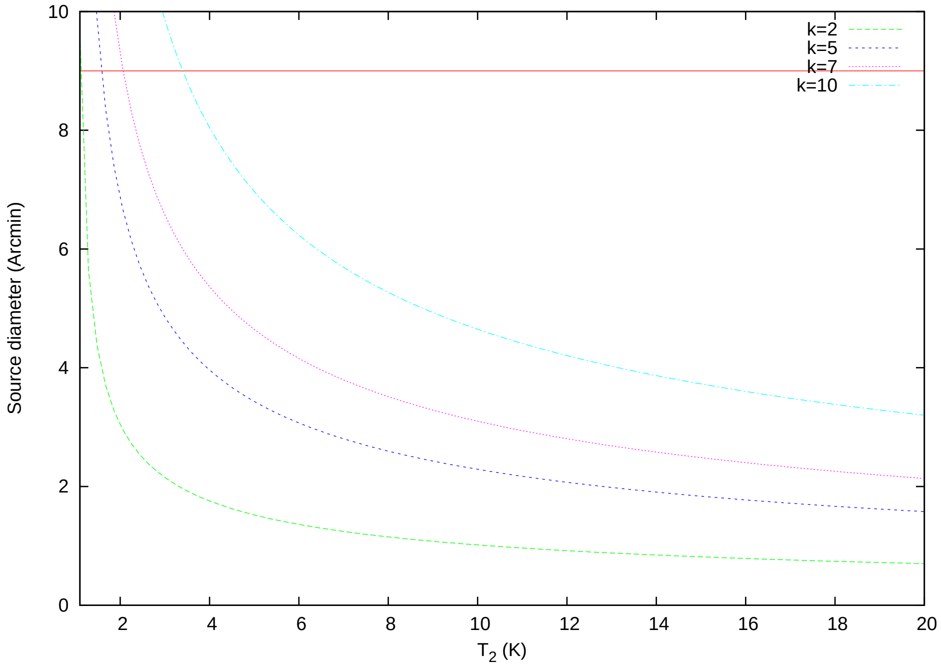

Fig. 12.64: *A diagram of the source diameter D as a function of brightness temperature of the source* T_2 *for different ratio K. The number of cores n constituting the clump is fixed at n=10. I assume the brightness temperature of the extended source is* T_1*=1K.*

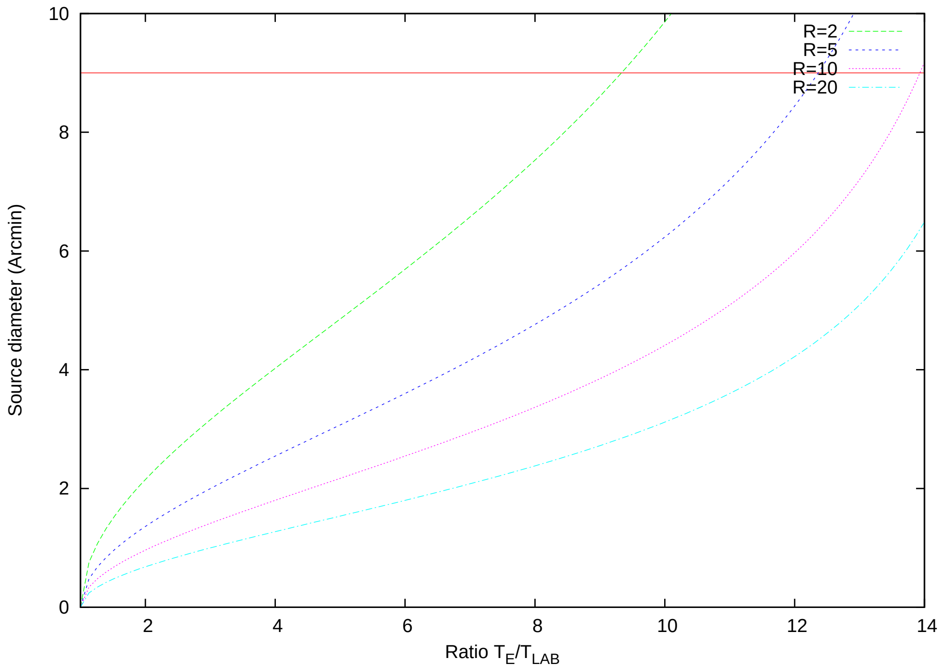

Fig. 12.65: *A diagram of the source diameter D as a function of the ratio K for different core brightness temperature* T_2*. The number of cores n constituting the clump is fixed at n=10. I assume the brightness temperature of the extended source is* T_1*=1K.*

13 Acknowledgments

I arrived in Bonn to begin my studies in 2001. My goal was to study astronomy and finally obtain a doctorate in this field. It was not always an easy task and it had its up and downs but it always remained a fulfilling experience that enriched me as a person. Now that I am about to complete my thesis, I would like to thank a number of people who in one way or another helped me.

I would like to thank Peter Kalberla, not only for being the prime mover behind the project but also for his willingness to share his knowledge about Galactic HI and offering me the opportunities and the scientific inspiration. I am truly indebted to him, above all else, because he was the best supervisor anyone could ask for, always caring for me and my thesis.

I would like to thank Jürgen Kerp, for his useful and critical comments that defined part of my thesis. I want also to thank him for the time he took to read the manuscript of the thesis and for his useful corrections.

I would like to thank Uli Klein, who, despite being extremely busy, was a constant help during my studies at the University of Bonn. I still fondly remember how during the beginning of my studies he gave a lecture just for me, and later, in the early part of my thesis he encouraged me to give my first talk at a meeting in Croatia, up to the last stages of my thesis when he still found the time to check on the progress of my thesis.

I would like to thank Ulrich Mebold for his support on my project but also for the useful scientific discussions we had and the insight in the data he offered me.

I would like to thank Christina Stein-Schmitz, not only for her help but also for her sincere care. The AIfA is lucky to have her.

I would like to thank all my officemates during my time in the AIfA, Christoph Böttner, Gianfranco Gentile, Christian Struve and Maike Sawitzki for the friendly and nice atmosphere.

I have spend the last five years working in the AIfA. Throughout this time I have met a lot of interesting people, who made my stay here a nice experience, but I would like to thank especially Jorge Pineda, Tobias Westmeier, Juan Pradas and Franz Kenn for the beers, the hiking, the discussions and friendship.

This project was supported by Deutsche Forschungsgemeinschaft, grant KA1265/5-1.

I would like to thank Snezana Stanimirovic for the opportunity she gave me to use the Arecibo 300-m telescope and Joshua Peek and Kevin Douglas for their help during the reduction of the Arecibo data.

I would like to thank Ralf-Jürgen Dettmar and the “Graduiertenkolleg 787” for the financial support during the early stages of my thesis.

I would like also to thank all my friends here in Bonn but also back home for all the fun times we had together.

I would like to thank my wife, Carolin, for all her support and help. Especially during the last stages of the thesis she gave me the necessary optimism boost, support and kind words to finish the project.

Finally I would like to thank my parents Apostolos Dedes, Anna Dede and my sister Christina Dede. Without their support and help I think I would have never come this far.

14 Summary

Recently the existence of a neutral component of the Galactic Halo was confirmed in all sky HI surveys but also from direct observations of the small scale structure of this component with the GBT telescope (Lockman, 2002). A similar layer, following the disk rotation, was also detected in a few external galaxies. In order to understand the nature of the gaseous halo, its origin and its role in galaxy evolution, it is important to study the neutral component since it composes 50% of the total mass of the Galactic Halo. In my thesis, in order to reach this goal, I studied the physical properties of the small scale structure of the neutral component in the form of HI clumps. Using various telescopes I studied their properties as probes of the gaseous Galactic halo.

The observed properties of the HI clumps can be used to derive their physical state if the distance from the Sun is known. Using the measured line-of-sight velocity υ_{lsr} , I can determine their distance with the help of the velocity field of the Galaxy. In my thesis I used the Bonn Mass Model of the Milky Way. Deviations from circular motion can affect this method of distance determination. One of the most important perturbations is the spiral structure of the Milky Way. In order to evaluate the effect of the spiral structure but also to find whether out it is possible to implement spiral structure in the mass model, I utilized the linear density wave theory to model the Milky Way spiral arms. The result were formatted as synthetic image cubes which I compared with the real HI data from the all sky LAB survey for similarities with the velocity structure found there. As is evident from the comparison, the linear density theory reproduces at least partially successfully the morphology observed in the LAB image cube. Therefore it can potentially be used as a basis for a more complex model of the Milky Way spiral structure. Also as a result it is proven that large scale velocity fluctuation are responsible for the apparent spiral structure in the real image cube and not density fluctuations. Therefore the interpretation of the spiral structure of the Milky Way need to be handled with extreme care. More importantly, I found that the spiral structure does affect spectra up to latitudes of $|b|$=8°.

The main purpose of my thesis was to study the properties of the co-rotating HI halo clumps. With the help of the LAB survey a number of regions were identified where the emission unambiguously is originating from the halo. I made 21-cm line observations of these regions using the 100-m Effelsberg Radio Telescope. I have detected in 22 fields, each of a size of 3°x 3°, 25 HI clumps which follow Galactic rotation. They have a mean angular size of $18'$and a column density of the order of $10\cdot10^{18}$ cm^{-2}. All the clumps lie outside the solar circle with a maximum Galactocentric radius $R \leq$15kpc and a height above the disk of $z \leq$5kpc. I detected very narrow line widths with a mean of $\Delta\upsilon_{1/2}$=5.3 km s^{-1}; in agreement with Wolfire et al. (2003) who expects cold gas up to 18kpc distance from the center. The physical properties of the sample are similar to the HI clumps detected with the GBT radio telescope (Lockman, 2002) in the inner Galaxy, although the sample shows more narrow line width implying a bias towards observing colder gas. The most important property of the clumps is that in their majority, they are found to be embedded in a warmer medium with a more extended distribution, thus showing two component structure. The broader component appears in the spectra to be connected with the main Galactic line. Estimates of the visible HI mass show that the clumps are not virialized. In this case the surrounding extended component should play the role of a confining stabilizing envelope to the clumps. The Effelsberg observations do not support this case. A comparisons between the observed pressures of the HI clumps with estimates for the surrounding the warm components show that the clumps are under-pressured, thus not in pressure equilibrium with the envelope. This discrepancy could be explained assuming that the clumps show extensive small structure which is unresolved with the Effelsberg beam.

In order to study the small scale structure of the clumps, the two most prominent ones were observed with high resolution using the Westerbork interferometer and the Very Large Array. The results show that the HI clumps are resolved into a number of cold cores ($\Delta\upsilon_{1/2}\sim$ 4km s^{-1}) with an angular size of a couple of arc-minutes, implying a true size of a few pc. These cores in comparison with the “parent” Effelsberg clumps have up to 30 times higher density and pressure. Also they seem to carry a significant percentage of the total visible HI mass in the region. A comparison of their pressure with the surrounding medium detected with Effelsberg shows that the two components can be in pressure equilibrium. Therefore it is confirmed that indeed the extended component plays the role of the confining envelope and the discrepancy in the Effelsberg observations is due to limited resolution. In comparison with VLA studies of similar HI objects (Stil et al., 2006), our sample of HI cores show smaller densities and pressures. This difference can be explained by the larger distance in Galactocentric radius R.

To enlarge our sample, we have observed a region in the fourth Galactic quadrant using the Arecibo 300-m telescope. The beam resolution is $\sim 4'$. We have detected 16 HI objects outside the solar circle. These objects show the same two-component structure as the HI clumps observed with Effelsberg telescope. They have a mean angular diameter of $6'$ and they are also very cold. The whole sample is denser and has higher pressures in comparison with the Effelsberg sample. It is possible that there is also in this case a pressure equilibrium with the surrounding warmer gas. The properties of these clumps show a great similarity with the properties of the cores observed with the synthesis arrays. As a side product of the Arecibo observation I have detected a spherical object with angular diameter of $6'$which seems to exhibit solid-body rotation. If the Arecibo observation are verified I will have detected the first cloud which does not conform with the contemporary perception of the neutral medium clouds as being sheet like.

Having assembled the different telescope sample of the HI clumps, I compared them with other studies of clumps in the inner Galaxy using the GBT (Lockman, 2002), in the anti-center using the Arecibo telescope (Stanimirović et al., 2006), and at low latitude using the VLA (Stil et al., 2006). We found that the observational quantities, which are directly comparable, are similar. There I concluded that the different samples can be considered to be characteristic for the same population of clumps despite different location. Most importantly, I compared my sample of clumps with theoretical phase diagrams (Wolfire et al., 2003) in order to test the possibility of a thermal equilibrium between the clumps and the warmer extended envelopes. The Effelsberg sample did not match the theoretical predictions of a thermal equilibrium. As already discussed, this can most probably be attributed to a systematic bias caused by insufficient beam resolution. For the Arecibo, VLA and the WSRT sample I found that all the HI objects lay either in the region where cold neutral medium is allowed to exists in stability or in the region where phase transition is taking place. Therefore they can exist in thermal equilibrium with the surrounding medium. These envelopes seem not only to provide confinement for the clumps but protect them against fast evaporation by the hot plasma. It is difficult to determine the exact conditions in the clumps since their molecular content is unknown. A significant amount of molecular gas can be hidden in extremely dense concentrations with a very low filling factor.

Utilizing the larger area observed with Arecibo, I was able to study the turbulence in HI at different distances. This was done by calculating the spatial power spectrum from the image cube for each line-of-sight velocity υ_{lsr} . I found that throughout the different velocity ranges, the power spectrum exhibits a power law behavior with an index $\gamma = -2.65$, very close to the expected index for a 2-D spatial power spectrum described by a Kolmogorov spectrum. This power law seems to be true from $14'$ scale up to 5°scale. This implies that turbulence is a important factor for the transfer of energy from the largest scales to the smallest scale in the Galactic halo.

Finally we test the hypothesis of the Galactic fountain as a mechanism to create the clumps. Using a basic ballistic simulation I compared the observed kinematical properties of the clumps with the predictions for clumps following a ballistic motion, the end stage of the Galactic fountain mechanism. I found that for 50% of the clumps the observed values agreed with the simulation while for the rest no ballistic motion could reproduce the observed kinematical parameters. As a result I deduce that the Galactic fountain mechanism, at least partially, can account for the creation of the clumps. In addition I studied the morphology of the clumps in comparison with the predicted sheet like morphology of the CNM. Neither a sheet-like morphology nor a more spherical morphology could be supported by directed evidence. Indirect arguments, based on thermal and pressure equilibrium and the presence of turbulence, show that the clumps should not have the sheet like morphology with extreme length-to-width ratio of 70 as proposed by Heiles & Troland (2003b) for the CNM.

References

1998, JRASC, 92, 271

Albert, C. E., Welsh, B. Y., & Danly, L. 1994, ApJ, 437, 204

Audit, E. & Hennebelle, P. 2005, A&A, 433, 1

Bracewell, R. N. 1956, Australian Journal of Physics, 9, 297

Brand, J. & Blitz, L. 1993, A&A, 275, 67

Bregman, J. N. 1980, ApJ, 236, 577

Burton, W. B. 1971, A&A, 10, 76

Carilli, C. & Rawlings, S. 2004, ArXiv Astrophysics e-prints

Chandrasekhar, S. 1949, ApJ, 110, 329

Crane, P. C. 1988, S&T, 76, 634

Crovisier, J. & Dickey, J. M. 1983, A&A, 122, 282

de Boer, W., Sander, C., Zhukov, V., Gladyshev, A. V., & Kazakov, D. I. 2005, A&A, 444, 51

Dessauges-Zavadsky, M., Combes, F., & Pfenniger, D. 2007, A&A, 473, 863

Dickey, J. M., McClure-Griffiths, N. M., Stanimirović, S., Gaensler, B. M., & Green, A. J. 2001, ApJ, 561, 264

Fernández, D., Figueras, F., & Torra, J. 2001, A&A, 372, 833

Fleck, Jr., R. C. 1981, ApJ, 246, L151

Fraternali, F., Oosterloo, T., & Sancisi, R. 2004, Ap&SS, 289, 377

Gómez, G. C. 2006, AJ, 132, 2376

Gooch, R. 1996, in Astronomical Society of the Pacific Conference Series, Vol. 101, Astronomical Data Analysis Software and Systems V, ed. G. H. Jacoby & J. Barnes, 80–+

Hartmann, D. & Burton, W. B. 1997, Atlas of Galactic Neutral Hydrogen (Atlas of Galactic Neutral Hydrogen, by Dap Hartmann and W. Butler Burton, pp. 243. ISBN 0521471117. Cambridge, UK: Cambridge University Press, February 1997.)

Heiles, C. 1997, ApJ, 481, 193

Heiles, C. 2007, PASP, 119, 643

Heiles, C., Perillat, P., Nolan, M., et al. 2001, PASP, 113, 1247

Heiles, C. & Troland, T. H. 2003a, ApJ, 586, 1067

Heiles, C. & Troland, T. H. 2003b, ApJ, 586, 1067

Józsa, G. I. G., Kenn, F., Klein, U., & Oosterloo, T. A. 2007, A&A, 468, 731

Kahn, F. D. 1981, in Astrophysics and Space Science Library, Vol. 91, Investigating the Universe, ed. F. D. Kahn, 1–28

Kalberla, P. M. W. 2003, ApJ, 588, 805

Kalberla, P. M. W., Burton, W. B., Hartmann, D., et al. 2005a, A&A, 440, 775

Kalberla, P. M. W., Burton, W. B., Hartmann, D., et al. 2005b, A&A, 440, 775

Kalberla, P. M. W., Dedes, L., Arnal, E. M., et al. 2005c, in Astronomical Society of the Pacific Conference Series, Vol. 331, Extra-Planar Gas, ed. R. Braun, 81–+

Kalberla, P. M. W., Dedes, L., Kerp, J., & Haud, U. 2007, ArXiv e-prints, 704

Kalberla, P. M. W. & Kerp, J. 1998, A&A, 339, 745

Kalberla, P. M. W., Mebold, U., & Reich, W. 1980, A&A, 82, 275

Kalberla, P. M. W. & Stenholm, L. G. 1983, Mitteilungen der Astronomischen Gesellschaft Hamburg, 60, 397

Kalberla, P. M. W., Westphalen, G., Mebold, U., Hartmann, D., & Burton, W. B. 1998, A&A, 332, L61

Kiguchi, M., Narita, S., Miyama, S. M., & Hayashi, C. 1987, ApJ, 317, 830

Kolmogorov, A. 1941, Akademiia Nauk SSSR Doklady, 30, 301

Lazarian, A. & Pogosyan, D. 2000, ApJ, 537, 720

Levine, E. S., Blitz, L., & Heiles, C. 2006a, ApJ, 643, 881

Levine, E. S., Blitz, L., Heiles, C., & Weinberg, M. 2006b, ArXiv Astrophysics e-prints

Lin, C. C. & Shu, F. H. 1964, ApJ, 140, 646

Lin, C. C. & Shu, F. H. 1966, Proceedings of the National Academy of Science, 55, 229

Lin, C. C., Yuan, C., & Shu, F. H. 1969, ApJ, 155, 721

Lockman, F. J. 1984, ApJ, 283, 90

Lockman, F. J. 2002, ApJ, 580, L47

Lockman, F. J. & Gehman, C. S. 1991, ApJ, 382, 182

Mac Low, M.-M. & Klessen, R. S. 2004, Reviews of Modern Physics, 76, 125

McClure-Griffiths, N. M., Dickey, J. M., Gaensler, B. M., & Green, A. J. 2004, ApJ, 607, L127

McClure-Griffiths, N. M., Ford, A., Pisano, D. J., et al. 2006, ApJ, 638, 196

McKee, C. F. & Cowie, L. L. 1977, ApJ, 215, 213

Münch, G. & Zirin, H. 1961, ApJ, 133, 11

Nakanishi, H. & Sofue, Y. 2004, in Astronomical Society of the Pacific Conference Series, Vol. 317, Milky Way Surveys: The Structure and Evolution of our Galaxy, ed. D. Clemens, R. Shah, & T. Brainerd, 32–+

Oort, J. H., Kerr, F. J., & Westerhout, G. 1958, MNRAS, 118, 379

Pietz, J., Kerp, J., Kalberla, P. M. W., et al. 1998, A&A, 332, 55

Pogosyan, D. & Lazarian, A. 2005, in American Institute of Physics Conference Series, Vol. 784, Magnetic Fields in the Universe: From Laboratory and Stars to Primordial Structures., ed. E. M. de Gouveia dal Pino, G. Lugones, & A. Lazarian, 287–298

Reed, B. C. 2000, AJ, 120, 314

Richter, P., Sembach, K. R., & Howk, J. C. 2003, A&A, 405, 1013

Rohlfs, K. & Wilson, T. L. 2004, Tools of radio astronomy (Tools of radio astronomy, 4th rev. and enl. ed., by K. Rohlfs and T.L. Wilson. Berlin: Springer, 2004)

Sandage, A. 1961, The Hubble atlas of galaxies (Washington: Carnegie Institution, 1961)

Sault, R. J., Teuben, P. J., & Wright, M. C. H. 1995, in Astronomical Society of the Pacific Conference Series, Vol. 77, Astronomical Data Analysis Software and Systems IV, ed. R. A. Shaw, H. E. Payne, & J. J. E. Hayes, 433–+

Savage, B. D. & Sembach, K. R. 1996, in Astronomical Society of the Pacific Conference Series, Vol. 99, Cosmic Abundances, ed. S. S. Holt & G. Sonneborn, 315–+

Scalo, J. M. 1987, in Astrophysics and Space Science Library, Vol. 134, Interstellar Processes, ed. D. J. Hollenbach & H. A. Thronson, Jr., 349–392

Shapiro, P. R. & Field, G. B. 1976, ApJ, 205, 762

Spitzer, L. J. 1956, ApJ, 124, 20

Stanimirović, S., Putman, M., Heiles, C., et al. 2006, ApJ, 653, 1210

Stark, A. A., Gammie, C. F., Wilson, R. W., et al. 1992, ApJS, 79, 77

Stil, J. M., Lockman, F. J., Taylor, A. R., et al. 2006, ApJ, 637, 366

Vallée, J. P. 2002, ApJ, 566, 261

van Woerden, H., Wakker, B. P., Schwarz, U. J., Peletier, R. F., & Kalberla, P. M. W. 1998, in Lecture Notes in Physics, Berlin Springer Verlag, Vol. 506, IAU Colloq. 166: The Local Bubble and Beyond, ed. D. Breitschwerdt, M. J. Freyberg, & J. Truemper, 467–470

Wakker, B. P., Howk, J. C., Savage, B. D., et al. 1999, in Astronomical Society of the Pacific Conference Series, Vol. 166, Stromlo Workshop on High-Velocity Clouds, ed. B. K. Gibson & M. E. Putman, 26–+

Wakker, B. P., Kalberla, P. M. W., van Woerden, H., de Boer, K. S., & Putman, M. E. 2001, ApJS, 136, 537

Wakker, B. P. & van Woerden, H. 1991, A&A, 250, 509

Wakker, B. P. & van Woerden, H. 1997, ARA&A, 35, 217

Wolfire, M. G., Hollenbach, D., McKee, C. F., Tielens, A. G. G. M., & Bakes, E. L. O. 1995a, ApJ, 443, 152

Wolfire, M. G., McKee, C. F., Hollenbach, D., & Tielens, A. G. G. M. 1995b, ApJ, 453, 673

Wolfire, M. G., McKee, C. F., Hollenbach, D., & Tielens, A. G. G. M. 1995c, ApJ, 453, 673

Wolfire, M. G., McKee, C. F., Hollenbach, D., & Tielens, A. G. G. M. 2003, ApJ, 587, 278

Yuan, C. 1969, ApJ, 158, 871

List of Figures

List of Tables

Ich versichere, daß ich diese Arbeit selbständig verfaßt und keine anderen als die angegebenen Quellen und Hilfsmittel benutzt, sowie Zitate kenntlich gemacht habe.